PULSED LASER ABLATED CARBON PLASMA
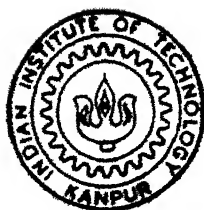
by

Abhilasha Trivedi

DEPARTMENT OF PHYSICS
INDIAN INSTITUTE OF TECHNOLOGY KANPUR
April, 1994

PULSED LASER ABLATED CARBON PLASMA

A Thesis Submitted
In Partial Fulfilment of the Requirements
for the Degree of

DOCTOR OF PHILOSOPHY

by
A bhilasha Trivedi

to the

DEPARTMENT OF PHYSICS
INDIAN INSTITUTE OF TECHNOLOGY
April, 1994

CERTIFICATE
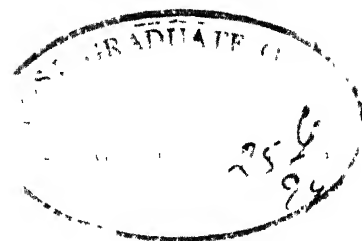
It is certified that the work contained in the thesis entitled "PULSED LASER ABLATED CARBON PLASMA" by Abhilasha Trivedi has been carried out under my supervision and this work has not been submitted elsewhere for a degree.

Kanpur

April 25, 1994

(R. K. Thareja)

Professor

Department of Physics

I.I.T. Kanpur

SYNOPSIS

Name of student : Abhilasha Trivedi   Roll # : 9010961

Degree for which submitted : Ph.D.   Department : **Physics**

Thesis Title : PULSED LASER ABLATED CARBON PLASMA

Name of the thesis supervisor : Professor R K Thareja

The thesis describes studies of Nd:YAG laser ablated carbon plasma in vacuum and in the presence of ambient gases at low and moderate laser irradiances. A detailed investigation of optical emission of laser produced ionic/atomic (C I, C II, C III, C IV and C V) and molecular (C_2) species of carbon in vacuum and in the presence of background gas viz. air, helium and argon was conducted. A peculiar double peak structure observed in the temporal profile of the C II transition $3d\ ^2D - 4f\ ^2F^0$ at 426.7 nm in an ambient gas was attributed to Rayleigh-Taylor instability at the interface. The presence of carbon clusters (fullerenes) in laser ablated carbon soot and carbon films obtained from laser vaporization of graphite in a helium atmosphere is reported. A Nd:YAG laser (1.06 μm) delivering 1 J of energy in 2.5 and 8 ns (FWHM) pulse with a repetition rate of 10 pps (and its harmonics 2ω, 3ω and 4ω) was used to produce carbon plasma.

To study laser ablated carbon plasma the laser radiation was focussed onto a rotating graphite target mounted in a vacuum chamber. The experiments were carried out in vacuum and for different pressures in the range 10^{-3}-100 Torr of air, helium and argon gas. The plasma radiation was imaged onto a monochromator (HRS-2, Jobin Yvon) and the output was detected with a photomultiplier tube (1P28, Hamamatsu) and recorded on a strip chart recorder or displayed on an oscilloscope (11302A, Tektronics). The signals

were digitized and fed to personal computer for further data processing. For depositing carbon films laser radiation was focussed using a cylindrical lens. The carbon films were deposited on silicon and glass substrates under various helium pressures. The ablated carbon powder 'soot' was also collected from the chamber at different helium pressures to ascertain the presence of fullerenes, C_{60}.

The emission spectra of carbon plasma were recorded in the wavelength range 190-800 nm at various distances away and parallel to the target surface (z = 0-20 mm) at different laser irradiances and wavelengths (1.06, 0.532, 0.355 and 0.266 μm). Assuming the plasma to be in local thermodynamic equilibrium the electron temperature of the carbon plasma was estimated from the relative intensities of spectral lines. Electron temperature calculated at 2 mm away and parallel to the target surface for C II, C III and C IV species at 8×10^{11} W/cm^2 laser irradiance was found to be 4 eV, 6 eV and 7 eV respectively. It is observed that the electron temperature increases with higher ionic charge and decreases with increase in distance away from the target surface. Variation of electron temperature with intensity of laser radiation shows $I^{0.4}$ dependence. The electron density was estimated from the stark broadened profile of C II transition $3p\ ^2P^0 - 4s\ ^2S$ at 392.0 nm at various distances away from the target in vacuum and was found to be in the range $10^{16}-10^{17}$/cm^{-3}. Temporal profiles of C II transition $3d\ ^2D - 4f\ ^2F^0$ at 426.7 nm, C III transition $3s\ ^3S - 3p\ ^3P^0$ at 465.0 nm and C IV transition $3s\ ^2S - 3p\ ^2P^0$ at 580.1 nm were recorded to estimate the velocity of the plasma front. The expansion velocities of C II, C III and C IV species were found to be about 4×10^6, 7×10^6 and 10×10^6 cm/sec respectively. The expansion velocity of C II species in the presence of helium, argon and air at 10^{-3} Torr

was found to be 8.2×10^6, 7.3×10^6 and 7.5×10^6 cm/sec respectively. The velocity decreases with the increase in background gas pressure and atomic mass of the ambient gas. Studies of laser ablated carbon in the presence of helium and argon showed enhancement of line emission for the transitions $2p^2\ ^1D - 3s\ ^1P^0$ of C I at 193.1 nm, $3p\ ^2P^0 - 5d\ ^2D$ of C II at 213.7 nm, $3d\ ^3D - 4f\ ^3F^0$ of C III at 192.3 nm and $3d\ ^1D - 4f\ ^1F^0$ of C III 216.3 nm. It was observed that line intensity was more in presence of helium and argon gases than that in vacuum. This is attributed to enhanced cooling of the expanding plasma in the presence of background gas which increases the three body recombination rate ($\alpha_c \propto T_e^{-9/2}$) and results in populating the excited neutral/ionic carbon species.

The spatial and temporal characteristics of various ionic states at various pressures of background gas were performed. An interesting feature observed is the appearance of a hump in the temporal profile of the C II transition $3d\ ^2D - 4f\ ^2F^0$ at 426.7 nm at distances far away from the target viz. 12, 7 and 8 mm for helium, argon and air respectively. It was found that the onset distance for the double peak structure decreases with the increase in pressure and atomic mass of the ambient gas. To explain the peculiar double peak various interaction processes such as recombination, charge transfer, blast/shock wave interactions, micro-instabilities etc. were considered. It is proposed that at the interface region due to density fluctuations Rayleigh-Taylor instability occurs in the decelerating laser plasma front and leads to stratification of the plasma into fast and slow ion components. We found that at 0.1 Torr, mutual penetration of the laser plasma ions and the ambient gas decreases and interaction region becomes an interface. The experimental value of 0.1 Torr compares well with theoretically evaluated pressure of the ambient gases at which Rayleigh-Taylor instability occurs at the interface i.e. 0.16

Torr of air, 0.19 Torr of argon and 0.36 Torr of helium gas.

At moderate laser intensities ($\sim 10^9$-10^{12} W/cm^2) atomic/ionic species from C V to C I which recombine through atomic to molecular carbon are observed. However, at low irradiance ($\sim 10^8$-10^9 W/cm^2) molecular C_2 emission was found to dominate the plasma emission. C_2 emission studies are helpful to optimize parameters for diamond like carbon film deposition, to correlate carbon clusters with the plasma dynamics and to investigate the spectroscopy of small carbon clusters. We observed C_2 emission in the $\Delta v = -2, -1, 0, +1,$ +2 sequences of the Swan ($d^3\Pi_g$-$a^3\Pi_u$) bands and the $\Delta v = 0$ and +1 sequences of the Deslandres-d'Azambuja ($C^1\Pi_g$-$A^1\Pi_g$) bands. The studies were performed at various laser irradiance, wavelength and at various pressure of the ambient gas. It is found that there is an optimum energy at which the intensity of C_2 band heads is maximum. The presence of helium gas enhances the intensity of emitted spectrum and of all Swan band heads. The presence of " high pressure " band of the Swan system at 589.9 nm originating from $v' = 6$ level suggests that the plasma is in fast recombining phase. Vibrational temperature estimated from the measured emission intensities of the Swan band heads of the sequence ($\Delta v = -1$) at various laser energies and wavelengths and under various helium pressures was found to be in the range of 6000 - 12000 K. Temperature and velocity of the C_2 species decrease with the increase in helium pressure. Vibrational temperature increases with the decrease in laser wavelength. It is found that shorter laser wavelength irradiation produced higher vibrational temperature at all helium pressures. Vibrational temperature calculated at various energies for 0.355 μm at 10^{-1} Torr helium pressure showed that there exists an optimum energy at which temperature is maximum.

The carbon films were deposited on silicon and glass substrates at 1

cm away and parallel to the target surface at low laser irradiance under various helium pressures. The experiments were performed in a vacuum chamber. The laser radiation was focussed using a cylindrical lens to a spot of length 1.2 cm and breadth 0.04 cm. The deposited films were characterized using X-ray and Scanning electron microscopy (SEM). X-ray diffraction pattern of the carbon films deposited on silicon wafer at 100 Torr helium pressure showed peaks at 10.3°, 11°, 17.9° and 20° which corresponds to (100), (002), (110) and (112) crystalline planes of C_{60}. SEM photographs of the films deposited under various helium pressures showed that the density of the microcrystalline clusters increase with the increase in helium pressure. The ablated carbon powder 'soot' collected from the chamber at different helium pressures was analyzed for the presence of fullerenes, C_{60} etc.. The carbon clusters were characterized using UV-visible absorption and IR spectroscopic techniques. The optical absorption spectra showed prominent peaks characteristic of C_{60} and C_{70} clusters. Infrared spectrum showed prominent modes confirming the presence of C_{60}, C_{70} and C_{84} in the benzene / n-hexane solvable carbon soot.

ACKNOWLEDGEMENTS

Dedicated

To

My Parents

LIST OF PUBLICATIONS

1. Abhilasha, P.S.R. Prasad and R.K. Thareja, "Laser produced carbon plasma in an ambient gas", Phys. Rev. E 48, 2929 (1993).

2. P. S. R. Prasad, Abhilasha and R. K. Thareja, "Fullerenes from laser produced plasmas", Phys. Stat. Solids (a) 139, K1 (1993).

3. Abhilasha and R.K. Thareja, "Optical emission studies of molecular carbon", Phys. Lett. A 184, 99 (1993).

4. R.K. Thareja and Abhilasha, "C_2 from laser produced plasma", J. Chem. Phys. 100, 4019 (1994).

5. Abhilasha, R.K. Dwivedi and R.K. Thareja, "Wavelength dependence of the photoablation of carbon at low irradiance", J. Appl. Phys. 75, XXXX (1994).

6. R. K. Thareja, Abhilasha and Sampriti, "Fullerenes from pulsed laser ablated carbon plasma", Appl. Phys. Lett. submitted.

7. Abhilasha and R.K. Thareja, "Temporal profiles in laser ablated carbon plasma", J. Appl. Phys. submitted.

8. Abhilasha and R.K. Thareja, "Line emission enhancement in laser ablated carbon plasmas", to be submitted.

TABLE OF CONTENTS

LIST OF FIGURES

LIST OF TABLES

.

LIST OF SYMBOLS

D	Diffusivity
τ	Duration of the laser pulse
L_s	Latent heat of sublimation
I	Intensity of laser radiation
ρ	Density
m_j	Mass of species j
α	Vaporization constant
P_j	Vapour pressure
k_B	Boltzmann constant
T	Temperature
$\hat{T}$	Maximum surface temperature
$\hat{p}$	Vapour pressure in units of atm
ΔH_v	Heat of vaporization
ω_p	Plasma frequency
k	Wave propogation vector
n_e	Electron density
Z	Average charge
n_i	Ion density
h	Planck's constant
ν	Frequency
z	Distance perpendicular to the target surface
n_c	Critical density
c	Speed of light
t_{ei}	Electron ion thermalization time

A	Atomic mass number
$\ln \Lambda$	Coulomb logarithm for laser plasma
χ	Excitation potential
q	Charge
R_R	Radiative recombination rate
T_e	Electron temperature
R_C	Three body recombination rate
α_C	Three body recombination coefficient
α_R	Radiative recombination coefficient
u	Ion steaming velocity
σ	Cross section
$\bar{u}$	Mean velocity
γ	Specific heat capicity
E	Laser energy
p	Pressure
a	Accleration
f_o	Amplitude of disturbance
n	Constant related to the growth of the disturbance
M_o	Laser plasma mass
ρ_1	Density of laser ablated carbon plasma
ρ_2	Density of ambient gas
λ	Wavelength
A_{ij}	Transition probability
E_i	Excitation energy
g_i	Degeneracy of upper state
N_D	Number of particles in Debye sphere

W	Electron impact parameter
T_{vib}	Vibrational temperature
v'	Upper vibrational level
v''	Lower vibrational level
$I_{em}^{v'v''}$	Band head intensity
$F_{v'v''}$	Franck-Condon factor
$G(v')$	Term value of the upper vibrational level
D_{ν}	Correction factor
M_B	Mass of background gas atom
σ_{ea}	Elastic scattering cross-section
μ	Surface absorption index
$\dot{m}$	Mass ablation rate
K	Surface absorption coefficient

CHAPTER I

INTRODUCTION

Pulsed laser ablated plasma of a material is characterized by laser parameters (laser irradiance, pulse duration and wavelength) and temperature-dependent optical (reflectivity, absorption coefficient, penetration depth) and thermophysical (heat capacity, diffusivity, thermal conductivity etc.) properties of the target material.[1-5] When a laser pulse is incident on an opaque solid target, two extreme situations occur.[1,2] At very low irradiances the light causes only a rise in temperature by conduction below the surface with no change of phase. If the irradiance is very high, multi-photon ionization takes place at the surface eventually leading to plasma formation. Characteristic features of the laser ablated plasma such as temperature, velocity, forward-directed nature, pressure, presence of atomic, ionic and molecular species mainly depend on laser irradiance.[2] There are many reports on studies at various laser irradiances but a few reports[6,7] are available on the comparative study of low and high laser irradiance produced plasmas. Laqua[6] explained theoretically two different cases of vaporization depending on the irradiance; lower than 10^8 W/cm^2 and higher than 10^8 W/cm^2. In the first case, most of the material is removed in the form of polyatomic particles moving at a velocity of 10^4 cm/s. At higher irradiance, the temperature of the plasma is much higher than the boiling temperature of the material and the evaporated material i.e. atomic and ionic species move with velocity greater than 10^6 cm/s. Laser ablated plasma at low irradiance ~ 10^8 - 10^9 W/cm^2 is mostly used for pulsed laser deposition of thin films e.g. high T_c,[8] diamond like carbon[9] and polymeric thin films,[10] for microelectronic fabrication;[11] for studies of molecular species;[12] for production of carbon,[13]

sodium,[14] aluminium,[15] copper,[16] and other clusters; for surface temperature studies[17] etc.. Recent applications of the laser ablated plasma at moderate irradiance ~ 10^9- 10^{12} W/cm^2, includes source of X-rays,[18] VUV continuum[19] and highly charged ions,[20-22] for generation of laser oscillations,[23,24] understanding of hydrodynamics of plasma,[21,22,25] modelling of various processes in space physics,[26] particle injection in plasma devices for diagnostics,[27] sampling of materials for subsequent mass analysis,[11] and the studies of laser-plasma interactions in the presence of ambient gases.[28-30]

Laser ablated plasma has been recognized for a long time as a means to produce controlled beams of atomic species.[20,31] The laser produced plasmas from different targets have been extensively studied.[32] It has been found that ionic species from C I to C VI can be generated from laser ablated carbon plasma.[21,22] Detailed investigations of the temporal, spatial and spectral characteristics of various ionic species of carbon generated from a polyethylene film using pulsed ruby laser have been reported.[22,25] Electron density from stark broadened profiles and line intensity ratios have been reported.[25,33] Recently a laser imaging method has been developed for measurement of electron density fluctuations in plasmas,[34] and laser absorption spectroscopy has been used to measure the density of atomic niobium vapour in a laser ablated plume near the target surface.[35] Kinetic energy contribution for the different ionic species of carbon have been analyzed by Mann et al.[36] Kools et al[37] measured the angular velocity distribution of neutral copper atoms created by near-threshold ultraviolet excimer laser ablation of polycrystalline copper foils as a function of the laser fluence. There has been great interest in studying the interaction between charged ions emanating from expanding laser ablated plasmas with a background gas medium.

Various interaction processes such as recombination, collisional interactions, micro-instabilities etc. play an important role in line emission[30,38-39] in understanding the hydrodynamics of the expanding plasma[21,22] and in exploring the possibility of laser generated controlled thermo-nuclear reaction.[26] The interaction between laser plasma and the ambient gas approaching each other is also of interest because it provides information on collisional, collective and electromagnetic processes in astrophysical and laboratory plasmas[40] and can help in the solution of various practical problems.[12] The nature of interaction is governed by the densities, relative velocity, temperature, ion composition etc. of the plasma and background gas. There are some recent experimental reports on the study of the turbulent interactions of a hot expanding laser plasma with a low density background gas plasma.[41-44] The laser produced plasmas in an ambient gas are also being studied as a gain medium for x-ray lasers.[24] Seely et al[23] have used charge exchange scheme between C VI and Ar III in expanding carbon plasma for soft x-ray laser in carbon. Laser oscillations in the Balmer α-line[45] of C VI and in capillary discharge plasmas[24] have also been reported.

It has been experimentally shown that at laser intensity of 10^8 W/cm^2 molecular carbon emission dominates over ionic emission in laser ablated plasma plume.[46] Dreyfus et al[17] have reported molecular emission for copper (Cu_2) and carbon (C_2) from laser ablated plasma at low irradiance. Many laboratory studies have provided transition probability data and FrancK-Condon factors needed for diagnostic interpretation of the C_2 spectra in many astrophysical, gas dynamic and combustion applications.[47] C_2 molecule possesses seven known triplet and six known electronic states giving rise to nine band systems which lie across the vacuum ultraviolet, the visible and the

infrared spectral regions.[48] The strongest and most easily excited of these band systems is the Swan system which lies between 420 and 770 nm.[49] In a recent systematization of the energy level scheme and nomenclature for the C_2 molecule, Herzberg et al[48] assigned the notation $(d^3\Pi_g - a^3\Pi_u)$ for the Swan system. Several investigators have studied the C_2 emission during the laser sputtering of graphite.[50,51] Similar studies of C_2 Swan bands have been conducted for laser etching of polymers.[52-54] The Swan band system is an important spectroscopic feature of many different types of sources. It is prominent in flame-spectra,[55] in the emission spectrum from the comet heads[56] and electrical discharges through carbon bearing materials.[49] It is observed that C_2 emission is dominant[57] when high quality laser ablated unhydrogenated diamond like carbon films are deposited at low laser power densities. The properties of the films prepared by pulsed laser deposition depend on simultaneous control of various physical parameters during both deposition and cooling steps. In order to optimize film properties a better understanding of the dependence of film formation on the laser and plasma parameters is essential. It has been found that kinetic energy and temperature of the species deposited influence the growth of high quality films.[57] Therefore, it is necessary to estimate the temperature of the species which dominate in a deposited film. Various techniques have been utilized to estimate the temperature during dynamic changes in both temperature and free electron density in a laser produced plasma. The optimum films are obtained by the condensation of energetic atomic and molecular species.

Pulsed atomic, molecular or cluster beams produced by laser ablation of a solid target are widely used to study the elementary properties of non volatile elements[58] and to investigate different mechanisms such as

collisional and reactive processes. Laser vaporization in an ambient atmosphere has been used to produce clusters from polycyclic aromatic hydrocarbons, metals,[59] polymers,[10] and even soot particles.[13] Of all the elements for which gas phase clusters have been used, perhaps none has evoked more interest than carbon. It has been shown that the mechanism hypothesized for pure-carbon condensation in the graphite vaporization experiments also applies to soot formation in combustion.[55] The growing number of recent publications on clusters reflect the tremendous interest in these particles.[60] The individual crystals are intrinsically interesting since they often exhibit properties uncharacteristic of either the atomic state or the bulk. In addition, they are potentially of significant technical importance in the fields of catalysis and combustion, and are useful as models of surfaces.[61] Carbon clusters C_2, C_3, etc play important roles in the chemistry of cometary and stellar atmospheres[60] and in the formation of soot in rich combustion environments. Recently a hot band laser induced fluorescence study of the $A^1\Pi_u - X^1\Sigma_g^+$ transition in C_3 was performed.[62] Despite the interest in small clusters,[63] best of our knowledge of these species comes through theoretical calculations of their electronic and geometric structures.[64] Unfortunately detailed experimental data that could answer many questions, especially how these species are formed, is still largely lacking. Early work on carbon molecules/clusters was reported by Palmer and Shelef.[65] Major advances made in the recent past upto 1989 have been updated by Weltner and Van Zee[61] who have given a complete picture of the state of this field. Many researchers[66-68] have observed quite remarkable physical and chemical properties for even numbered carbon clusters in the size range of 2-100 atoms. Their unique properties lead to the hypothesis that these clusters adopt closed, spherical

structures.[69] The most symmetric structure is that of C_{60}, which is postulated to be a truncated icosohedral containing 12 pentagons and 20 hexagons. It is the third major form of pure carbon and has an unusual bonding behaviour, hollow symmetry and amazing electronic properties. C_{60} is so resistant to shock that it has been suggested as a lubricant. It is proposed that C_{60} may provide the added ingredient that makes diamond like carbon films more practical.[70] Properly doped C_{60} was found to be both superconducting and magnetic.[70] All aspects of C_{60}, buckminsterfullerene were comprehensively covered by Kroto et al.[71] Diederich et al[72] have presented a comprehensive review of higher clusters beyond C_{60}. Highly specific characterization methods[73] such as NMR and X-ray diffraction have been used to determine the structure and chemical properties of pure C_{60} and C_{70}. Mass spectroscopic methods using electron impact or laser ionization after laser desorption have been employed to estimate the mass distribution in C_{60} thin films.[74] Great interest still exists to determine the nonlinear properties and ionization potential of free C_{60} and C_{70}.[75]

For the formation of C_{60}, Kroto et al[76] has proposed that cluster closure satisfies the valences of the carbon atoms in the totally unsaturated molecules and make them relatively inert to reactions that lead to larger clusters and ultimately to particles. Thus the mechanism of condensation in the laser vaporization source is supposed to proceed via a spirally network of incompletely closed carbon shells.[76] Recently Wakabayashi et al proposed a ring-stacking model[77] which directly leads to the understanding of the formation mechanism of the stable fullerenes. They assumed that a closed carbon cage is formed by sequential stacking with appropriate numbers and combinations of only even-numbered carbon rings without any loss of carbon

atoms. As shown in Fig. 1 they showed that C_2 is necessary and dominant molecule for the formation and closed caging of fullerenes. C_{60} and C_{70} formation terminate by sequential addition of one and three C_2 units, respectively. C_{60} and C_{70} thus produced satisfy the requirement of I_h and D_{5h} symmetry, respectively.

Laser ablated plasma

For low laser irradiation ($\sim 10^6$ W/cm^2) the absorbed radiation appears as heat which is slowly distributed throughout the material by thermal diffusion.[1-5] For a conducting material, the incident energy is absorbed within a skin depth. At slightly higher irradiation ($> 10^6$ W/cm^2), depending on the thermal conductivity, thermal diffusivity, reflectivity of the target material and parameters of laser pulse, intense local heating of the surface will occur resulting in a rise in the surface temperature of the material.[1-5] As the irradiation increases, the temperature of the surface increases and a molten pool of depth $(D\tau)^{1/2}$ is formed,[5] where D is the diffusivity and τ is the duration of the laser pulse. A further increase in the irradiation will cause the surface temperature of the molten pool to reach boiling point resulting in evaporation. This will happen when the energy deposited is approximately equal to the latent heat of sublimation[5] L_s (erg/gm) $\simeq I \ \tau^{1/2}\rho^{-1}D^{-1/2}$, where ρ is the density of the solid target and I is intensity of laser irradiation. Once the vapours are formed, the laser light will cause further heating by multiphoton ionization and inverse bremsstrahlung resulting in a high temperature plasma. Figure 2 shows various phenomena occurring in laser ablated plasma as a function of laser irradiance. According to thermal model,[17] one requires that the peak surface temperature be sufficiently high
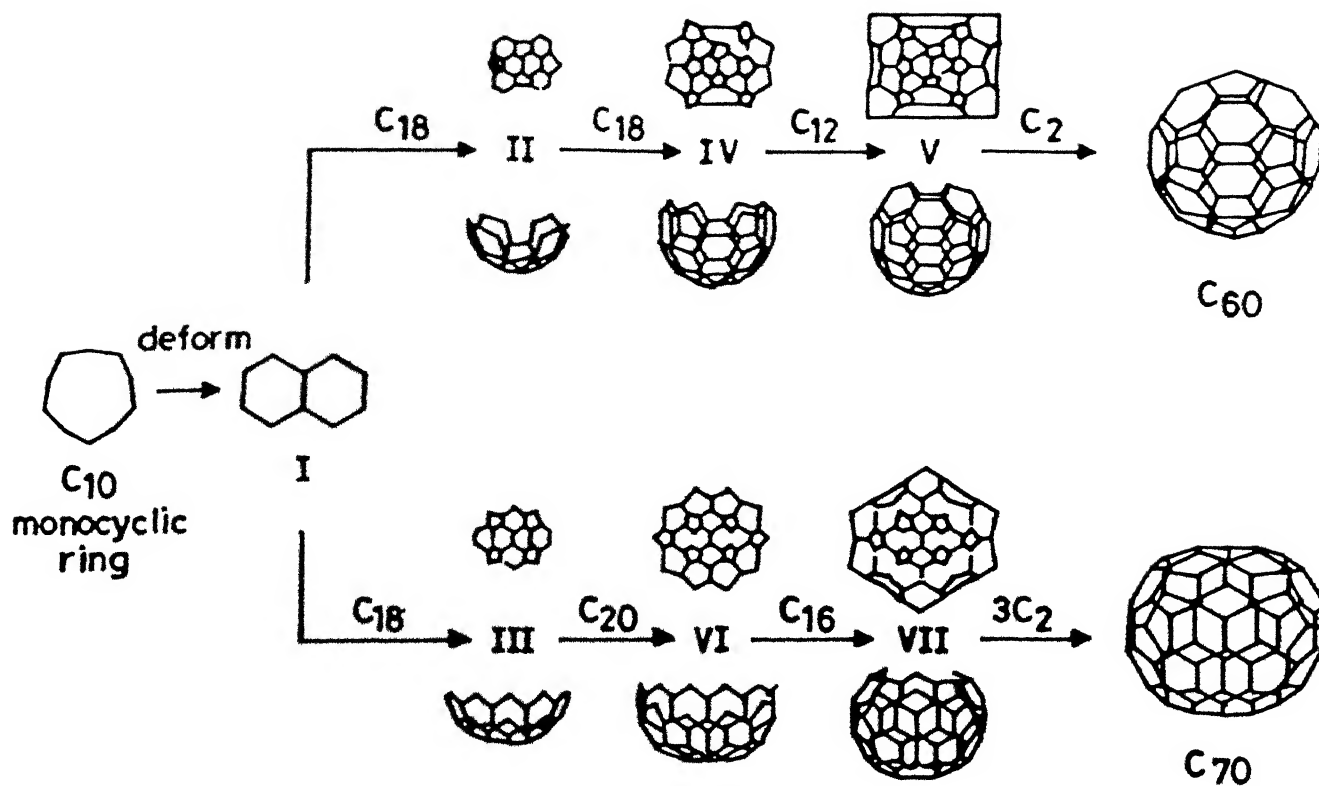
Fig. 1   Schematic drawings of the ring-stacking processes for C_{60} and C_{70} formations.

LASER INTENSITY

$\propto 10^6$ W/cm^2

$10^6 - 10^7$ W/cm^2
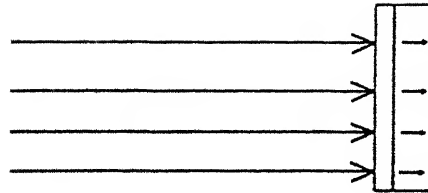
$\geq 10^8$ W/cm^2

Absorption

Thermal Conduction
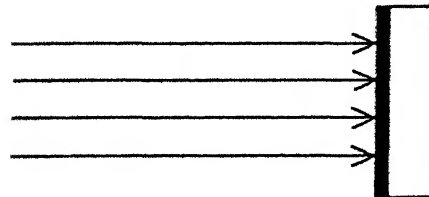
Surface Melting
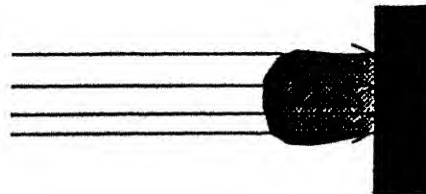
Vaporization

Multiphoton Ionization

Plasma Production

Fig. 2   Various phenomena occurring in laser ablated plasma as a function of laser irradiance.

so that vaporization can occur during the laser pulse. Due to vaporization the target material erupts out leaving a crater on the solid surface. This process is known as laser ablation. The amount of material ablated/removed and the shape of the crater are influenced by the laser parameters. The material removed per pulse[17] is given by

$$\text{mass loss per unit area} = \sum_{j} \int dt \ m_j \ \alpha \ P_j (2\pi m_j k_B T)^{-1/2} \qquad (1)$$

where m_j is the mass of species j, α is vaporization coefficient, P_j is the vapour pressure, k_B is Boltzmann constant and T is the temperature. The extent of vaporization per pulse[78] is given by

$$\text{distance (nm)/pulse} = (\alpha \ \hat{P} \ \hat{T}^{1/2}\tau \ / \ M^{1/2}\Delta H_v) \times 1.53 \times 10^6 \qquad (2)$$

where $\hat{T}$ is the maximum surface temperature, $\hat{P}$ is vapour pressure in units of atm at $\hat{T}$, M is molecular weight, and ΔH_v is the heat of vaporization. Equation (2) is valid only if $\hat{T}$ is well below the critical temperature so that vaporization is limited to the surface. It is found that the temperature required for graphite to vaporize 0.04 to 1 nm/pulse ($\hat{P}$ ~ 60 atm) is about 4000 K, whereas Al_2O_3 requires ~ 4800 K to remove 1.5 nm, while polymers decompose in nanosecond at temperatures near 2000 K.[17] At irradiance of 10^8 W/cm^2 onto a target it is possible to produce the plasma directly due to direct vaporization of the solid without going through the intermediate steps. At low irradiance plasma emission comprises of vibrational bands from molecular species. In laser ablated carbon plasma, molecular carbon C_2 Swan band emission dominates[46,57] at low irradiances (~ 10^8 W/cm^2), whereas at higher irradiance (~ 10^{11} W/cm^2) atomic/ionic species from C I to C V are observed.[21,79] Figure 3 shows the energy level diagram of C_2 Swan bands[80] and
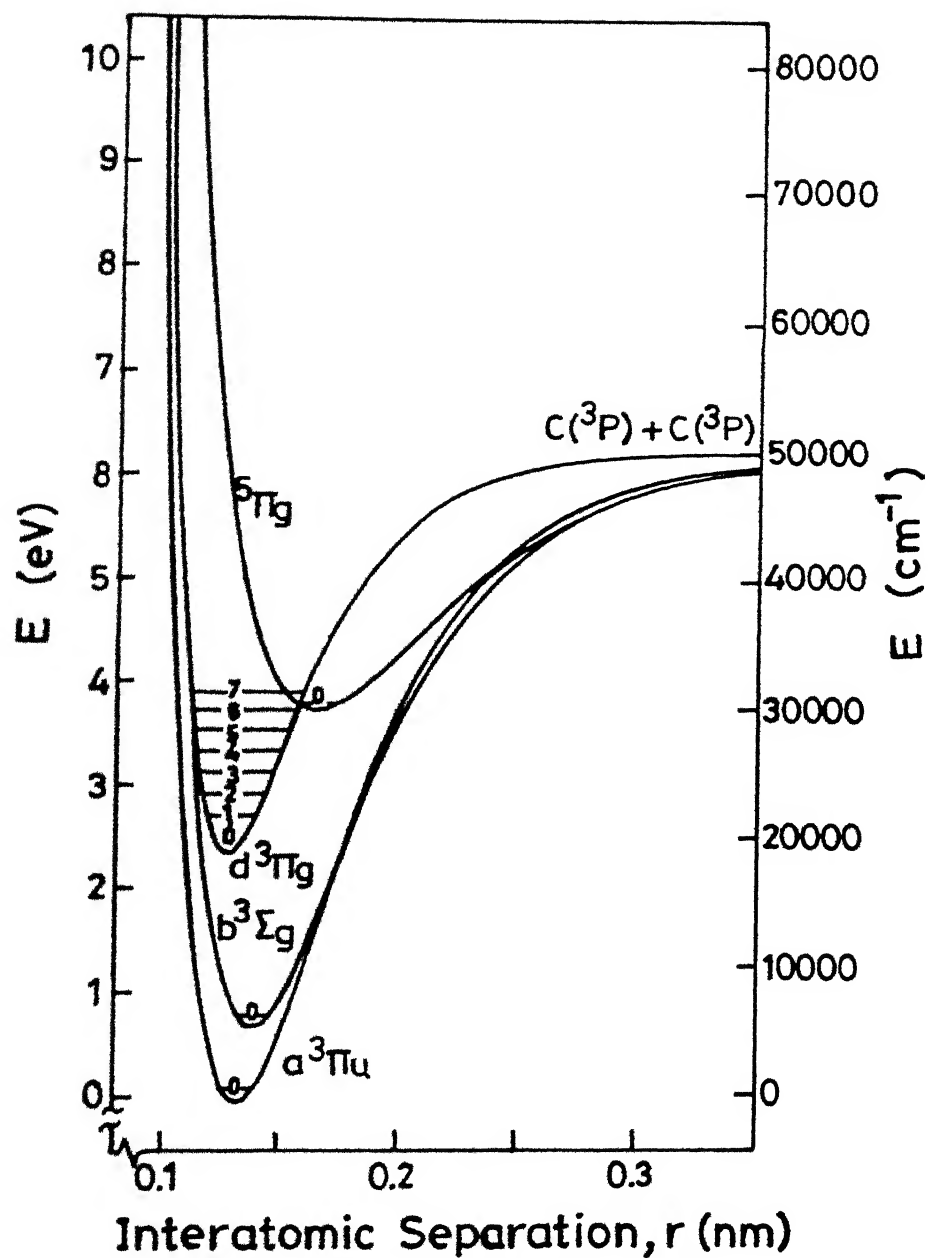
Fig. 3   Partial Potential Energy diagram for C_2 Swan bands.

Figs. 4 and 5 show the partial grotrian energy level diagrams of various carbon transitions observed in our experiments. Recently Optical emission of C_2 Swan bands ($d^3\Pi_g$ - $a^3\Pi_u$) and CN bands produced from the etching of diamond like carbon films using KrF excimer laser has been reported.[54]

At moderate laser irradiance[3] ($\sim 10^9$-10^{12} W/cm^2), direct ionization of the target material takes place and a short lived, optically moderately thick hot plasma is created at the focus on the target which tends to shield the target surface. Dispersion relation for an electromagnetic wave travelling through a plasma[1] is given by $\omega^2-\omega_p^2 = k^2c^2$ where ω_p is plasma frequency, $\omega_p = \sqrt{\dfrac{4\pi n_e e^2}{m_e}}$, c the speed of light, k the propagation vector and n_e is the electron density. If an electron density gradient exists as in a laser produced plasma, ω_p varies according to $\omega_p \propto \sqrt{n_e}$. For $\omega > \omega_p$, k is real and the electromagnetic wave propagates whereas for $\omega < \omega_p$, k is imaginary and the wave is not propagated. At $\omega_p = \omega$, reflection of laser light occurs at the density called the critical density $n_c = m_e\omega^2/4\pi e^2$. Most of the absorption of laser energy occurs at or close to n_c. Laser light is absorbed in the plasma by an inverse bremsstrahlung process which occurs due to electron-ion collisions in the plasma. The absorption coefficient being given by[2]

$$K_\omega = 3.69 \times 10^8 \ (Z^3 \ n_i^2/ \ T^{0.5} \ \nu^3)[\ 1 - \exp(-h\nu/k_B T_e) \ ] \qquad (3)$$

where Z, n_i and T are respectively the average charge, ion density, and temperature of the plasma; h and ν are the Planck's constant and frequency of the laser light, respectively. The laser energy is highly absorbed if ($K_\omega z$) is large, where z is the distance perpendicular to the target of the expanding plasma. In Eq. (3) it is assumed that the plasma frequency is smaller than the frequency of the laser wavelength, otherwise, all the radiation would be
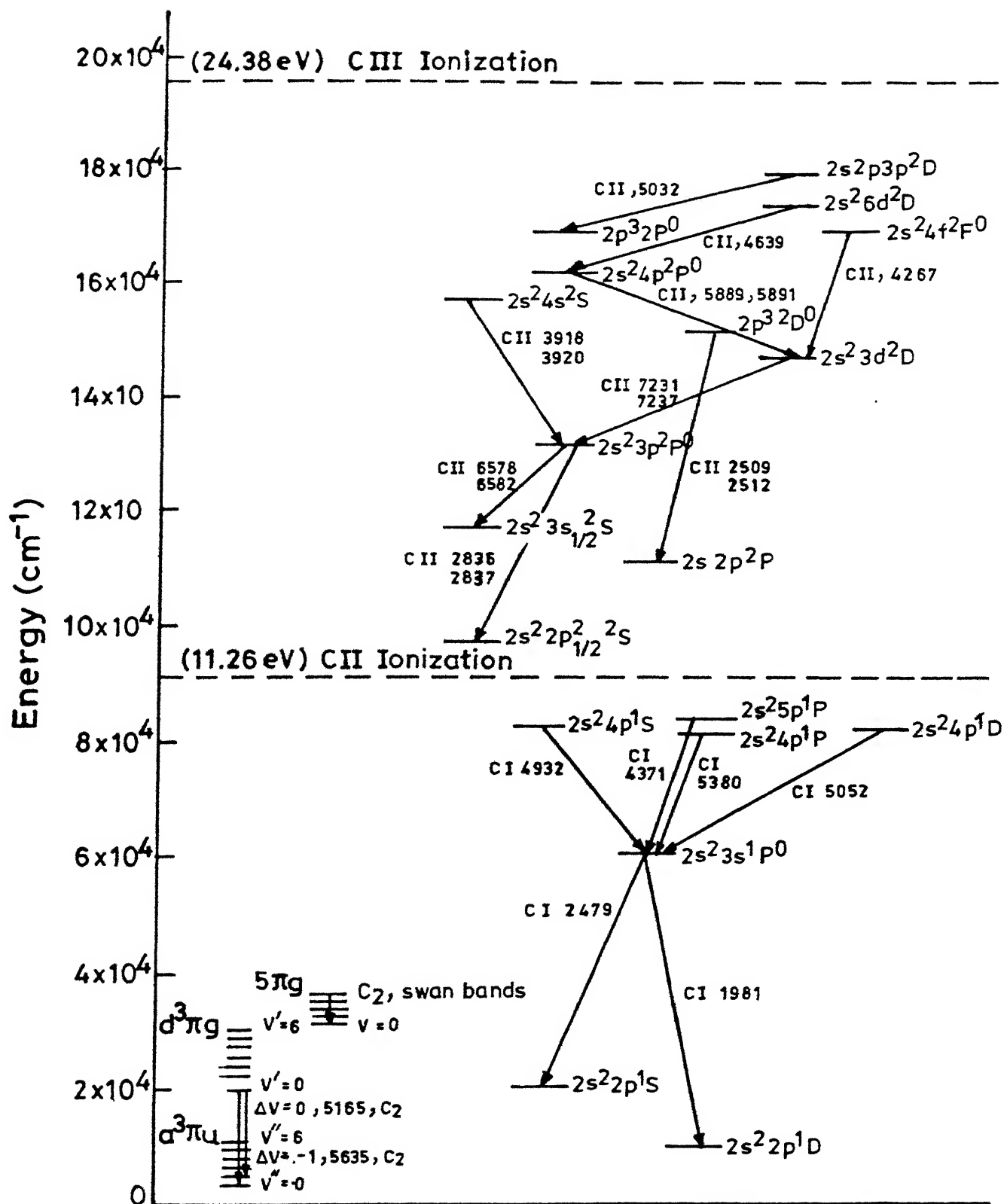
Fig. 4 Partial grotrian energy level diagram of C_2, C I and C II species (Wavelengths of the transitions are in Å).
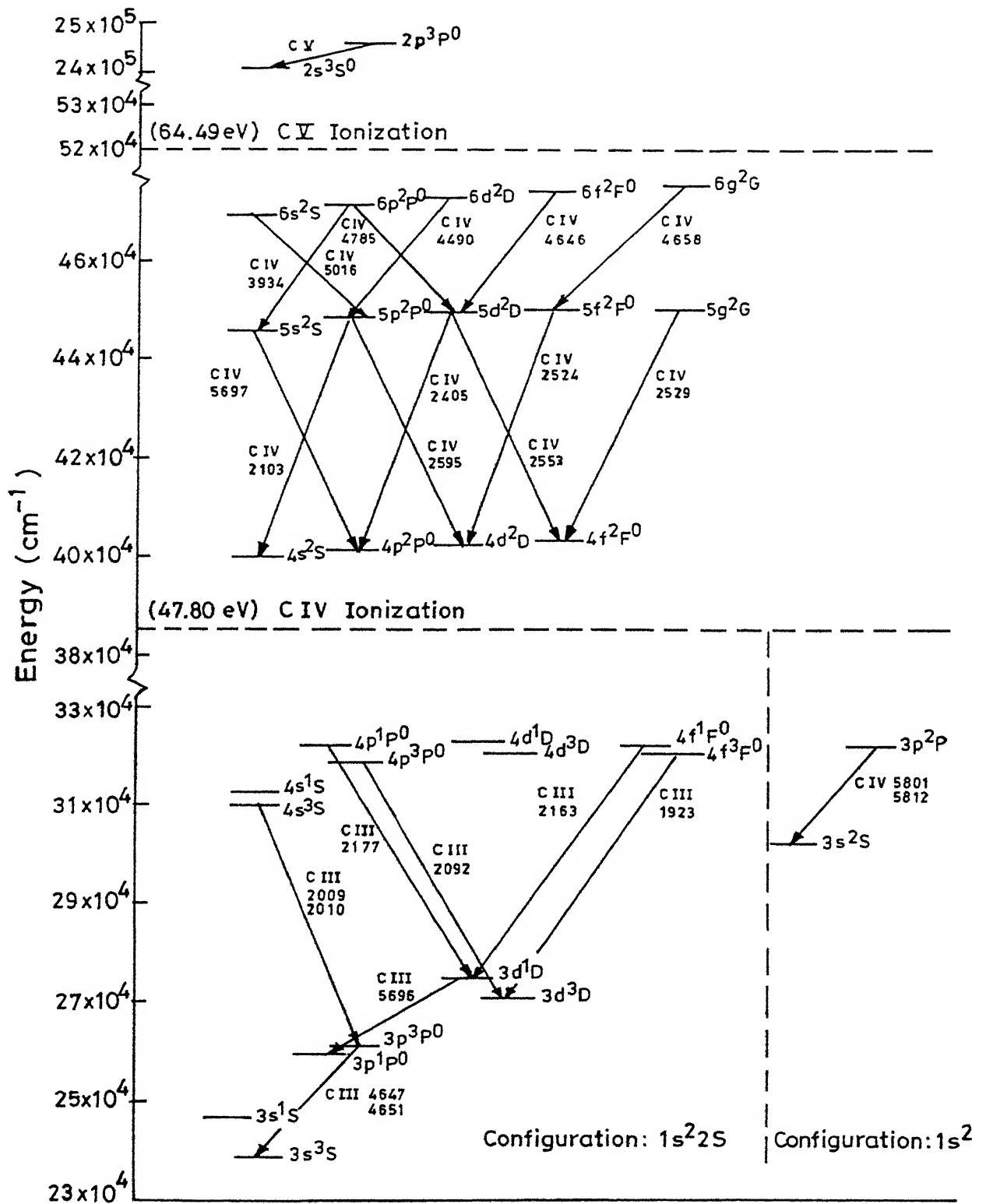
Fig. 5 Partial grotrian energy level diagram of C III, C IV and C V species (Wavelengths of the transitions are in Å).

reflected by the plasma. Equation (3) shows that the rate of absorption depends on n_i^2. The absorbed energy causes an increase in the kinetic energy of the electrons, i.e. an increase in electron temperature and this inturn produces further ionization with a consequent increase in n_e. Hence the rate of absorption and with it the rate of ionization escalates so that n_e increases further and eventually approaches n_c at which stage the critical density is established across a surface some distance into the plasma. At this surface the plasma becomes opaque to the incoming radiation which is therefore reflected outwards again and in the layers immediately in front of the surface (where $\omega_p \rightarrow \omega$) the absorption coefficient becomes very large. When the plasma becomes opaque laser radiation can no longer reach the surface of the target to generate new plasma by evaporation and ionization. Plasma growth however does not cease. Because of the heating which follows the absorption of energy by inverse-bremsstrahlung the plasma is driven rapidly away from the target surface, consequently the electron density decreases and the laser radiation again reaches the target.[81] In laser heated solid targets, the inward flow of thermal energy towards cold, high density solid regions produces a compensating outward flow of plasma kinetic energy towards lower density regions i.e. away from the solid target surface as shown in Figs. 6 (a) and (b). These processes do not take place discontinously but merge into a smooth self regulating regime with the generation, heating and expansion of plasma taking place throughout the length of the laser pulse. This is the self-similar model for the plasma expansion.[3] The energy absorbed by the electron equilibriates very rapidly so that a well defined electron temperature is established. The energy gained by the electrons is also shared with ions in collisions, the time required to attain equilibrium (the
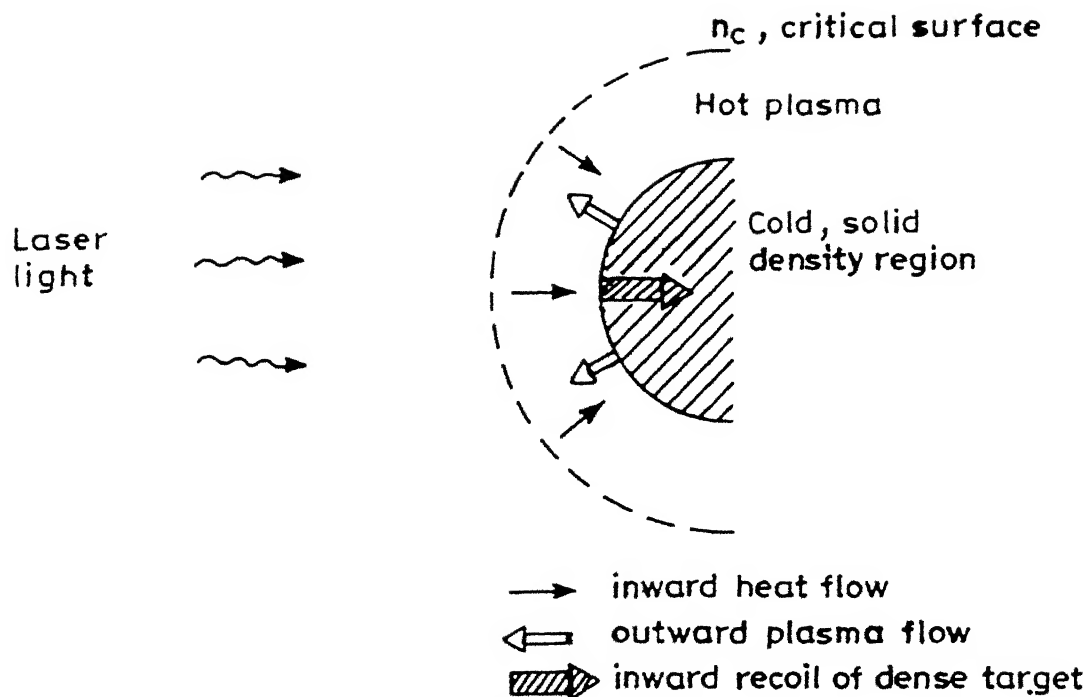
Fig. 6(a) Schematic diagram of the critical surface.
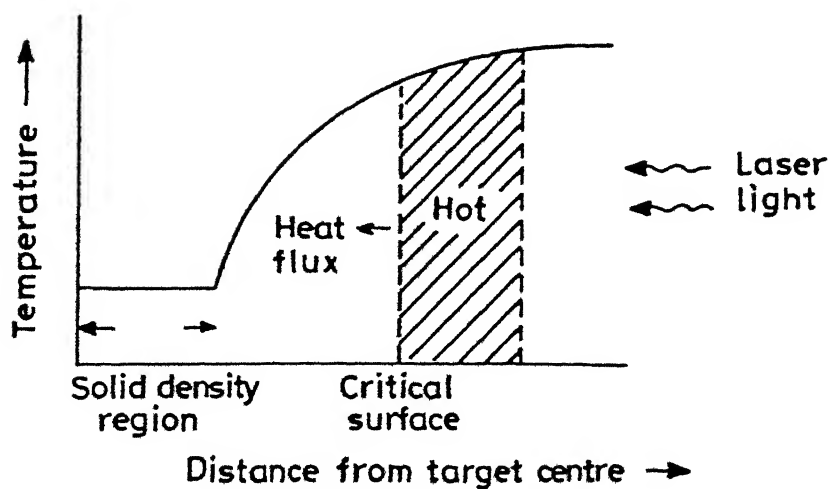
Fig. 6(b) Temperature versus distance from the centre of the target.

electron - ion thermalization time) is given by[81]

$$t_{ei} = 2.52 \times 10^8 \; \frac{AT_e^{3/2}}{n_e Z^2 \ln \Lambda} \quad (s) \tag{4}$$

where A is the atomic mass number and $\ln \Lambda \approx 10$ represents the Coulomb logarithm for the laser plasma. For laser produced carbon plasma, t_{ei} is considerably less than the duration of a Q - switched laser pulse and so a good degree of thermalization is expected in the plasma.

At higher irradiances ($>10^{12}$ W/cm^2) the plasma is generated and heated to a very high temperature in a thin absorbing layer at the surface of the dense region and has only a small optical thickness, so the self regulating regime no longer exists. Absorption becomes non-collisional and takes place via resonance mode conversion at critical density. The absorbing surface of the dense region moves into the target as a laser heated deflagration wave. This regime has been investigated in one dimension by Fauquignah et al.[82] These plasmas are used for studying dynamics of strongly coupled plasmas,[40] short wavelength lasers[24] and for astrophysical like plasmas.[40] The laser ablated plasmas have quite unusual properties. The plasma density is extremely high compared with that of other laboratory plasmas. It ranges from about 10^{17}-10^{23} cm^{-3} depending on the wavelength and intensity of the radiation. With temperature of about 1 keV condition close to those in the interior of the sun are realized. The pressure in such plasmas reaches as high as 10^8 atm. These are very fast recombining plasmas with a velocity of about $\sim 10^7$-10^9 cm/s.

Equilibrium in plasmas

In complete thermodynamic equilibrium[81] (with both kinetic and

radiative equilibrium at the same temperature T) every atomic process occurring in the plasma is balanced by an equal and opposite process. In this case the following conditions are satisfied: (a) all particles, electrons, neutral species and ions obey the Maxwell velocity distribution law; (b) the population distributions over the states of any atom or ion are given by the Boltzmann formula; (c) the number of ions in stage Z relative to the number in stage (Z-1) is given by the Saha equation; (d) the intensity distribution of the radiation as a function of frequency and temperature is given by the Planck's formula. All these conditions are characterized by the same temperature T. Rarely, especially in terrestrial plasmas is perfect thermodynamic equilibrium approached; the very fact that radiation is emitted from a plasma prevents thermodynamic equilibrium from occurring.

The commonest plasma model is that which conforms to local thermodynamic equilibrium (LTE). In LTE it is assumed that collisional events, in particular the events involving electrons, determine the behaviour of the system. The collisions are assumed to be governed by the same laws that hold in total thermodynamic equilibrium. The temperature used is the electron temperature, T_e, since electrons dominate the collisional process. The radiation distribution however is not given by Planck's equation and radiative effects are assumed to play an insignificant role in determining the equilibrium in the plasma. For LTE to hold the electron density must be sufficiently high. According to McWhirter,[81] for LTE to hold n_e, the number of electrons per cm^3 must satisfy;

$$n_e \geq 1.6 \times 10^{12} \, T_e^{1/2} \, \chi^3, \qquad\qquad (5)$$

where χ is the excitation potential (in eV) of the transition.

At low electron densities a second limiting type of equilibrium called coronal equilibrium (so called because it describes conditions in the solar corona) may be attained. In this case excitation and ionization occur as the result of electron collisions whereas de-excitation and recombination occur by the emission of radiation. The plasma is assumed to be optically thin so that re-absorption of the emitted radiation is negligible.

Laser ablated plasma in the presence of an ambient gas

When a fast laser-ablated plasma flows into an ambient media (Fig. 7), interstreaming plasma interactions, much like those found in many space and astrophysical situations occur.[40] At low background gas pressure (p < 1 Torr) a large fraction of the ions stream through the background gas depositing very little of their energy. Whereas at higher pressure (> 1 Torr) of the ambient gas essentially all of the kinetic energy of the ions is lost in collisions with the background gas particles that occur within a very small volume near the target resulting in a shock/blast wave structure.[83]

The interaction of the laser plasma with the ambient gas results in various processes such as recombination interactions, collisional and collisionless interactions, shock/blast wave interactions, microinstabilities in the laser plasma, turbulent interactions etc.. Various processes are discussed in brief below.

Recombination process

When a positive ion collides with an electron or a negative ion, electron transfer between the colliding particles results in neutralization of the charge on the positive ion, the process is known as recombination.[84] The recombination can occur either due to the radiative or three body
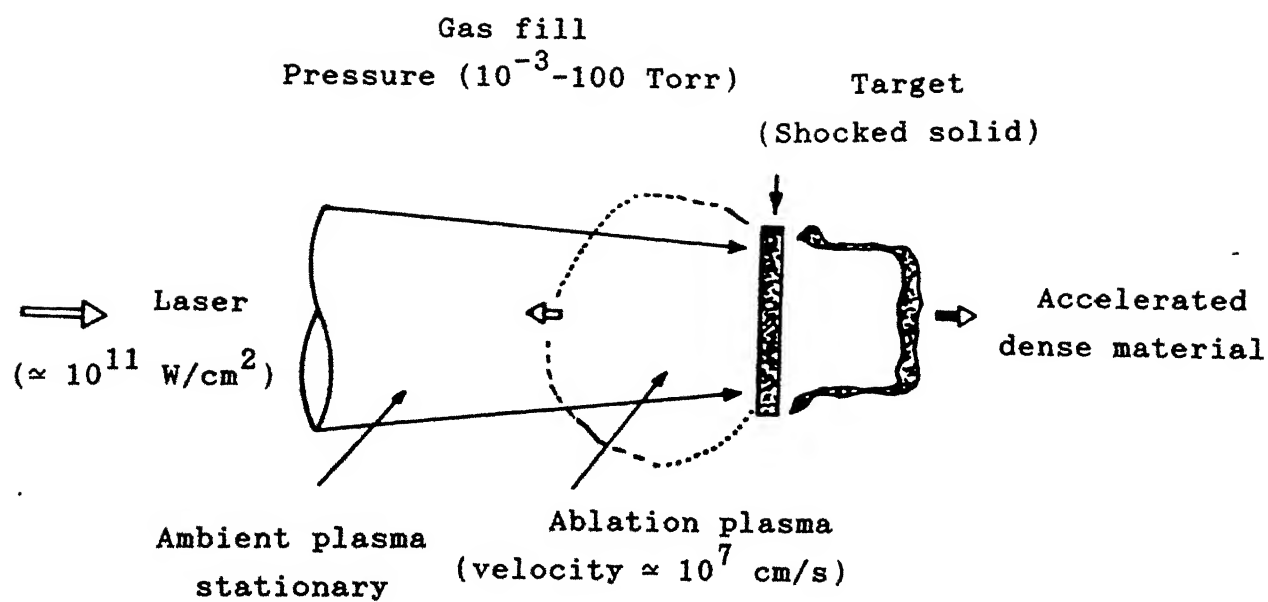
Fig. 7   Fast laser ablated plasma in the presence of an ambient gas.

recombination.[85,86] For the radiative recombination

$$C^{q+} + e = C^{(q-1)+} + h\nu$$
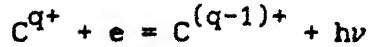
The radiative recombination rate R_R being given by

$$R_R = \left(\frac{dn_e}{dt}\right)_R = -\alpha_R n_e n_i \tag{6}$$

where α_R is the radiative recombination coefficient,

$$\alpha_R = 2.7 \times 10^{-13} \, Z^2 \, T_e^{-3/4} \quad cm^3/s \tag{7}$$

where n_e and n_i are the electron and ion densities, respectively; T_e is electron temperature in eV and Z is ionic charge. Three body recombination process is defined as

$$C^{q+} + e + e = C^{(q-1)+} + e$$
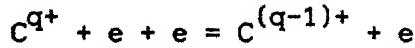
Three body recombination rate R_C being given by

$$R_C = \left(\frac{dn_e}{dt}\right)_C = -\alpha_C n_e^2 \, n_i \tag{8}$$

where α_C is the three body recombination coefficient

$$\alpha_C = 9.2 \times 10^{-27} \, Z^3 \, T_e^{-9/2} \ln \left[(Z^2 + 1)^{1/2}\right] \quad cm^6/s \tag{9}$$

From Eqs. (6) and (8) it follows that radiative process is important only close to the target and the three body recombination is a dominant phenomenon beyond a few mm from the target surface.

Charge Transfer

When an ion enters into the vicinity of a neutral/ionic particle, there is a finite possibility that an electron may be transferred from the neutral/ionic particle to the other ion and thereby exchange of charge takes

place.[84] This process is referred to as charge transfer and is represented by

$$X^+ + Y \longrightarrow X + Y^+ \pm \Delta E \tag{10}$$

The quantity ΔE is called the energy defect in the electronic collision. The energy dependence of the cross section for a particular charge-transfer reaction depends markedly upon the magnitude of the energy defect. The charge-exchange rate of ions is given by the relation

$$R = n_i < u\sigma > \tag{11}$$

where u is ion streaming velocity, σ is cross-section for the charge transfer. The cross section for the ion-ion charge transfer interaction is given by[84]

$$\sigma(Z_1, Z_2) = \frac{4 \pi Z_1^2 Z_2^2 e^4 \ln\Lambda}{\mu^2 \bar{u}^4 \left(1 + \frac{m_2}{m_1}\right)} \tag{12}$$

where index 1 refers to the laser plasma ions, 2 to the ambient gas ions, Z is charge number, $\ln\Lambda \approx 10$ is the Coulomb logarithm for the laser plasma, $\bar{u}$ the mean velocity of laser plasma ions, m the mass of ion and μ the reduced mass of ions. The cross-section σ, for the conditions of our experiment is equal to $\approx 10^{-18}$ cm^2. Seely et al[23] have examined the charge exchange process in detail occurring between C VII and Ar III in expanding laser produced carbon plasma.

Shock/Blast Wave

When a powerful, short-pulsed laser beam is focussed onto a solid target located in a high pressure ($\geq$ 1 Torr) ambient gas, the target plasma rapidly expands supersonically against the background gas and a shock wave is formed at the plasma-gas boundary. The background gas is compressed into a relatively thin shell at the shock front. As the shock front expands, more and

more background gas is swept up by the shock wave and the expansion velocity of the laser produced plasma decreases. If the ultraviolet (UV) radiation emitted by the hot plasma penetrates and photoionizes some of the background gas surrounding it, plasma shock wave may occur between the expanding laser produced plasma and the ionized background gas. This kind of non-steady shock wave is called a blast wave. At sufficiently long time after the laser heating of the plasma stops, the plasma/gas shock boundary moves according to blast wave theory. Using Sedov's approach,[87,88] the motion of the blast wave front is governed by the relation,

$$z = \phi_0 \left(\frac{E}{\rho} \right)^{1/5} t^{2/5} \qquad (13)$$

where ϕ_0 is a constant which depends on γ, the specific heat capacity of the expanding gas, E is the laser energy and ρ the density equivalent to the gas pressure.

Micro-Instability

A hydrodynamic instability called Rayleigh-Taylor instability (RTI)[89,90] occurs at the interface when two fluids of different densities are accelerated in a direction perpendicular to their interface, this interface is stable or unstable according to whether acceleration is directed from heavier to the lighter medium or vice versa. The RTI causes ripples to grow in amplitude until the fluids interpenetrate each other as bubbles (lower density fluid) and spikes (higher density fluid). Theoretical[91] and experimental[92] studies have shown that the conditions favoring hydrodynamic instability may be established during the deceleration of a propelling gas (e.g. a laser plasma) at an interface.[42,79]

For deriving the necessary and sufficient condition[89,90] so that a

stratified heterogeneous fluid is stable or unstable, we consider a static state in which an incompressible fluid of variable density is arranged in vertical strata and the pressure p and the density ρ are functions of the horizontal coordinate ζ only. The character of the equilibrium of this initial static state can be determined by supposing that the system is slightly disturbed and then by following its further evolution.
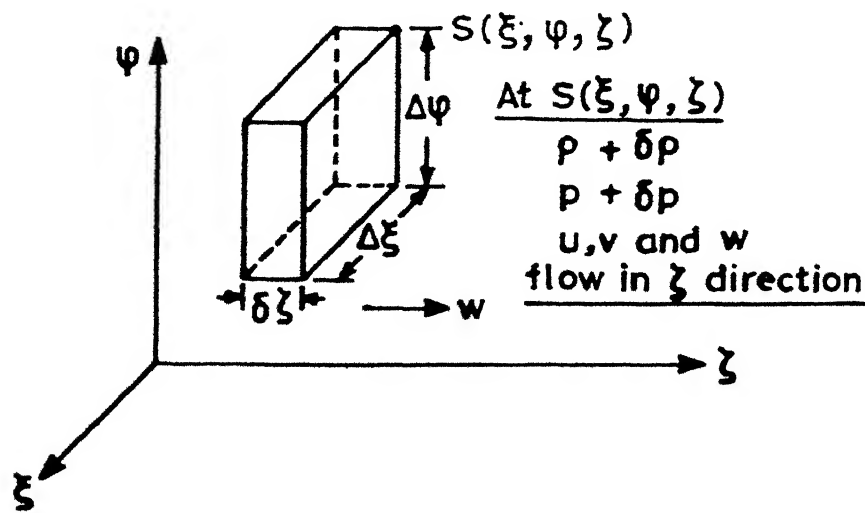
Let the actual density at any point $S(\xi,\psi,\zeta)$ as shown above as a result of the disturbance be $\rho+\delta\rho$; and let $\delta\rho$ denote the corresponding increment in the pressure. Let ω denote the small component of the velocity. The equations of motion and continuity are

$$\rho \frac{d\omega}{dt} = - \nabla(\delta p) - a \, \delta\rho \, \hat{\zeta} \tag{14}$$

and

$$\frac{\partial}{\partial t} \delta\rho + \nabla(\omega \, \delta\rho) = 0 \tag{15}$$

where a is the acceleration and $\hat{\zeta}$ is a unit vector in the ζ - direction.

For an incompressible fluid $\nabla\omega = 0$ (16)

Using Eq. (16), we get from Eq. (15)

$$\frac{\partial}{\partial t} \, \delta\rho \, + \, \omega \, \nabla(\delta\rho) \, = \, 0, \tag{17}$$

which ensures that the density of fluid remains constant. Writing equations for the components of velocity (ω) i.e. u, v and w in the ξ, ψ, and ζ-directions respectively, we get from Eqs. (14),(16) and (17)

$$\rho\frac{\partial u}{\partial t} = -\frac{\partial}{\partial \xi}\delta p, \quad \rho\frac{\partial v}{\partial t} = -\frac{\partial}{\partial \psi}\delta p, \quad \rho\frac{\partial w}{\partial t} = -\frac{\partial}{\partial \zeta}\delta p - a\delta\rho, \tag{18}$$

$$\frac{\partial u}{\partial \xi} + \frac{\partial v}{\partial \psi} + \frac{\partial w}{\partial \zeta} = 0, \tag{19}$$

and $\qquad \dfrac{\partial}{\partial t} \, \delta\rho \, = \, -\, w\dfrac{d\rho}{d\zeta} \tag{20}$

The stability of the system means stability with respect to all possible (infinitesimal) disturbances. Accordingly it is necessary that the reaction of the system to all possible disturbances be examined. This is normally done by expressing an arbitrary disturbance as a superposition of certain basic possible modes and examining the stability of the system with respect to each of these modes. So, considering small perturbations described by

$$f(\xi,\psi,\zeta,t) = f_o\exp \, (ik_\xi\xi + ik_\psi\psi + ik_\zeta\zeta + nt)$$

where f_o is amplitude of the disturbance, k_ξ, k_ψ and k_ζ are wavevectors in the ξ, ψ, and ζ-directions and n is a constant related to the growth of the disturbance. In this system the physical variables are functions of the ζ-coordinate, hence analyzing the disturbance in terms of two-dimensional (ξ and ψ) periodic waves and ascribing all the physical quantities describing the perturbation a dependence on ξ, ψ and t of the form

$$\exp \, (ik_\xi\xi + ik_\psi\psi + nt) \tag{21}$$

where $k = \sqrt{(k_\xi^2 + k_\psi^2)}$ is the wavenumber associated with the disturbance.

Substituting Eq. (21) in Eqs. (18)-(20), we get

$$ik_\xi \delta p = -n\rho u, \quad ik_\psi \delta p = -n\rho v, \quad \frac{d}{d\zeta}\delta p = -n\rho w - a\delta p \tag{22}$$

$$ik_\xi u + ik_\psi v = -\frac{dw}{d\zeta} \tag{23}$$

$$n\delta p = -w\frac{d\rho}{d\zeta} \tag{24}$$

Multiplying first and second part of Eq. (22) by $-ik_\xi$ and $-ik_\psi$, respectively, and making use of equation (23), we obtain

$$k^2\delta p - n\rho\frac{dw}{d\zeta} = 0 \tag{25}$$

From third part of Eq. (22) and Eq. (24) we get

$$\frac{d}{d\zeta}\delta p = -n\rho w + \frac{a}{n}\frac{d\rho}{d\zeta}w \tag{26}$$

From equations (25) and (26) we get

$$\frac{d}{d\zeta}(\rho\frac{dw}{d\zeta}) = k^2\rho w - \frac{K^2}{n^2}\frac{d\rho}{d\zeta}w \tag{27}$$

Now considering the case of two uniform fluids of constant densities ρ_1 and ρ_2 separated by a vertical boundary at $\zeta = 0$, so $\frac{d\rho}{d\zeta} = 0$ and for both regions of the fluid, the general Eq. (27) reduces to

$$\frac{d^2w}{d\zeta^2} - k^2w = 0 \tag{28}$$

the general solution of which is

$$w = Ae^{+k\zeta} + Be^{-k\zeta} \tag{29}$$

Since w must vanish both when $\zeta \longrightarrow -\infty$ (fluid at $\zeta <0$) and $\zeta \longrightarrow +\infty$ (fluid at $\zeta > 0$), we suppose,

$$w_1 = -Ae^{+k\zeta} \qquad (\zeta < 0) \tag{30}$$

$$w_2 = Ae^{-k\zeta} \qquad (\zeta > 0) \tag{31}$$

The boundary conditions at an interface are w, $\frac{dw}{d\zeta}$ must be continuous across an interface and $\frac{d^2 w}{d\zeta^2}$ must be bounded at an interface. Integrating Eq. (27) over an infinitesimal element of ζ including $\zeta = 0$,

$$\int_{\zeta=0} \frac{d}{d\zeta} \left(\rho \frac{dw}{d\zeta} \right) d\zeta = \int_{\zeta=0} k^2 \rho w d\zeta - \frac{a \, k^2}{n^2} \int_{\rho_1}^{\rho_2} \left(\frac{d\rho}{d\zeta} w \right) d\zeta \qquad (32)$$

From Eqs. (30) and (31) we get

$$- k w_0 (\rho_2 + \rho_1) = - \frac{a \, k^2}{n^2} (\rho_2 - \rho_1) \, w_0 \qquad (33)$$

where w_0 is the common value of w at $\zeta = 0$.

From Eqs. (32) and (33) the growth of instability[87,88] is given by

$$n^2 = ak \frac{(\rho_2 - \rho_1)}{(\rho_2 + \rho_1)} = akC \qquad (34)$$

The growth time of perturbations is proportional to $(akC)^{-1/2}$. If $n^2 > 0$, the interface is stable while if $n^2 < 0$, perturbation grows exponentially and interface is unstable. The growth of instability occurs in the maximum acceleration region. Considering the two fluids to be laser ablated carbon plasma and the ambient gas, a_{max} can be estimated from the derivative of momentum conservation equation

$$\frac{d}{dt} \left[\left(M_0 + \frac{4}{3} \pi R^3 \rho_2 \right) u \right] = 0 \qquad (35)$$

where M_0 is the laser plasma mass, ρ_1 is density of laser ablated carbon plasma, ρ_2 is density of ambient gas, u is plasma front velocity and R is the distance from the target, assuming ρ_2 and M_0 are constant with time, solution of Eq. (35) yields

$$a_{max} = \frac{-2u^2}{3R} \qquad (36)$$

Using Eq. (36) in Eq. (35) we get

$$\rho_2 = \frac{6\ M_0}{28\ \pi\ R^3} \tag{37}$$

where R is the distance from the target where acceleration is maximum at which interface formation and instability occurs.

Present Work

In the present work we report the studies of laser ablated carbon plasma produced using Nd:YAG laser (DCR-4G, Spectra Physics) and its harmonics $2\omega_0$, $3\omega_0$ and $4\omega_0$ at moderate and low laser irradiances in vacuum as well as in the presence of ambient gases. Studies on characterization of laser ablated carbon powder 'soot' and laser deposited carbon films using various techniques are also reported.

The details of the experimental techniques used in the present work are described in chapter II.

Chapter III describes the results of laser ablated carbon plasma in vacuum and in presence of gases such as helium, argon and air at moderate intensities.[79] A Nd:YAG laser was used for plasma production. Assuming the plasma to be in local thermodynamic equilibrium electron temperature is estimated from the line intensities of various transitions. The estimated temperature is in the range $2 \leq k_B T_e \leq 10$ eV. The electron density is estimated by measuring the stark width of C II transition 3p $^2P^0$ - 4s ^2S at 392.0 nm. The temporal profiles of C II, C III and C IV species were recorded to estimate the velocity of the plasma front. In the presence of helium and argon gases, the role of recombination in enhancing the line emission of various ionic species is discussed. An appearance of a peculiar double peak

structure in the temporal profiles of the C II transition 3d ^{2}D - 4f ^{2}F^0 at

426.7 nm in a laser produced carbon plasma as it expands into a background

medium is reported. It is proposed that at the interface region between carbon

ions and background gas due to density fluctuations, Rayleigh-Taylor

instability may occur in the laser plasma front which leads to stratification

of the plasma into fast and slow components.

Chapter IV gives the details of the studies of laser ablated carbon

plasma at low laser irradiances.[46,93] C_2, Swan band emission spectra were

recorded using various laser wavelengths at various laser intensities in

vacuum and at various helium gas pressures in the range 10^{-3} to 100 Torr. The

presence of helium gas increased the intensity of the emitted spectrum and all

band heads. The C_2 vibrational temperature calculated from Swan band heads is

found to be in the range 6000 K to 12000 K. Temperature and the velocity of

the C_2 species decrease with the increase in helium pressure. It is found that

shorter laser wavelength irradiation produces higher vibrational temperature

at all helium pressures.[94]

In Chapter V we report the presence of carbon clusters (fullerenes)

in laser ablated carbon soot and pulsed laser deposited carbon films obtained

from vaporization of graphite in a helium atmosphere.[95,96] X-ray, UV-visible

and infrared spectroscopy and scanning electron microscopy were used to

characterize the carbon clusters.

Chapter VI summarizes the results of the present work.

CHAPTER II

EXPERIMENTAL TECHNIQUES

An overview of laser ablated plasmas is presented in Chapter I. We studied pulsed laser ablated carbon plasma in vacuum and in the presence of air, helium and argon gases at low and moderate laser irradiances.[46,79,93,94] A Nd:YAG laser (Spectra Physics, DCR-4G) and its harmonics were used to produce carbon plasma. Spectroscopic studies of ionic, atomic and molecular species of carbon were conducted. The parameters like temperature, density and expansion velocity of the carbon plasma are estimated. In the presence of ambient gases, various interaction processes are investigated.[79] At low laser irradiance, plasma emission was found to be dominated by various C_2 molecular bands.[46,93,94] The vibrational temperature is estimated at various helium pressures using intensities of C_2 Swan bands. Some studies on characterization of laser ablated carbon powder 'soot' and laser deposited carbon films were also carried out.[95,96]

A Q Switched Nd:YAG laser and its harmonics (2ω, 3ω and 4ω) were used to produce plasma for laser ablation studies. It is capable of delivering energy upto 1 J in 2.5 and 8.0 ns (FWHM) pulse at fundamental with a repetition rate of 10 pulses per second. The laser has a guassian limited mode structure, the beam divergence being less than 0.5 mrad. The pulse width of harmonics scales as pulse width of 1.06 μm divided by $\sqrt{2}$. The energy of the laser was monitored using a laser power meter (Ophir Model 30 A) by placing the power meter in the path of the main beam. Laser energy was varied by changing the voltage on the laser oscillator and amplifier. Burn patterns taken at different energies show no significant variation in mode pattern. The pulse duration was measured with a fast photo

diode (Antel, Model As-2, rise time < 35 ps) as shown in Fig. 8. The output

from the detector was displayed on the oscilloscope (Tektronics, 11302A) which

was triggered externally with a Q-switch synchronous pulse from the YAG laser.

The output signal was digitized using digitizing camera (Tektronics DCS 01)

attached to the oscilloscope. Digitized signal was fed to a personal computer

for further data processing. Typical temporal profile of 8 ns (FWHM) laser

pulse at 1.06 μm is shown in Fig. 9(a) and that of 1.8 ns (FWHM) at 0.532 μm

corresponding to 2.5 ns (FWHM) at fundamental is shown in Fig. 9(b). In Fig.

9(b) two peaks around the main pulse are equally spaced beats. The separation

between the beats is the cavity round trip transit time. Various harmonics

were generated using Type II phase matched $KD^{*}P$ crystals. Second, third and

fourth harmonics were separated from the fundamental using the prism harmonic

separator (PHS-1). The layout of prism harmonic separator is shown in Fig. 10.

For separating the harmonics from the fundamental, the Pellin-Broca Prism

(P-1) was adjusted so that the incident beam passes through the centre of it

and directs 1.06 and 0.532 μm beams through the roof prism (P-2) into the beam

dumper. It was ensured that the 0.532 μm beam also passes through the centre

of the half wave plate. The prisms P-4 and P-3 were inserted in the paths of

1.06 and 0.532 μm to get the separated outputs from the output windows.   In

order to separate third harmonic from the fundamental (1.06 μm) and second

harmonic (0.532 μm) the prism P-1 was adjusted until the 0.355 μm beam passes

through the centre of the half wave plate and strikes the metalplug

next to the beam dumper. Output was taken by moving prism P-3 into the

path of 0.355 μm beam so that it passes through the centre of the output

window. The fourth harmonic (0.266 μm) was separated from the other three

harmonics after replacing the prisms P-1 and P-3 by quartz prisms. The quartz
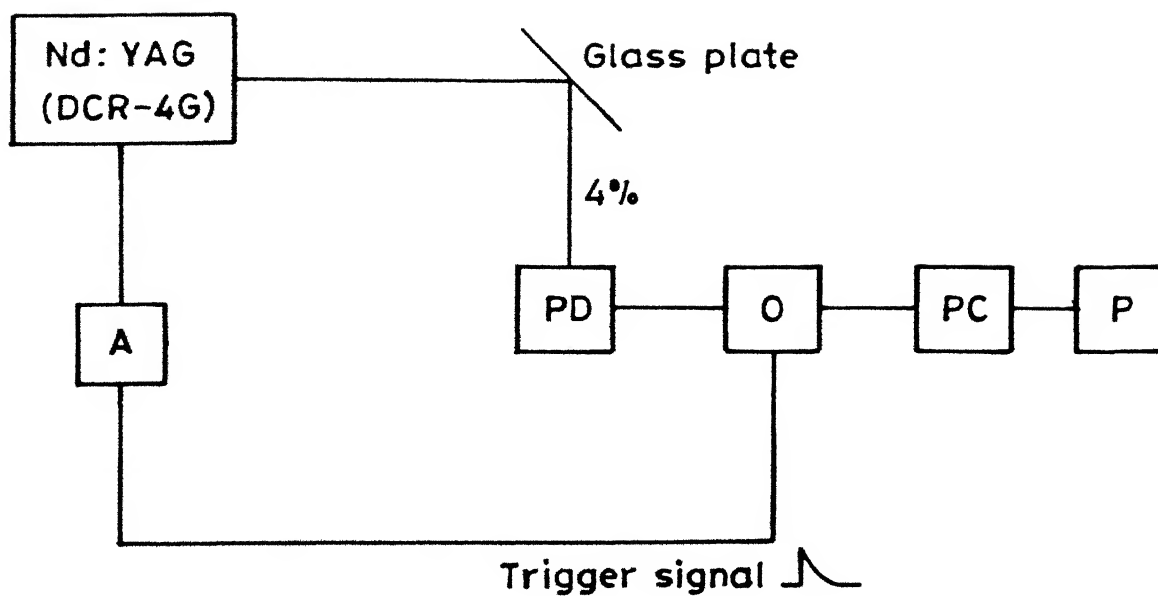
Nd:YAG-Laser; A-Attenuator; PD-Photodiode; O-Oscilloscope; PC-Personal computer; P-Printer.

Fig. 8   Experimental set up for measurement of pulse width of Nd:YAG laser and its harmonics.
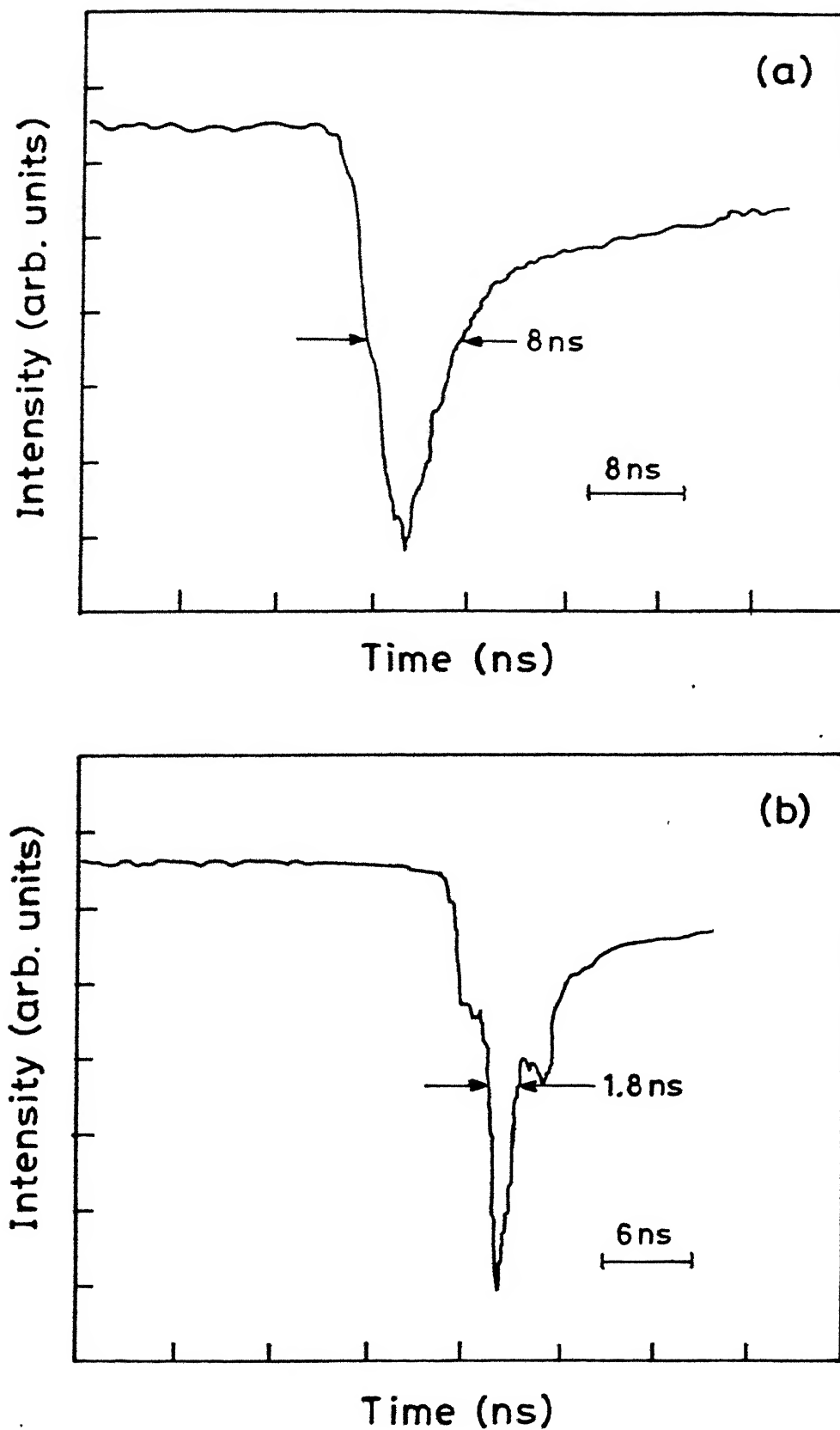
Fig. 9   Typical temporal profile of the Nd:YAG laser;

(a) 1.06 μm, 8.0 ns (FWHM).

(b) 0.532 μm, 1.8 ns (FWHM).
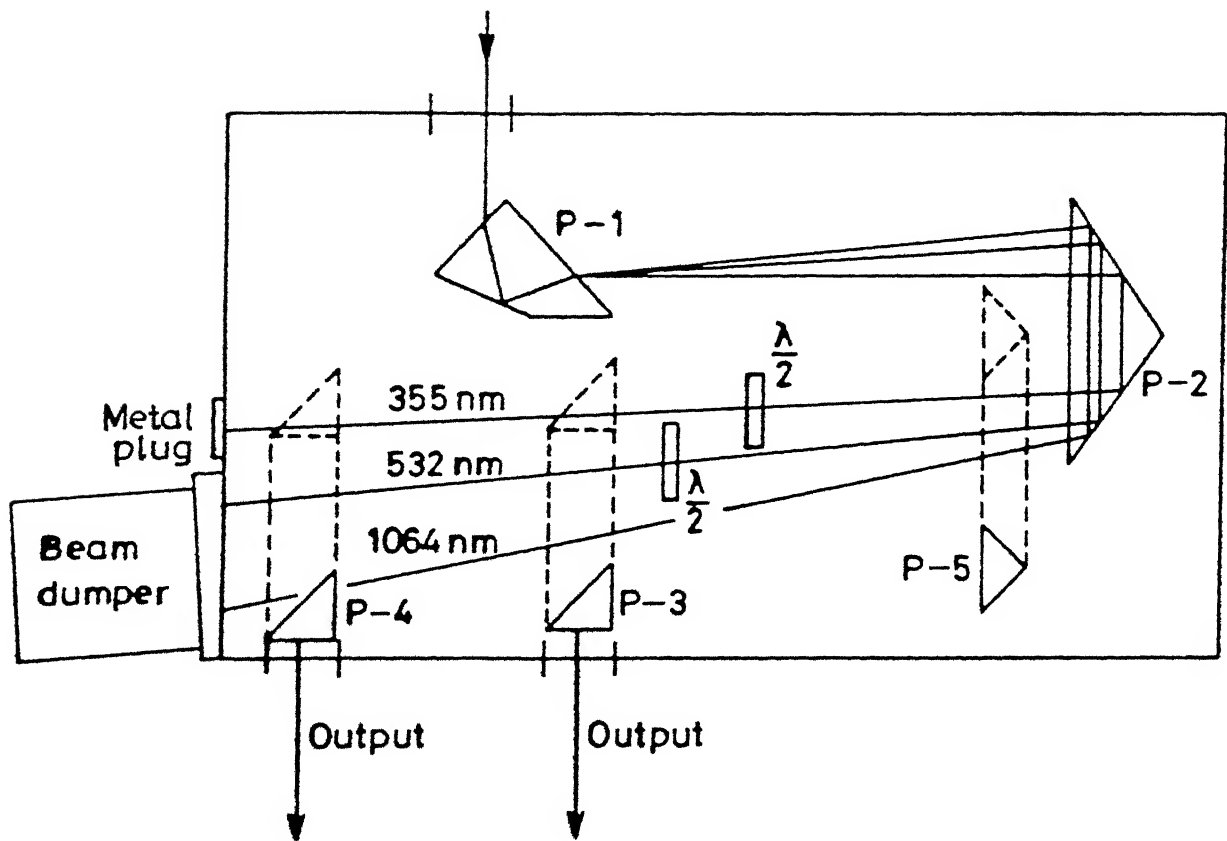
P-1, P-2, P-3, P-4 and P-5 are Prisms; λ/2 is Half-wave plate.

Fig. 10   Prism harmonic separator.

prism P-5 acts as roof prism P-2 in directing the fourth harmonic on to the output prism P-3 which was adjusted to get the beam at the centre of the output window. While looking for harmonics care was taken to direct the unused fundamental (1.06 μm) and 2nd harmonic (0.532 μm) beam into the beam dumper.

The experimental set up used for ablation studies is shown in Fig. 11. The laser beam was focussed on to the graphite target rod of 1 cm diameter attached to the target holder in a target chamber using a lens. To avoid crater formation, the target was continuously rotated and translated with the help of an external stepper motor so that each laser pulse falls on fresh graphite surface every time. The target chamber is of mild steel, chrome coated from the inside and has three output ports. One of the three output ports was used for laser input and the other two, perpendicular to the laser input port were used for recording the spectrum and for viewing the plasma. Quartz windows were pressed in vacuum on to the ports by O-rings contained in the flanges. The target chamber was evacuated to a pressure better than 10^{-3} Torr using a rotary pump and an oil diffusion pump. Experiments were carried out using helium, argon and air in the pressure range 10^{-3}- 100 Torr as background gases. A thermocouple gauge, an oil manometer and a pressure gauge (0 - 125 Torr) were used to monitor the pressure in the chamber. Gas was fed into the target chamber from the gas cylinder through a needle valve connected to the target chamber. The system was purged with the gas to be used several times before taking any data. The gauges near the target chamber were used to monitor pressure of the gas. The plasma radiation emitted from the target was imaged on to the entrance slit of monochromator (Jobin Yvon, HRS-2) with a lens of focal length of 12 cm so as to have one-to-one correspondence with the plasma and its image onto the slit of monochromator. The monochromator was
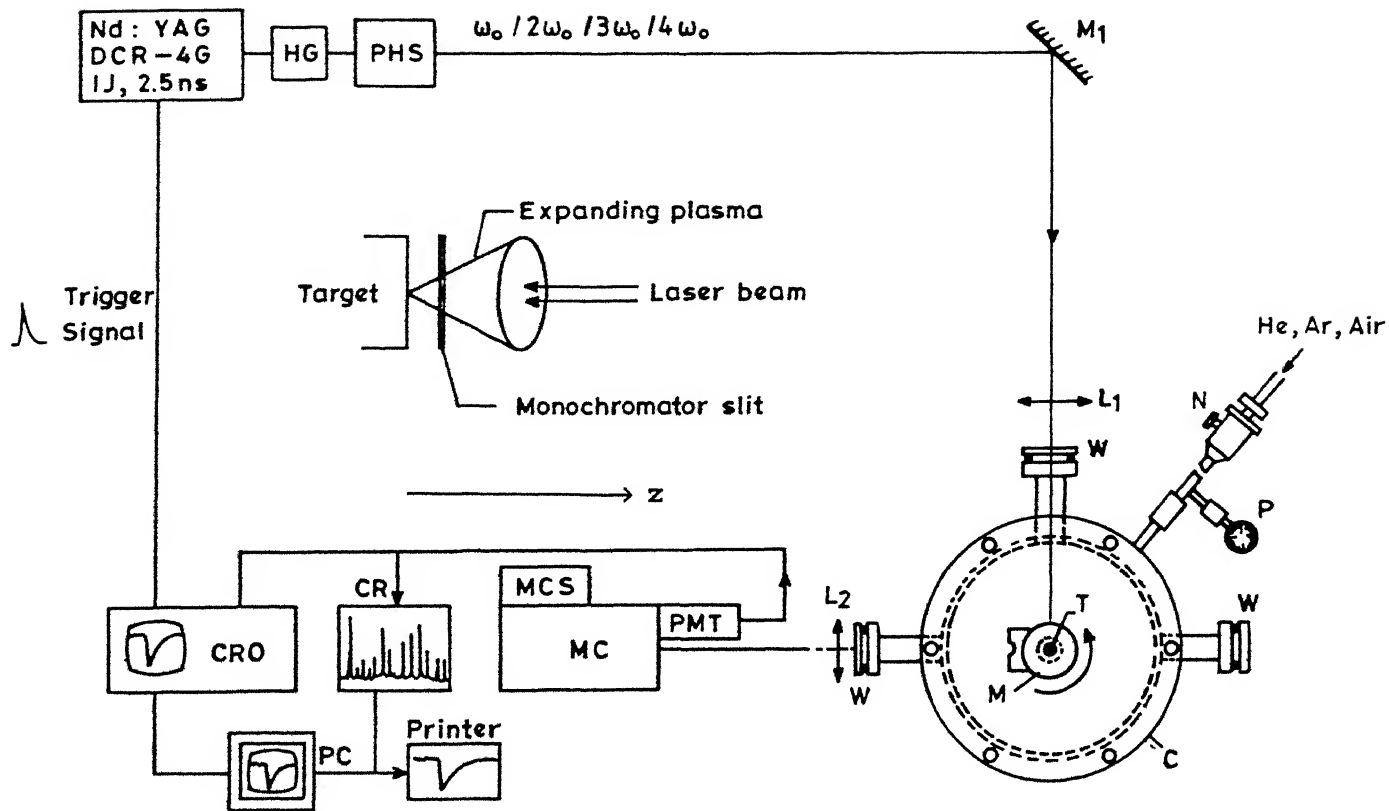
Nd:YAG-Laser; HG-Harmonic Generator; PHS-Prism Harmonic Separator; M_1-Reflecting mirror; L_1,L_2-Lenses; W-Window; M-Motor; T-Target; P-Pressure Gauge; N-Needle valve; C-Target Chamber; MC-Monochromator; PMT-Photomultiplier tube; MCS - Microprocessor controlled scan system; CR-Chart recorder; CRO-Oscilloscope; PC-Personal Computer;
[Inset shows the expanding plasma as seen by the monochromator slit]

Fig. 11   Experimental set up for spectroscopic studies of laser ablated carbon plasma.

continuously tuned using a microprocessor controlled scan system.[97] The output from the monochromator was detected with a photomultiplier tube (Hamamatsu, 1P28) and recorded on a strip chart recorder or displayed on the oscilloscope. The signals were digitized using digitizing camera and fed to a personal computer for data processing as described earlier. Experimental setup used for deposition of carbon films is shown in Fig. 12. The laser radiation was focussed using a cylindrical lens of 30 cm focal length on to the horizontal graphite rod. The carbon films were deposited on glass and silicon substrates. The substrate holder was kept parallel to the surface of target.

Diagnostics of laser ablated plasma

The techniques usually employed to measure the plasma parameters such as electron temperature, electron density and expansion velocity are listed in Table 1. We used the relative intensities of spectral lines to measure the electron temperature,[79,98] Stark broadened profile of a transition for electron density[79,99] and temporal profiles of laser ablated plasma for expansion velocity of the plasma front.[79,99] However, for low laser irradiance vibrational temperature[94] was estimated from C_2 Swan band head intensities.

Electron temperature

Relative intensities of lines from a given state of ionization can be used to calculate the electron temperature.[79,98] Assuming the plasma in local thermodynamic equilibrium the temperature of the plasma can be estimated
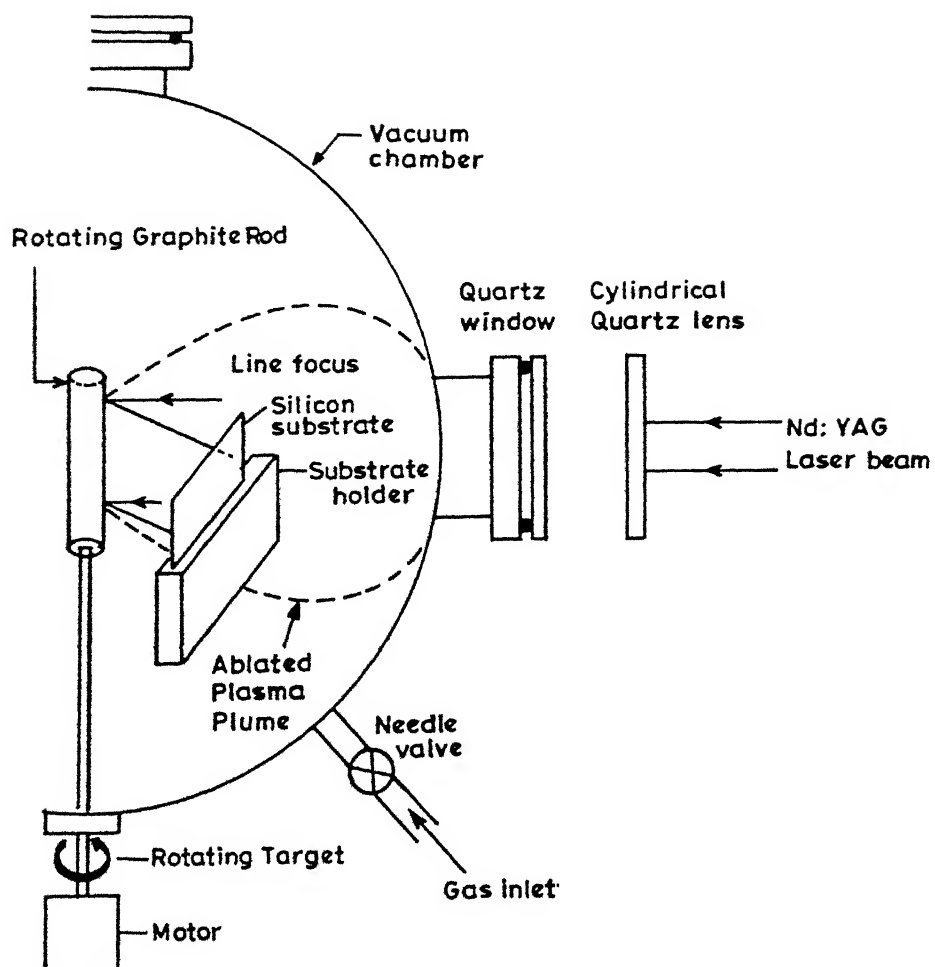
Fig. 12   Experimental set up used for deposition of carbon films.

Table 1

Experimental techniques used for plasma diagnostics

Laser irradiance	Plasma parameter	Diagnostics
Moderate 10^{10}-10^{12} W/cm^2	Electron Temperature	Line intensity measurements[79,98,100] Time of flight measurements[36,37] Doppler profile measurements[101,102] Langmuir probe measurements[103]
	Electron Density	Spectroscopic techniques (a) Stark broadening[98,101] (b) Resonance absorption[35,102] (c) Laser-induced fluorescence[57,104] Optical interferometry[105] Langmuir probes[103]
	Expansion Velocity	Temporal profiles[79,99] Time of flight measurements[36,37] Temperature measurements[102]
Low 10^8 - 10^9 W/cm^2	Vibrational Temperature	Swan band head intensities[46,94,106]

using the relation[100]

$$\ln\left(\frac{I_{ij}\,\lambda_{ij}}{A_{ij}\,g_i}\right) = \ln[\text{constant}] \; - \; \frac{E_i}{k_B T_e} \tag{38}$$

where i and j are the upper and lower state of the various transitions used, respectively; λ_{ij} is wavelength, I_{ij} is the intensity and A_{ij} is the transition probability of the corresponding transition, E_i and g_i are the excitation energy and degeneracy of the upper state, respectively, k_B is the Boltzmann constant and T_e is electron temperature. These parameters are available in the literature.[107] The slope of the curve ln $(I_{ij}\lambda_{ij}/A_{ij}g_i)$ against E_i gives the electron temperature. The estimated electron temperature[79] lies between 2-10 eV.

Electron density

The stark broadened transitions for which the stark-broadening coefficients have been measured or calculated, can provide information on electron densities. The relevant data is available in the literature.[100] Stark-broadening occurs due to perturbation of the energy levels of an atom or ion by the changing electric fields occurring in a collision with a charged particle. The line profiles were recorded keeping the monochromator resolution to maximum. Observed lines were fitted to Lorentzian profile with true half width being given by[101]

$$\Delta\lambda_{true} = \Delta\lambda_{observed} - \Delta\lambda_{instrument} \tag{39}$$

$\Delta\lambda$ of a line (FWHM) being given[101] by

$$\Delta\lambda = 2W\left(\frac{n_e}{10^{16}}\right) + 3.5A\left(\frac{n_e}{10^{16}}\right)^{1/4} \times (1-1.2N_D^{-1/3})W\left(\frac{n_e}{10^{16}}\right) \tag{40}$$

First term in Eq. (40) gives contribution from electron broadening and second term is the ion broadening correction; W is the electron impact parameter which can be interpolated at different temperatures and A is the ion broadening parameter, both W and A are weak functions of temperature, n_e is electron density and N_D is number of particles in Debye sphere given by

$$N_D = 1.72 \times 10^9 \frac{[T(eV)]^{3/2}}{[n_e(cm^{-3})]^{1/2}} \tag{41}$$

Eq. (40) is valid only if $N_D \geq 1$ and $0.05 < A(n_e/10^{16})^{1/4} < 0.5$. Using our measured temperature of 3 eV and density $\sim 1.2 \times 10^{17}$ /cm^3, we get the number of electrons in the debye sphere equal to 25 and the parameter $A(n_e/10^{16})^{1/4}$ equal to 0.07. Thus using Eq. (40) for density measurement is justified. Since ion broadening correction for laser ablated carbon plasma is much smaller than the electronic contribution, Eq. (40) further simplifies to

$$\Delta\lambda = 2W\left(\frac{N_e}{10^{16}}\right) \quad (\text{Å}) \tag{42}$$

We have used Eq. (42) for calculation of electron density for C II transition $3p\ ^2P^0 - 4s\ ^2S$ at 392.0 nm. Electron density[79] using 1.06 μm laser radiation is found to be $10^{16}-10^{17}$ /cm^3 .

Plasma expansion velocity

Temporal profiles of various transitions were recorded at different distances from the target for estimating the expansion velocity of ablated plasma. The slope of the curve for the variation of delay in the peak intensities with distance from the target gives the velocity of the plasma

front. The expansion velocities of C II, C III and C IV species are found to be about 4 x 10^6, 7 x 10^6 and 10 x 10^6 cm/s, respectively.[79]

Vibrational Temperature

The C_2 Swan band head intensities were used to estimate the vibrational temperature. The band spectrum being rotationally unresolved, we have used band head intensities[106] for estimating the vibrational temperature of C_2 bands. The relative population in each vibrational level $N_{v'}$ can be found using theoretical Franck-Condon factor[47] $F_{v'v''}$, and the band head intensity $I_{em}^{v'v''}$ observed at frequency ν,

$$N_{v'} = \frac{C\, I_{em}^{v'v''}}{D_\nu\, F_{v'v''}\, \nu^4} \tag{43}$$

where C is a constant and D_ν represents the correction factor for the detection system, v' and v'' are the vibrational levels of the upper and lower electronic states, respectively. Since in thermal equilibrium the population $N_{v'}$ of the initial state is proportional to exp $\left[-G(v')hc\, /\, k_B T_{vib} \right]$, we have

$$\frac{N_{v'}}{N_{v'=o}} = \exp\left[\frac{-[G(v')-G(v'=o)]hc}{k_B T_{vib}} \right] \tag{44}$$

where G(v') is term value of the upper vibrational level v', k_B is the Boltzmann constant and T_{vib} is the molecular vibrational temperature. We have used the Frank-Condon factor from Spindler.[47] Slope of the curve between the relative population of the upper vibrational level as derived from the measured intensities and vibrational quantum number gives vibrational temperature. The vibrational temperature from C_2 Swan band head intensities

was calculated at various helium pressures and laser wavelengths. The estimated vibrational temperature[94] lies between 6000 and 12000 K.

Characterization of laser ablated carbon soot and deposited film

Table 2 lists the various experimental techniques used to characterize and study the carbon clusters mainly fullerenes from laser ablated soot and deposited film. We have used X-ray diffraction and Scanning electron microscopy to characterize the pulsed laser deposited carbon film on silicon and glass substrates. UV-visible and Infrared spectroscopy were used to characterize fullerenes from laser ablated carbon soot.[95,96]

X-Ray Diffraction

The structural properties of the deposited carbon films were investigated by X-ray diffraction using an X-ray Diffractometer (Rich & Seifert, JSO-debyeflex 2002) in order to determine crystalline orientation. Diffraction leads to maxima in the intensity of the scattered X-rays and the position of the maxima gives information about the size and shape of the unit cell whilst the width of the maxima can be used to evaluate the size, orientation and strain of grains in polycrystalline materials.[108] Peaks observed at $10.3°$, $11°$, $17.9°$ and $21°$ show the presence of (100), (002), (110) and (112) crystalline planes of C_{60}, respectively.[96]

Scanning Electron Microscopy

Scanning electron microscopy (SEM) is usually used to study the variation in the surface structure and to examine the topography of the deposited carbon films. We used Scanning Electron Microscope (JEOL, JSM 840A) to study the surface morphology of the film. SEM photographs show that in

Table 2

Techniques used for characterization of carbon soot

and deposited carbon films.

Mass Spectrometry[71,109]

X-Ray Diffraction method[71,73,109]

Nuclear Magnetic Resonance (NMR)[71,73,109]

UV-Visible Absorption Spectroscopy[71,73,109]

Infrared Spectroscopy[71,109]

High Performance Liquid Chromatography (HPLC)[71]

Raman Spectroscopy[71,109]

Scanning Electron Microscopy[71,110]

Transmission Electron Microscopy[71]

vacuum the assemblage of hexagonal crystals is dominated whereas in the presence of helium gas spherical aggregates of carbon similar to the structure of C_{60} and C_{70} dominate.[96]

UV- visible and Infrared spectroscopy

We used a UV-visible spectrometer (Shimadzu, UV 160) for recording optical absorption spectrum of the n-hexane / benzene dissolved carbon soot. The peaks in the optical absorption spectrum in the range 200-450 nm show the presence of fullerenes in our collected soot.[95,96]

Infrared spectrometers (Perkin-Elmer, 1320 and 1600 Series FTIR) were used for recording IR spectrum of the benzene dissolvable carbon soot deposited on KBr pellets. The prominent modes in the IR spectrum show the presence of C_{60} and C_{70} clusters.[95,96]

LASER ABLATED CARBON PLASMA AT MODERATE INTENSITIES

INTRODUCTION

The focussed high-intensity laser radiation onto a solid target in vacuum or ambient gas creates a hot dense recombining plasma.[111,112] The interaction of an expanding plasma with an ambient background has been the subject of numerous experimental[112,113,114] and theoretical[115] investigations where it is shown that both plasma effects and atomic and molecular phenomena play many important roles in the formation of transient plasma. The studies are aimed at modelling of various processes in space physics,[40] plasma chemistry[12] and hydrodynamics of the expanding plasma.[21,22] Laser ablated plasmas in metals in the presence of background gas have been used in the recombination phase for generation of laser oscillations[116,117] and as strong x-ray and vacuum ultraviolet sources.[118,119] Detailed studies on the temporal, spatial and spectral characteristics of laser produced carbon plasma have been reported by Lee et al.[120] Laser ablated carbon plasma in an ambient gas has been used for deposition of C_{60} on various substrates.[74] Anan'in et al[42,121] have investigated the interaction of a laser plasma with the background gas in the pressure range 10^{-3}- 1 Torr of air using spectroscopic and high speed photographic methods. Enhancement of line emission from a laser produced plasma in a background gas has also been reported.[38,39,122]

Here we report spectroscopic studies of laser ablated carbon plasma in vacuum as well as in the presence of ambient gases.[79] The role of recombination and charge exchange processes in enhancing the line emission of various ionic species of carbon in the presence of ambient gas is discussed. The appearance of a peculiar double peak structure in the temporal profile of

the C II transition 3d ^{2}D-4f ^{2}F^0 at 426.7 nm in a laser produced carbon plasma as it expands into a background medium is reported for the first time.[79] These studies are helpful in the diagnostics of the plasma gas interaction regime,[42,121] in laser microspectral analysis[11] and in the development of X-ray[18,23] and UV lasers.[19]

EXPERIMENTAL SET UP

Experimental set up used in the present study is similar to the one shown in Fig. 11. A Nd:YAG laser with gaussian limited mode structure (1.06 μm) delivering upto 1 J of energy in 2.5 ns (FWHM) with a repetition rate of 10 pps was used to produce the carbon plasma. A 50 cm focal length lens focussed the laser beam onto the rotating graphite target to a spot of 240 μm diameter. Experiments were carried out for various background gases namely, air, argon and helium, at different pressures in the range 10^{-3}-100 Torr. The data acquisition system used is already described in Chapter II.

RESULTS AND DISCUSSION

The emission spectra of carbon plasma in the wavelength range 190-800 nm in vacuum as well as in the presence of helium and argon gases were recorded at different distances (z) away and parallel to the target surface by moving the monochromator on precision translators in the horizontal plane in the direction perpendicular to the direction of the expanding plume. The inset in Fig. 11 shows the z variation. It was made sure that the background gas does not breakdown and absorb the laser radiation.[123] Spectra were recorded at various laser intensities and laser wavelengths. It was found that at moderate laser intensities ~ 10^9-10^{12} W/cm^2 atomic and ionic species dominate the plasma emission. Figure 13 shows a typical emission spectrum in
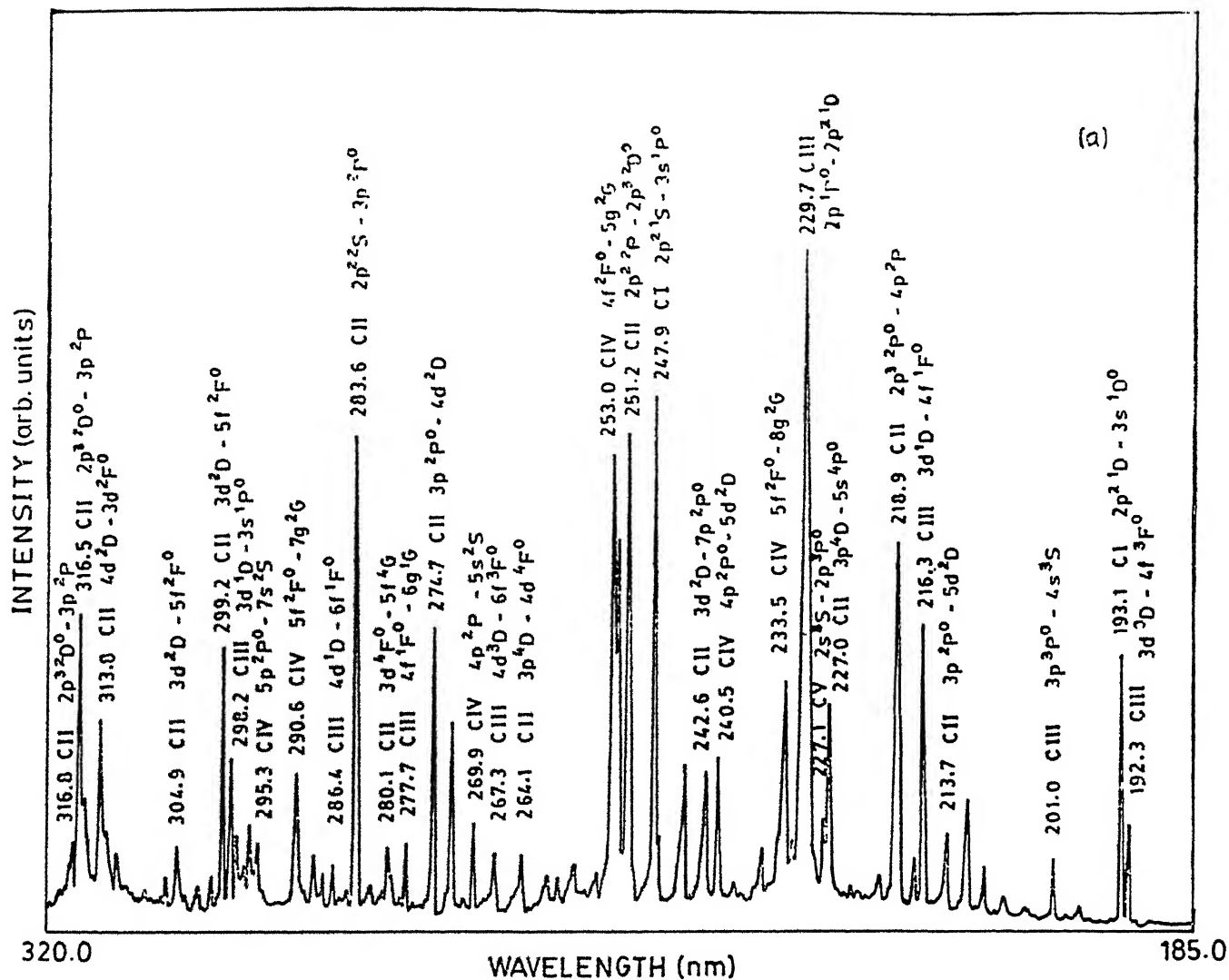
.g. 13 Typical emission spectrum in the wavelength range 190-800 nm in vacuum at 8×10^{11} W/cm^2 using 1.06 μm laser irradiation; (a) Spectrum range 190-320 nm.

INTENSITY (arb. units)

(b)

444.3 CIII 4d^{1}D - 3d^{1}P^0

438.3 CIII 4d^{3}D - 5p^{3}P^0

435.9 CIII 4f^{3}G - 5g^{3}H^0

432.5 CIII 3s^{1}P^0 3p^{1}D

428.5 CII 3d^{2}D^0- 4f^{2}D

426.7 CII 3d^{2}D - 4f^{2}F^0

422.8 CI 3s^{1}P^0-5p^{1}S

418.7 CIII 4f^{1}F^0-5g^{1}G

415.6 CIII 3p^{3}D - 5f^{3}F^0

407.0 CIII 4f^{3}F^0-5g^{3}G

405.6 CIII 4d^{1}D - 5f^{1}F^0

399.7 CI 2p^3 ^{3}D -8f F (2½)

397.3 CII 3d^{4}D^0 - 4f^{4}D

393.4 CIV 5s^{2}S - 6p^{2}P^0

392.0 CII 3p^{2}P^0-4s^{2}S

388.9 CIII 4d^{3}D - 5f^{3}F^0

387.1 CII 3d^{4}F -4f^{2}G

380.4 CI 3s^{1}P^0 - 7p^{1}D

376.2 CI
375.7 CI] 3s^{3}P^0 - 6p^{3}D

370.3 CIII 3p^{1}P - 3d^{1}P^0

360.9 CIII 4p^{3}P^0 - 5d^{3}D

358.9 CII 3p^{4}D - 4s^{4}P^0

336.1 CII 3d^{2}D - 5p^{2}P^0

450.0   WAVELENGTH (nm)   320.0

Fig. 13   Typical emission spectrum in the wavelength range 190-800 nm in vacuum at 8 x 10^{11} W/cm^2 using 1.06 μm laser irradiation; (b) Spectrum range 320-450 nm.
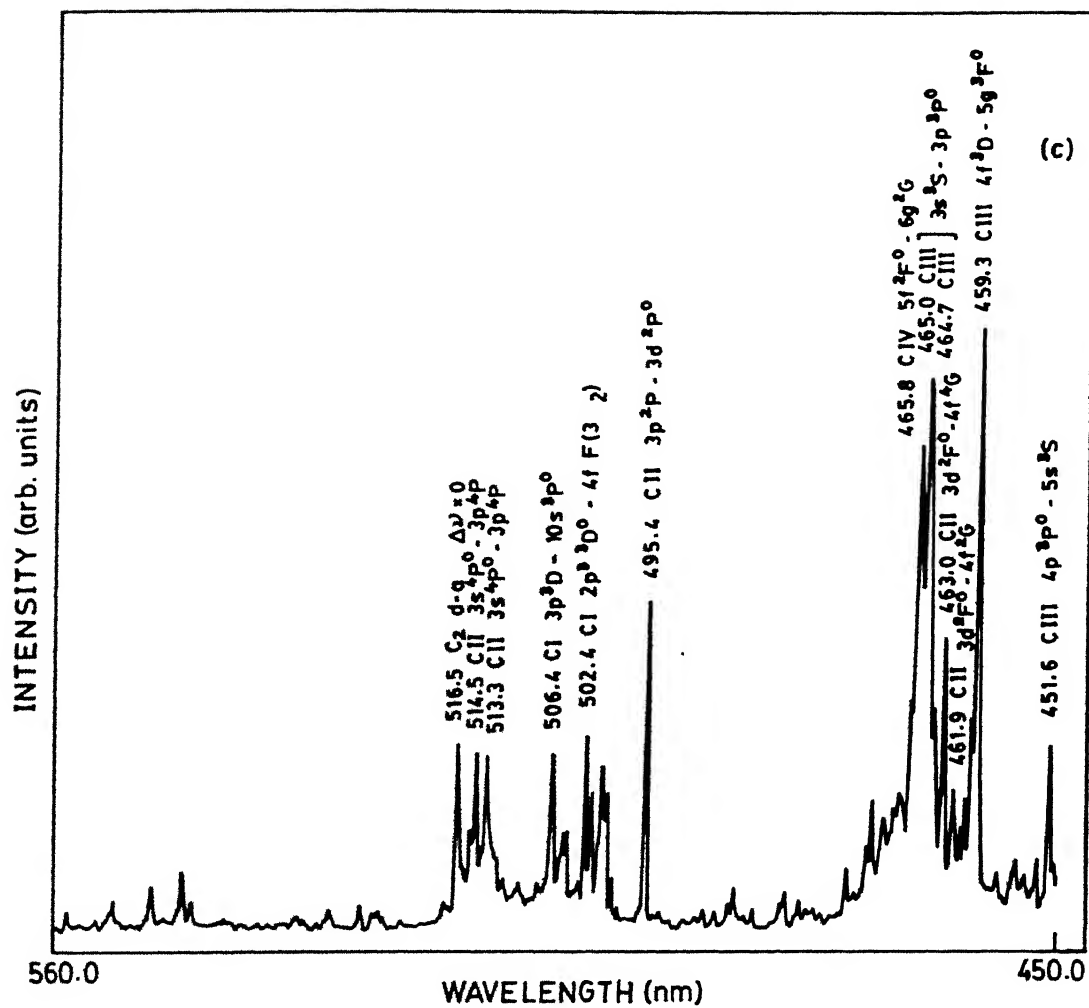
Fig. 13   Typical emission spectrum in the wavelength range 190-800 nm
           in vacuum at 8×10^{11} W/cm^2 using 1.06 μm laser irradiation;
           (c) Spectrum range 450-560 nm.
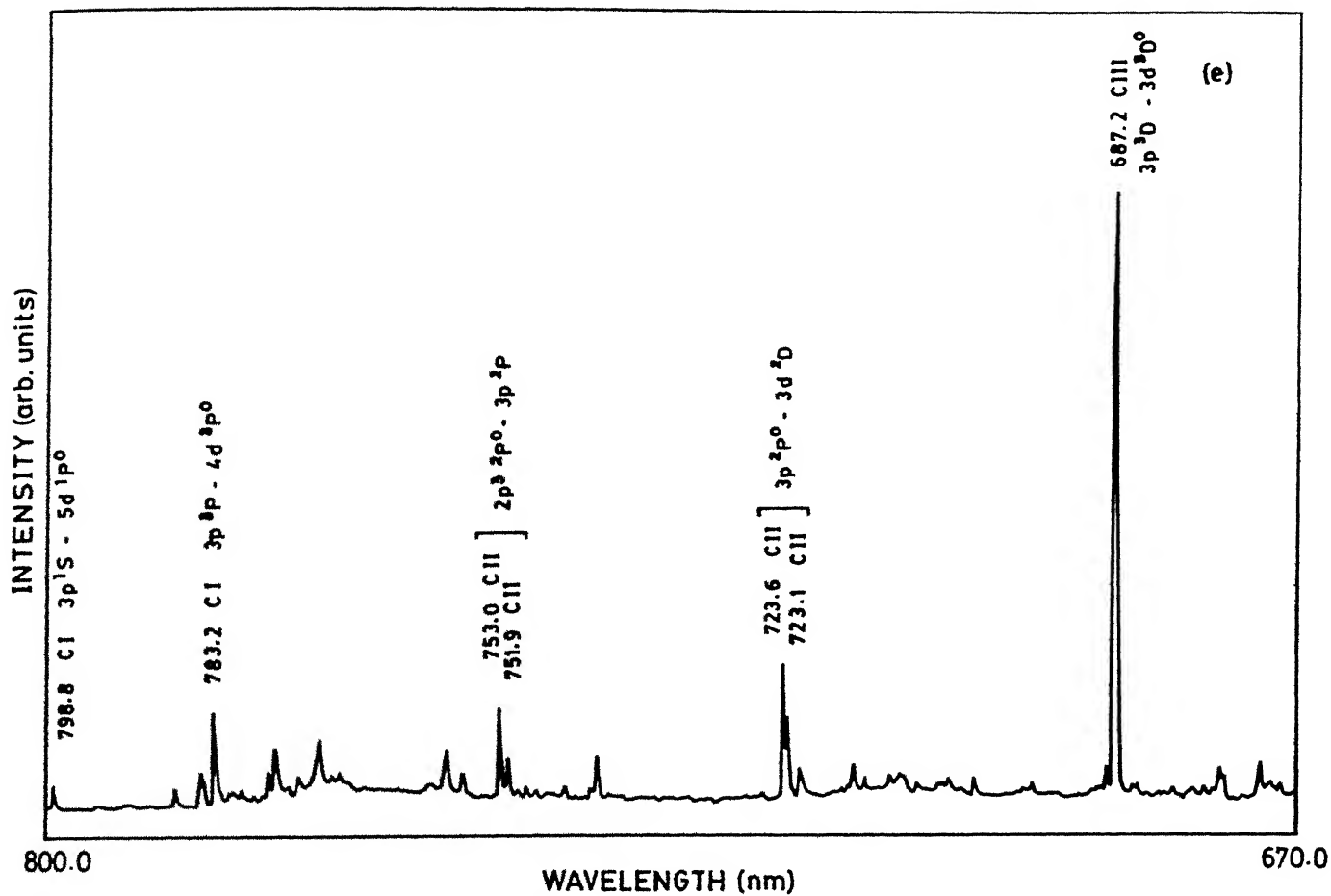
Fig. 13   Typical emission spectrum in the wavelength range 190–800 nm
in vacuum at 8×10^{11} W/cm^2 using 1.06 μm laser irradiation;
(e) Spectrum range 670–800 nm.
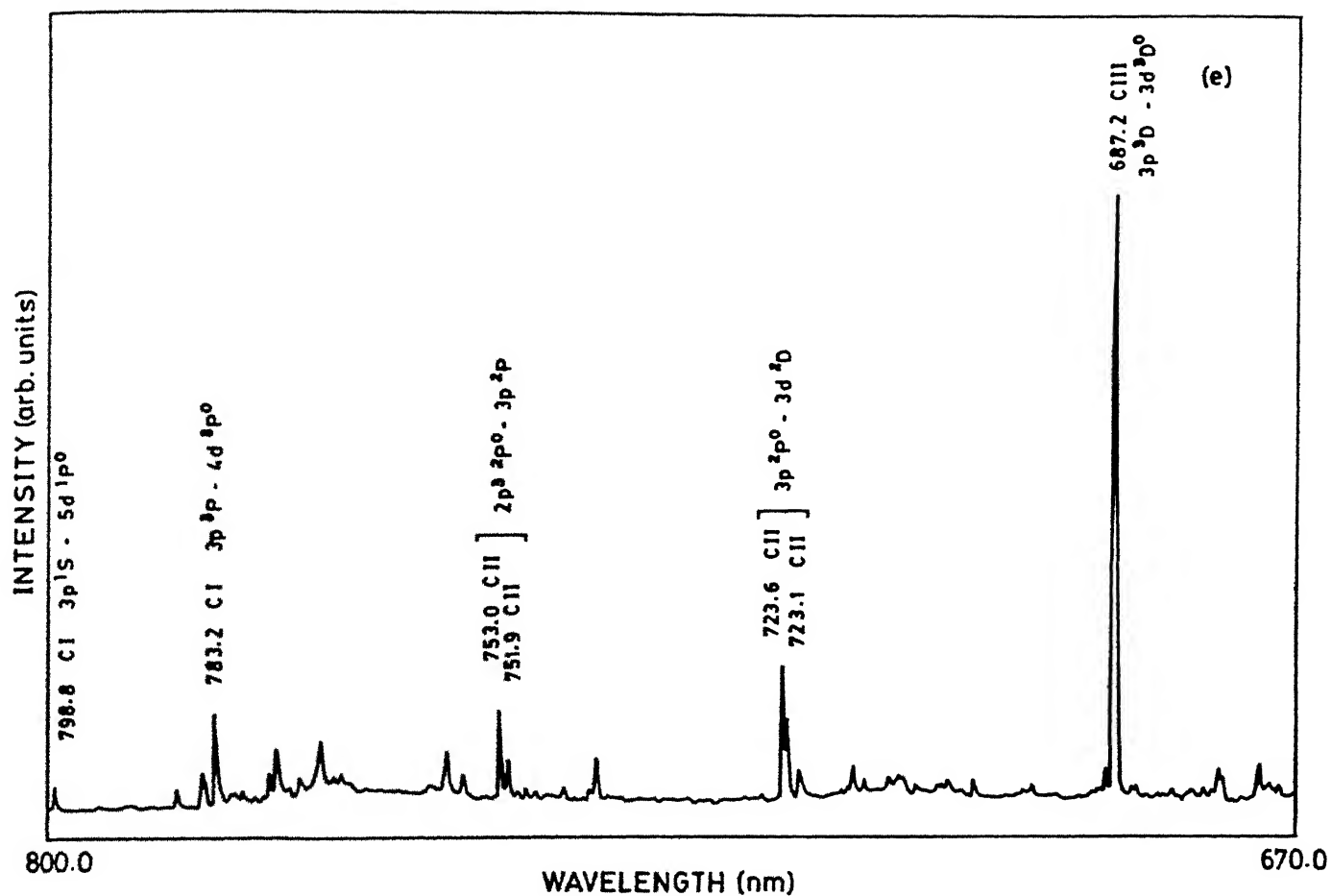
Fig. 13   Typical emission spectrum in the wavelength range 190-800 nm in vacuum at 8×10^{11} W/cm^2 using 1.06 μm laser irradiation; (e) Spectrum range 670-800 nm.

the wavelength range 190-800 nm in vacuum at laser intensity 8×10^{11} W/cm^2 and at a distance of 2 mm away and parallel to the target surface using 1.06 μm laser irradiation. The spectra were dominated by continuum radiation close to the target. The emission lines were identified using the information available in the literature.[107] We observed the transitions upto C V.

Emission spectra were recorded at various distances (z) away and parallel to the target surface. Every point in the figure to follow is an average of five observations. Figure 14 shows the normalized emission intensity for transitions $2p^2$ ^1D - $3s$ $^1D^0$ at 193.1 nm of C I, $3p$ $^2P^0$ - $5d$ ^2D at 213.7 nm of C II and $3d$ ^3D - $4f$ $^3F^0$ at 192.3 nm of C III species as a function of distance from the target for 1.06 μm laser irradiation in vacuum. It is observed that for C III species the line intensity peaks at 3 mm from the target surface and decreases rapidly as z increases whereas for C II and C I species the intensity is maximum at z = 4 mm from the target and decreases slowly as z increases. That is to say that the intensity of higher species decreases rapidly as they recombine to give lower species.

Temporal profiles were recorded of the transitions $3d$ ^2D- $4f$ $^2F^0$ at 426.7 nm of C II, $3s$ ^3S- $3p$ $^3P^0$ at 465.0 nm of C III and $3s$ ^2S- $3p$ $^2P^0$ at 580.1 nm of C IV at different distances away and parallel to the target surface in vacuum and ambient gases to estimate the velocities of different species. For each reading average of fifty profiles was taken by using the averaging system. Figure 15 shows the variation of delay in the peak intensity with distance from the target surface for 1.06 μm laser irradiation in vacuum, (pressure better than 10^{-3} Torr) the slope of the curve gives the velocity of the plasma front. The expansion velocities of C II, C III and C IV species are found to be about 4×10^6, 7×10^6 and 10×10^6 cm/s, respectively. Thus the
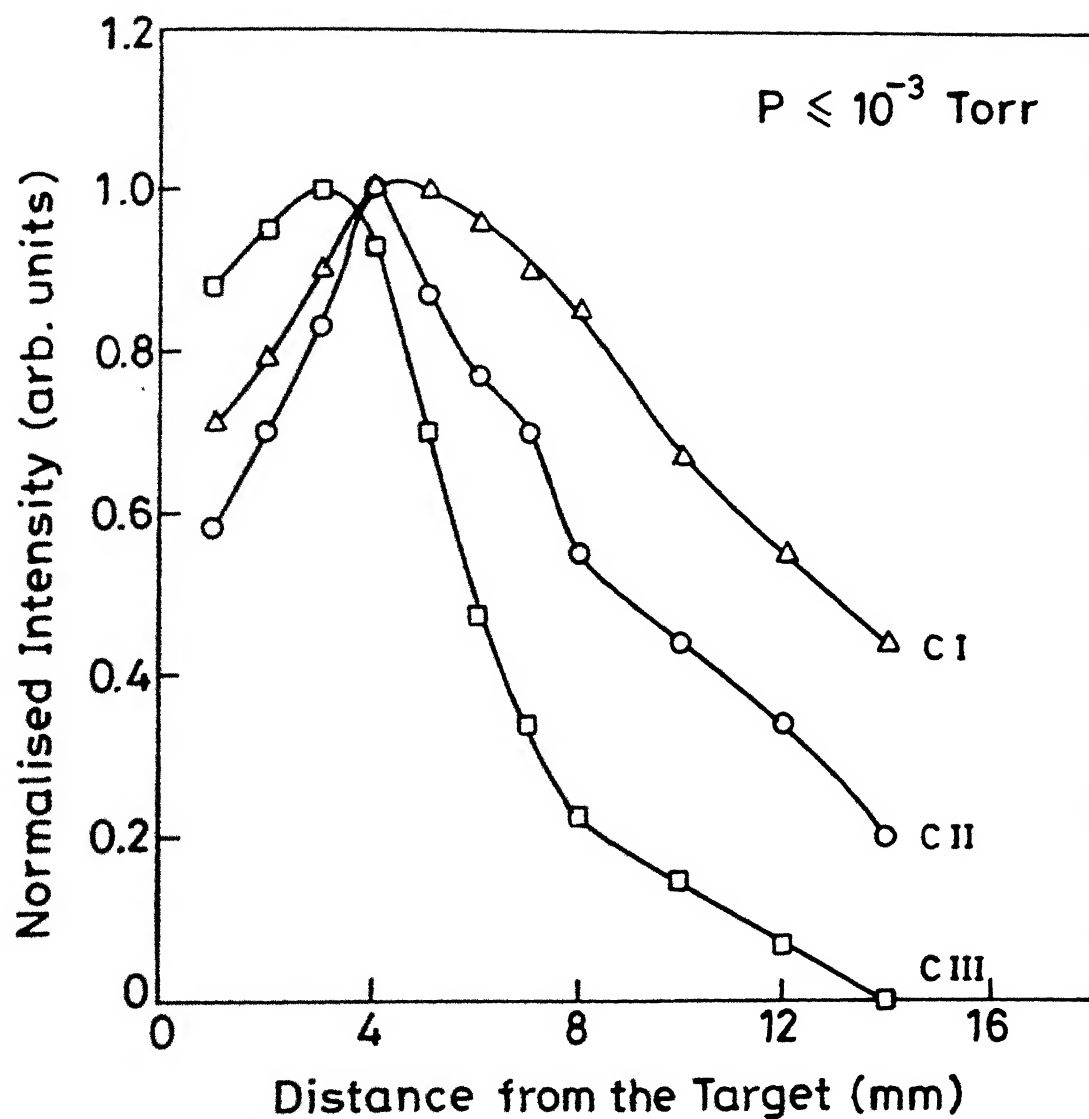
Fig. 14   Normalized emission intensity as a function of distance from
the target for transitions $2p^2 \, ^1D - 3s \, ^1D^0$ at 193.1 nm of
C I, $3p \, ^2P^0 - 5d \, ^2D$ at 213.7 nm of C II and $3d \, ^3D - 4f \, ^3F^0$
at 192.3 nm of C III species in vacuum.
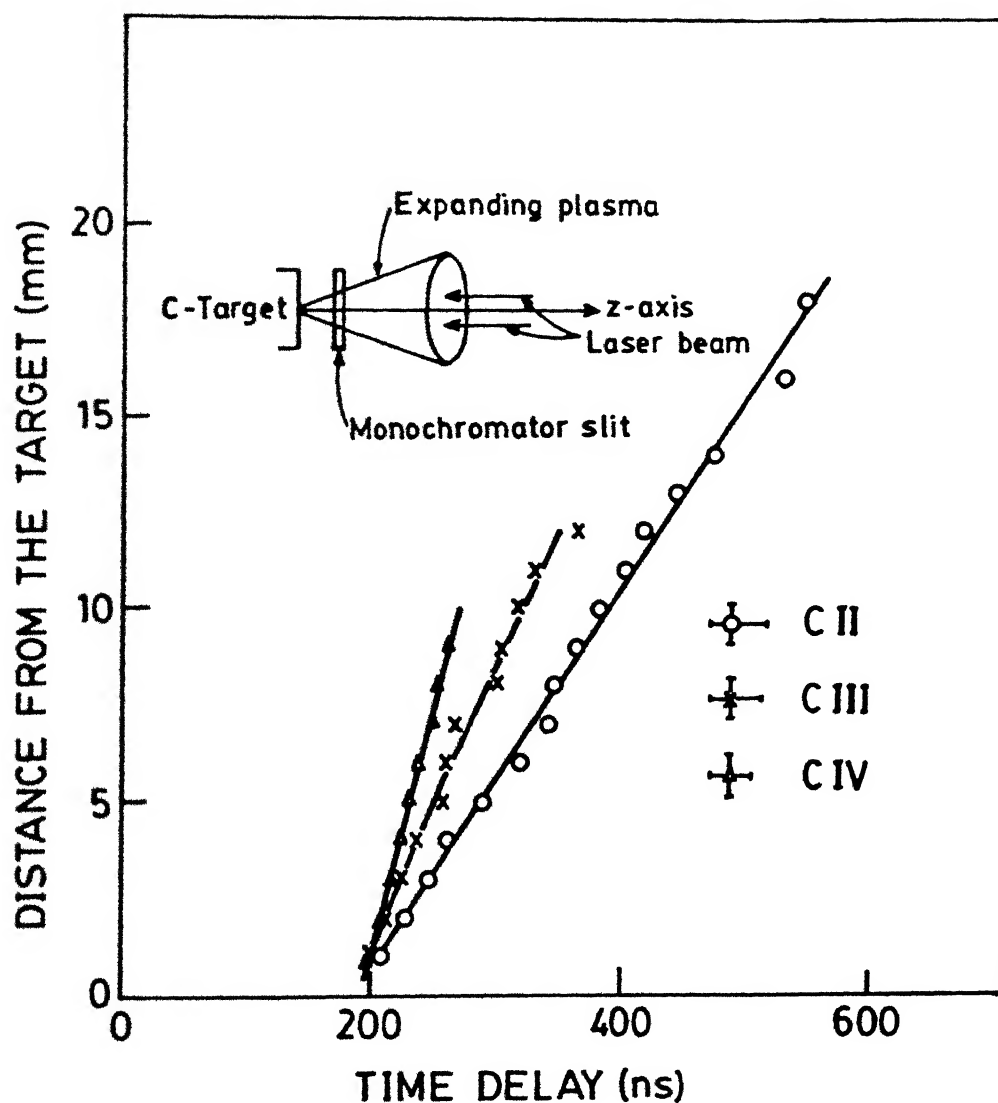
Fig. 15 Variation of time delay in the peak intensity with distance from the target for 1.06 μm irradiation at 8×10^{11} W/cm^2 in vacuum

(a) C II transition (3d ^{2}D - 4f ^{2}F^0) at 426.7 nm.

(b) C III transition (3s ^{3}S - 3p ^{3}P^0) at 465.0 nm.

(c) C IV transition (3s ^{2}S - 3p ^{2}P^0) at 580.1 nm.

expansion velocity decreases with decrease in ionic charge from C IV to C II. Figure 16 shows the variation of delay in the peak intensity with distance from the target for C II transition 3d ^2D - 4f $^2F^0$ at 426.7 nm using 1.06 μm irradiation in the presence of helium, argon and air at 10^{-3} Torr. The expansion velocities in presence of helium, argon and air are found to be about 8.2×10^6, 7.3×10^6 and 7.5×10^6 cm/s, respectively. Expansion velocity was maximum for helium and approximately same for argon and air. Thus expansion velocity of the plasma front decreases with the increase in atomic mass of the ambient gas. The temporal profiles of C III transition 3d ^1D - 4f $^1F^0$ at 216.3 nm were recorded at different distances and at various argon pressures. Figure 17 shows the variation of time delay in the peak emission intensity at various distances and for various argon pressures for 1.06 μm laser irradiation. The velocity of plasma emission front decreases with the increase in gas pressure.

Electron temperature was calculated using Eq. (38). Figure 18 shows a typical plot of E_i against $\ln\left(\dfrac{I_{ij} \, \lambda_{ij}}{A_{ij} \, g_i}\right)$ for $I = 8 \times 10^{11}$ W/cm^2 and at 2 mm distance from the target surface for 1.06 μm laser irradiation. The slope of the curve gives electron temperatures of $\approx$ 4, 6, and 7 eV for C II, C III and C IV species, respectively; electron temperature increases with higher ionic charge. Figure 19 shows temperature of C II and C III species at various distances away from the target surface. Electron temperature decreases at increasing distances from the target and decreases faster for C III species in comparison to C II species with distance. Figure 20 shows dependence of electron temperature on laser intensity for C III and C II species. We observe that temperature varies for C II, C III and C IV species as $I^{0.4}$ consistent
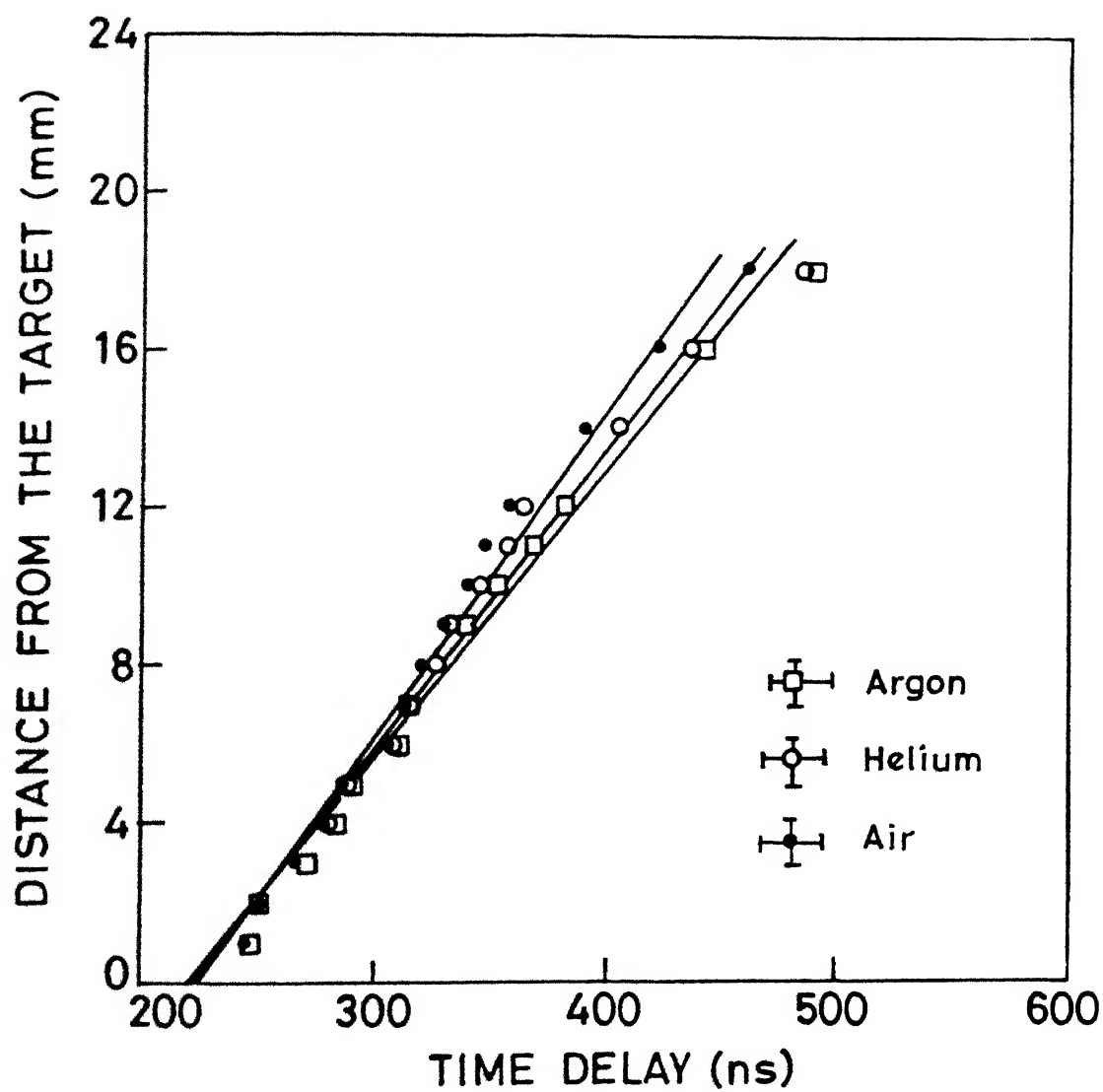
Fig. 16 Time delay in the peak emission intensity at various distances from the target for argon [open squares], helium [open circles] and air [filled circles].
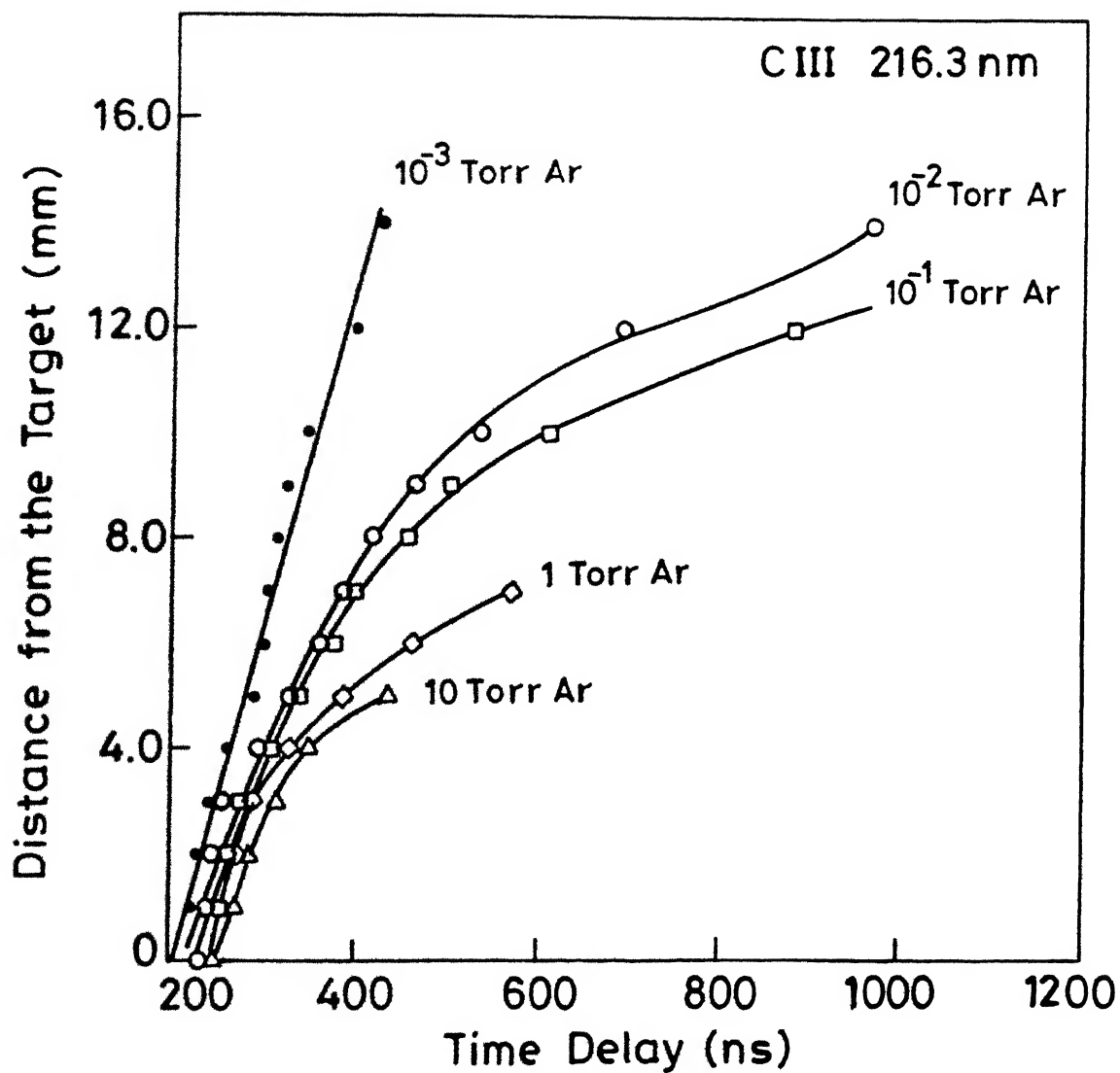
Fig. 17   Variation of time delay in the peak emission intensity with distance from the target for various argon pressures.
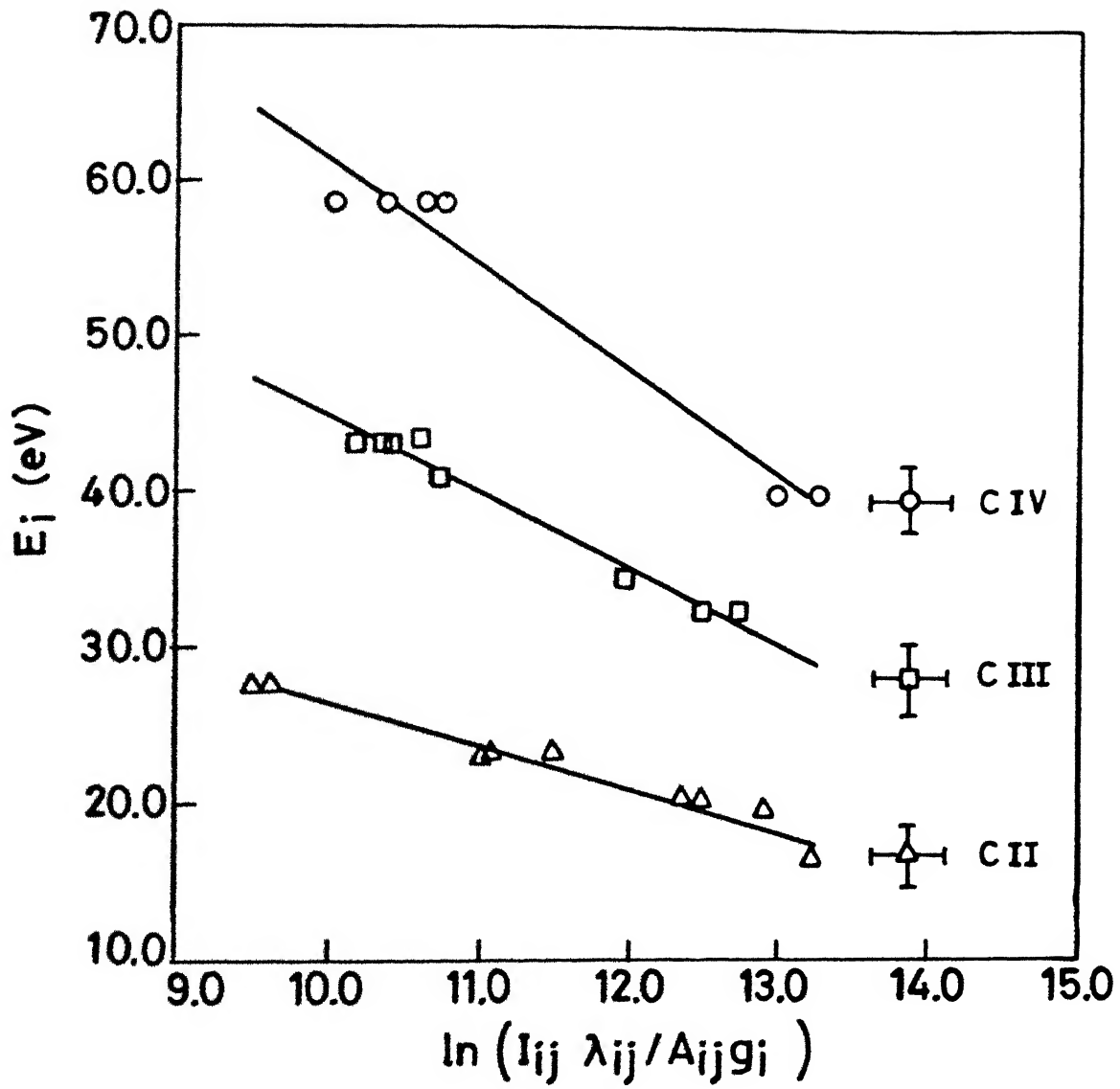
Fig. 18 E_i versus $\ln\left(\dfrac{I_{ij}\,\lambda_{ij}}{A_{ij}\,g_i}\right)$ at laser intensity 8×10^{11} W/cm^2 and at

2 mm distance from the target surface for C II, C III and

C IV transitions.
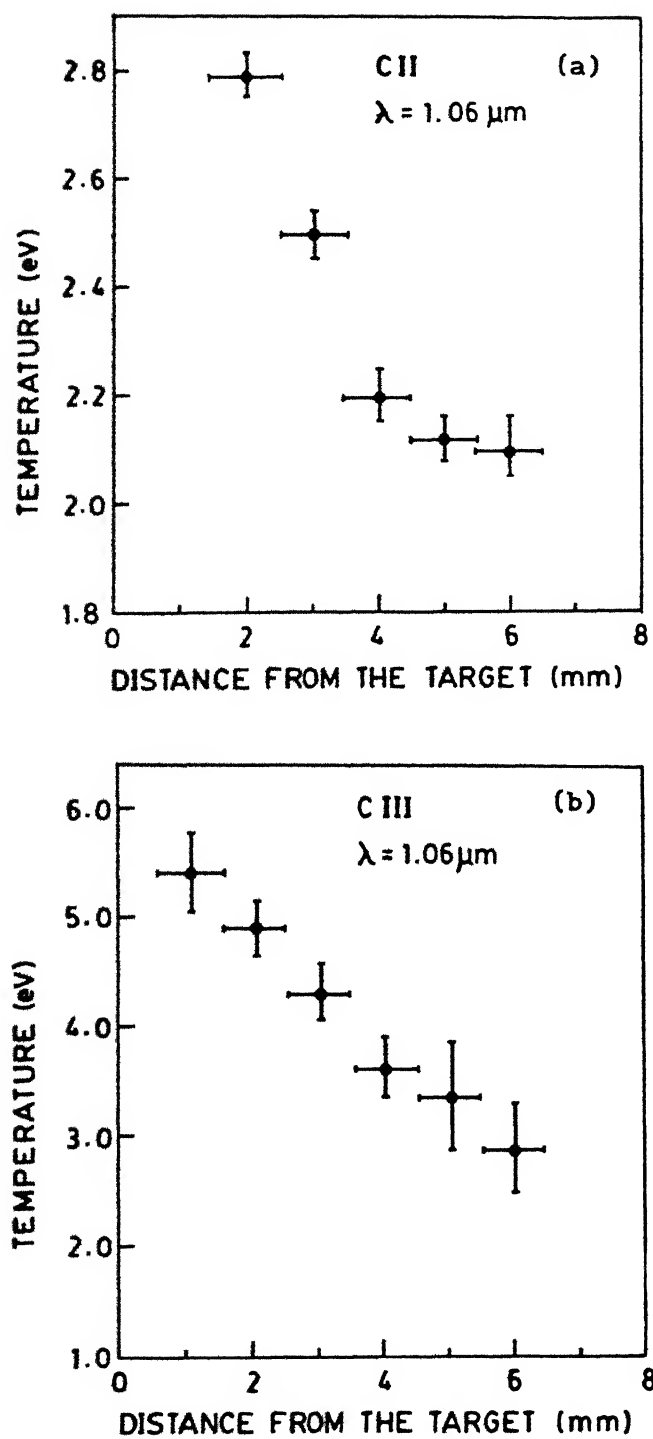
Fig. 19   Variation of electron temperature for (a) C II and (b) C III
species with distance from the target in vacuum.
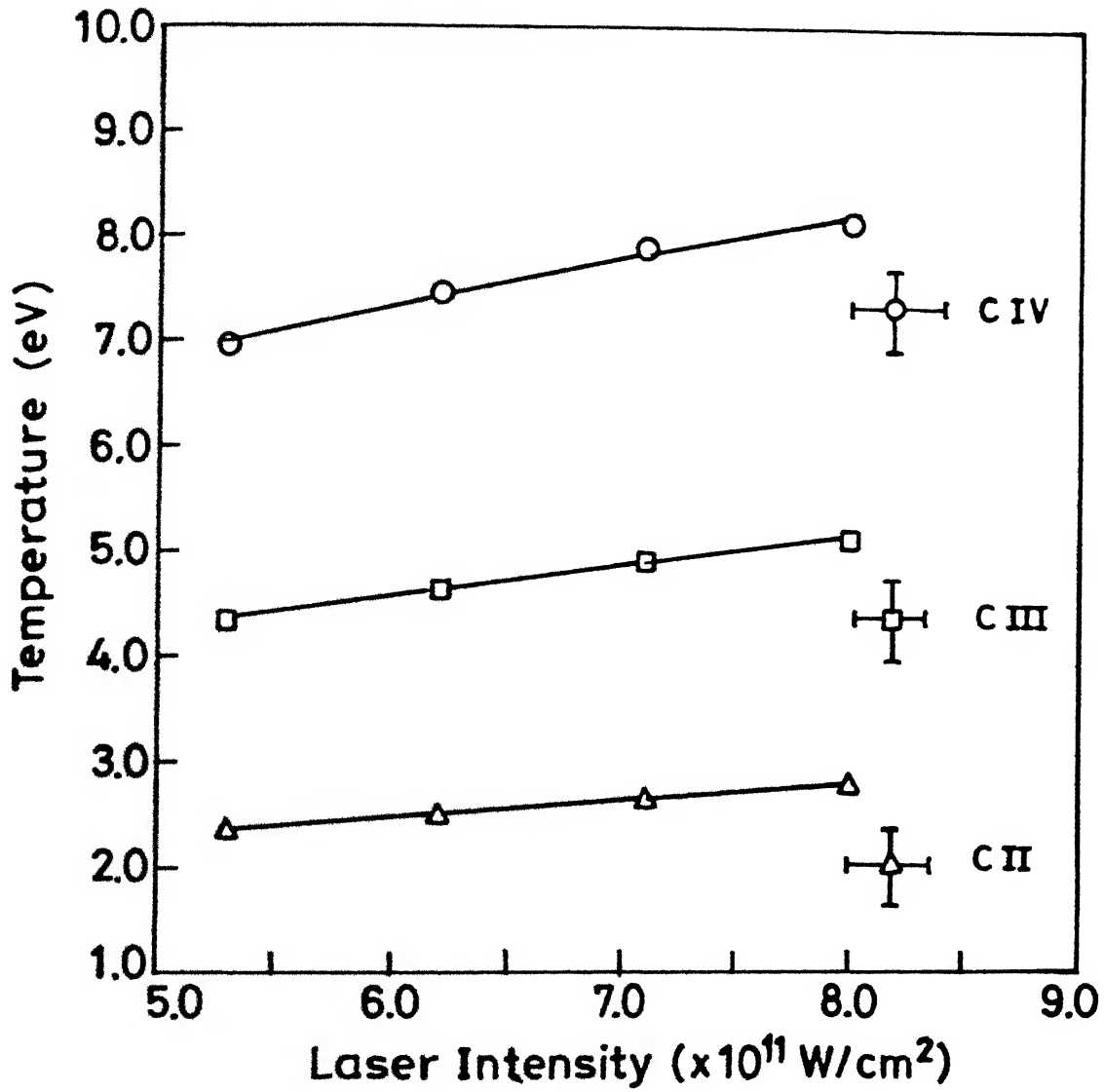
Fig. 20   Electron   temperature as a function   of   laser intensity for
C II, C III and C IV species

with $I^{4/9}$ dependence predicted from theory.[124]

Stark broadened profile of C II transition 3p $^2P^0$ - 4s ^2S at 392.0 nm was used to estimate the electron density. A typical stark broadened profile at a distance of 8 mm away and parallel to the target surface when pressure of the chamber was better than 10^{-3} Torr using 1.06 μm laser irradiation is shown in Fig. 21. Electron density measured using the relation, Eq. (42) is 10^{16}-10^{17} cm^{-3}. In order to estimate densities at various pressures, the variation of stark broadened profile with pressure of the background gas (helium and argon), was carried out. Figure 22 shows an axial density profile for C II species in the presence of helium and argon gases at 0.1 Torr for 1.06 μm laser irradiation.

For measuring electron temperature, we assumed plasma to be in local thermodynamic equilibrium (LTE). For LTE to hold the electron density must satisfy Eq. (5). Using ΔE = 2.66 eV, corresponding to the largest energy gap of the transitions used for temperature measurements and highest T_e (= 8 eV), the lower limit for n_e from Eq. (5) is 9.17×10^{15} /cm^3. Our observed values of n_e being always greater than this limit justifies the use of LTE approximation for our analysis.

Laser ablated carbon plasma studies in the presence of helium and argon gases using 1.06 μm laser irradiation indicated the line emission enhancement of various ionic species of carbon. Every point in the figure to follow is an average of five observations. Figure 23(a) shows the variation of line intensity of C I transition 2p ^2D - 3s $^1D^0$ with distance from the target at various helium gas pressures ranging from 10^{-3} Torr to 10 Torr. It is observed that line intensity is more in presence of helium gas than that in vacuum. Intensity of C I species increases when helium pressure is increased
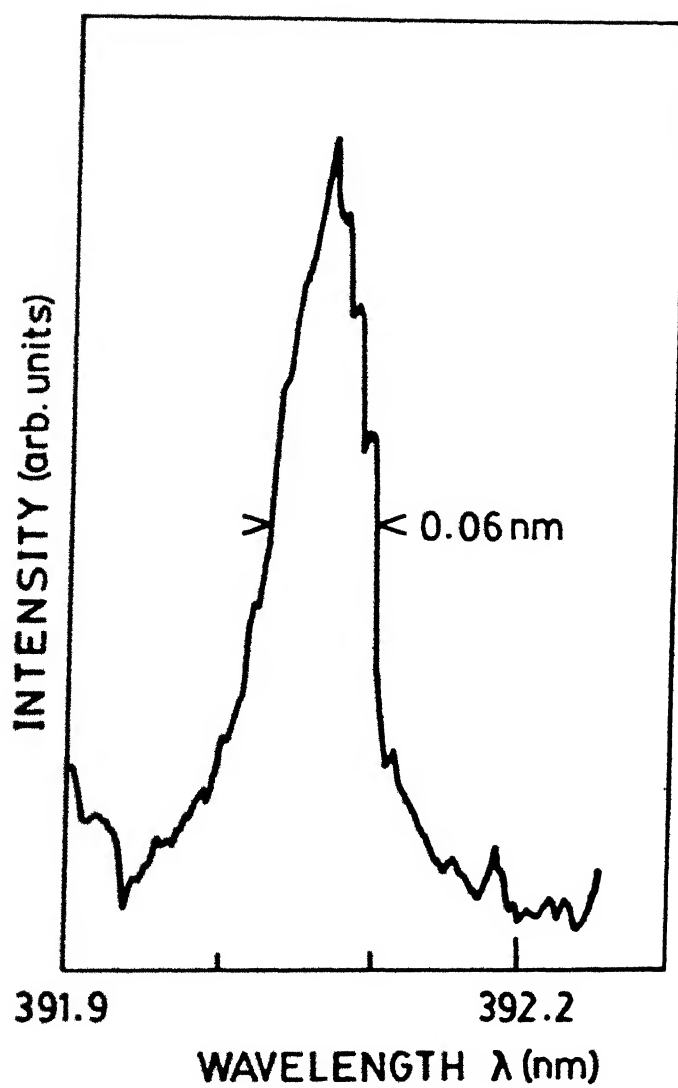
Fig. 21   Typical stark broadened profile of C II transition
3p $^2P^0$-4s ^2S at 392.0 nm for 1.06 μm irradiation in vacuum.
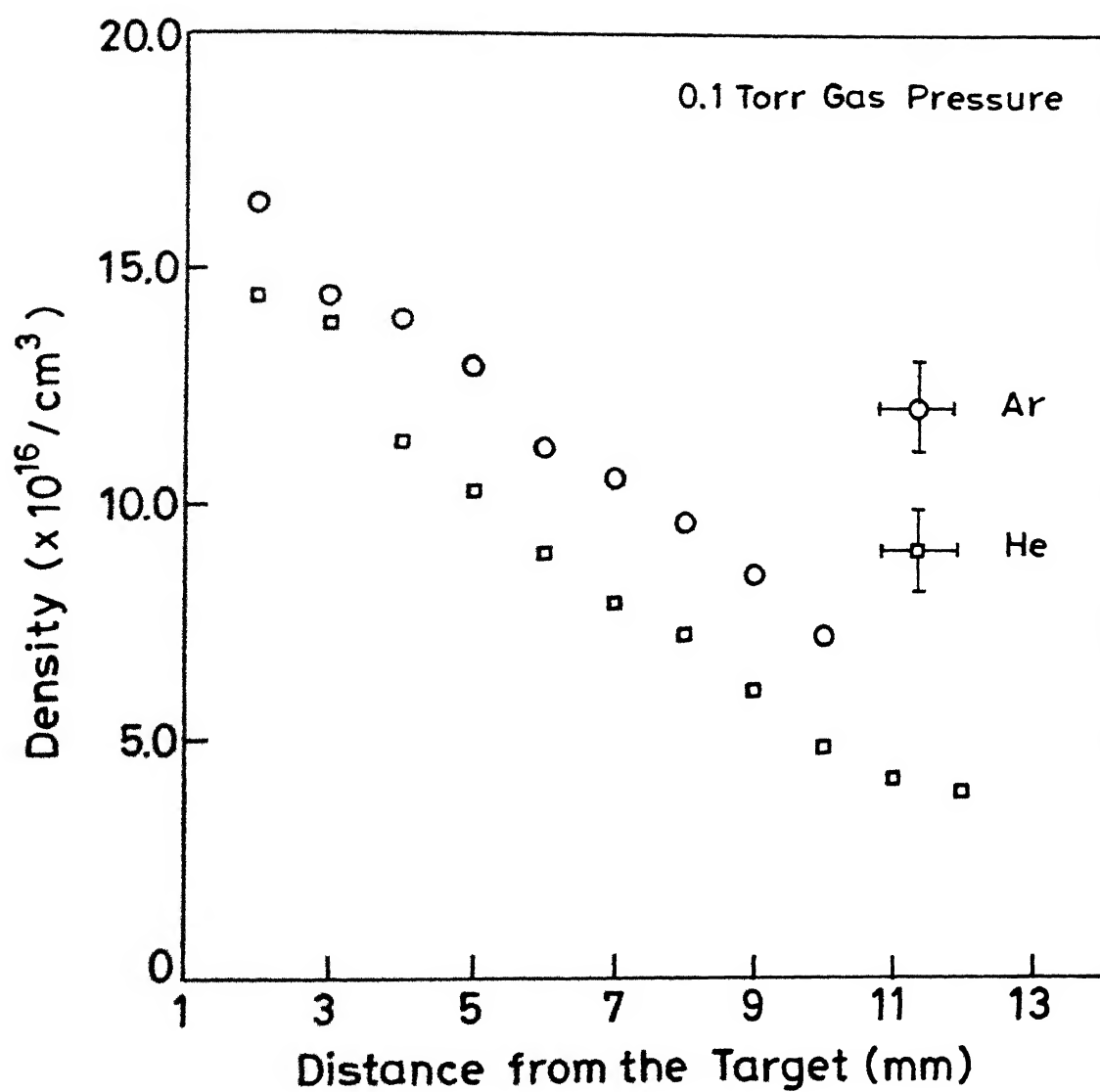
Fig. 22   Electron density of C II transition $3p\ ^2P^0 - 4s\ ^2S$ at 392.0 nm as a function of distance from the target at 0.1 Torr pressure of helium [open squares] and argon [open circles].

from 10^{-3} to 1 Torr but decreases for 10 Torr. In vacuum, the plasma expands freely where as in the presence of background gas plasma is confined to a smaller region which results in reduced expansion rate and hence enhanced cooling rate. The rate of change of electron temperature is sum of the three terms[125] viz. the elastic collision, electron heating due to collisional de-excitation of metastable ions and recombination of ions. The rate of loss of electron energy is dominated by the elastic collision term $Q_{\Delta T}$ given by

$$Q_{\Delta T} = - \frac{2m_e \sigma_{ea} \rho_2}{M_B} \left(\frac{8k_B T_e}{\pi m_e} \right)^{1/2} \qquad (45)$$

where σ_{ea} is the elastic scattering cross-section between the electrons and the atoms, ρ_2 is the density of background gas and M_B is the mass of the background gas atom. It follows from Eq. (45) that cooling is inversely proportional to M_B and hence lighter gas, helium in our case, is efficient for rapid cooling. It is also observed that as the gas pressure increases beyond a certain value, 1 Torr in our case, the enhancement slows down. Similar behaviour has also been observed for Al I transition in N_2 gas.[38] Figure 23(b) shows the variation of line intensity of C III transition $3d\ ^3D - 4f\ ^3F^0$ with distance from the target. It is observed that as the gas pressure is increased from 10^{-3} to 1 Torr the intensity increases and peaks at about 3 mm from the target but increasing pressure from 1 Torr to 10 Torr decreases the line intensity.

The studies were also done with argon as a background gas. Figure 24(a) shows the intensities of C I transition $2p\ ^2D - 3s\ ^1D^0$ at 193.1 nm, C II transition $3p\ ^2P^0 - 5d\ ^2D$ at 213.7 nm and C III transition $3d\ ^3D - 4f\ ^3F^0$ at 192.3 nm at a distance of 4 mm from the target at various argon pressures.
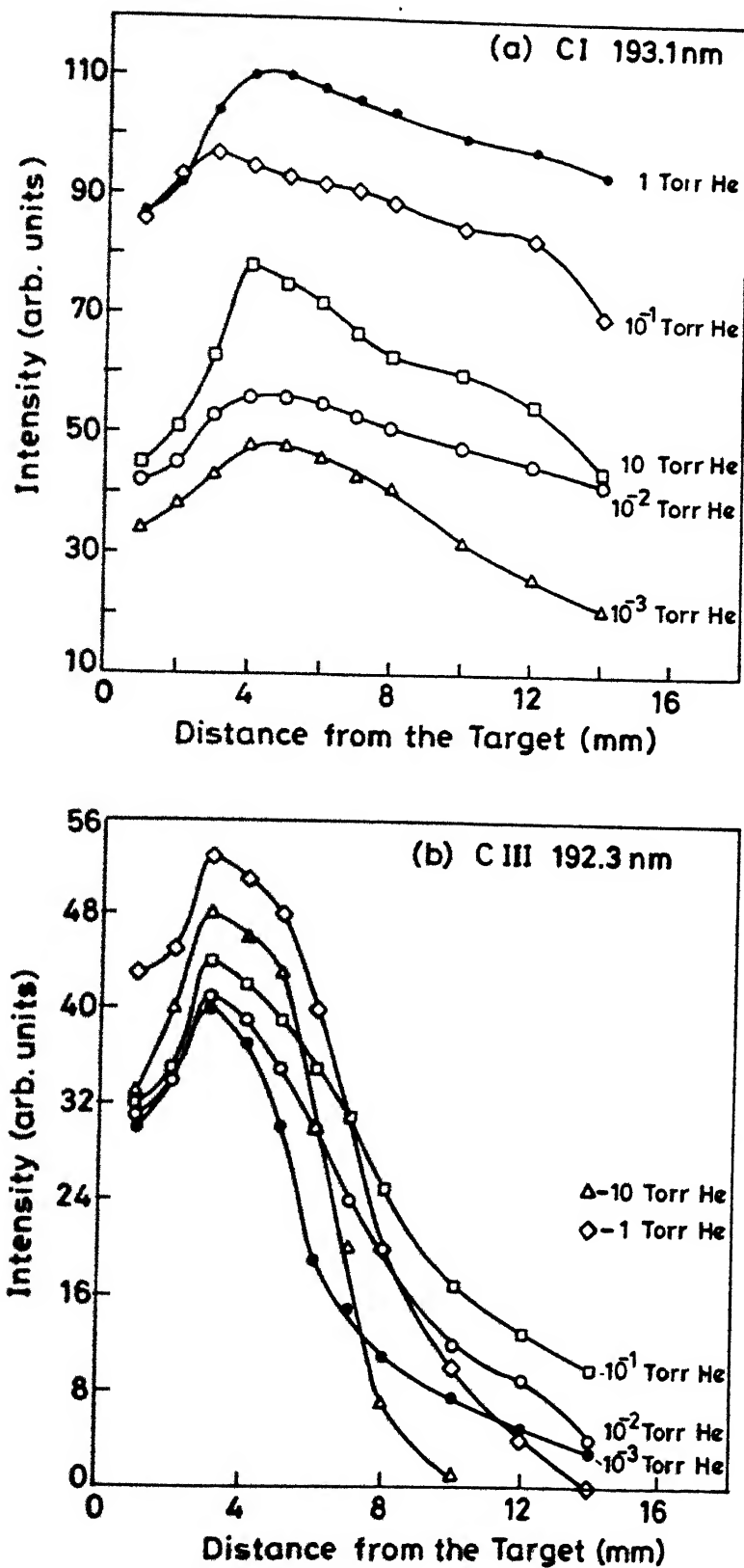
Fig. 23 Variation of line intensity with distance from the target at various helium pressures

(a) C I transition $2p\ ^2D - 3s\ ^1D^0$
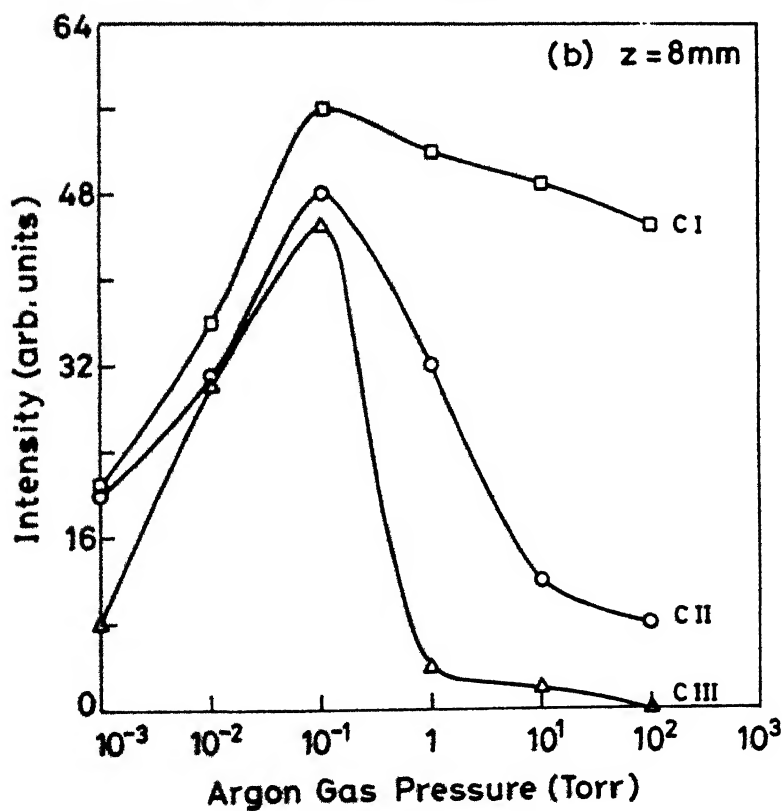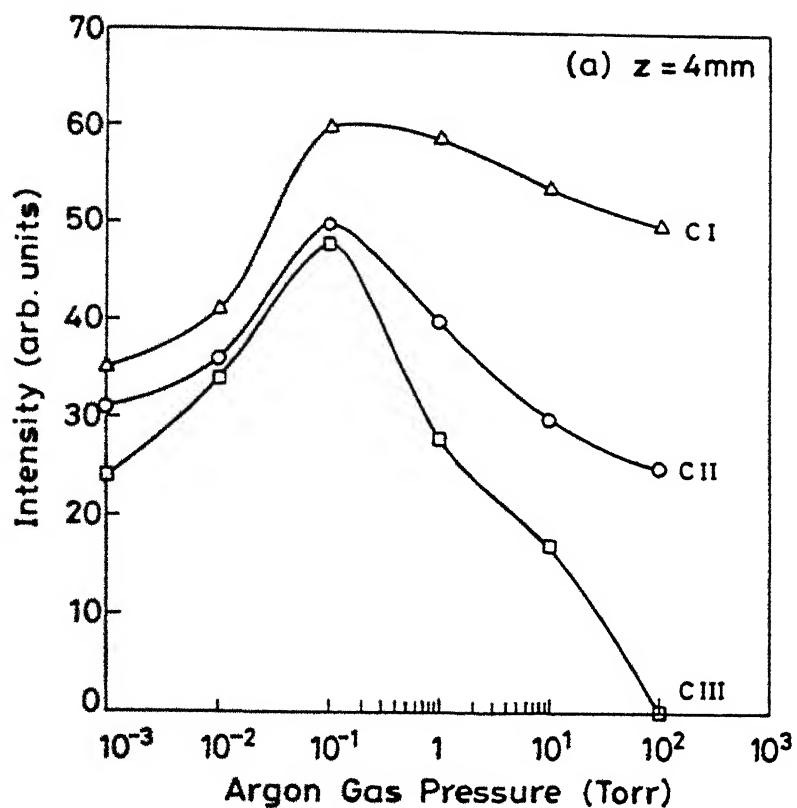
Fig. 24 Intensity of C I transition $2p\ ^2D - 3s\ ^1D^0$ at 193.1 nm, C II transition $3p\ ^2P^0 - 5d\ ^2D$ at 213.7 nm and C III transition $3d\ ^3D-4f\ ^3F^0$ at 192.3 nm at a distance of (a) 4 mm and (b) 8 mm from the target surface.

For C I and C II species intensity increases rapidly upto 0.1 Torr and decreases slowly beyond 0.1 Torr. Whereas, the intensity of C III line decreases rapidly after 0.1 Torr of argon gas pressure, decaying completely at 100 Torr. Figure 24(b) shows the intensities of C I, C II and C III lines at a distance of 8 mm from the target at various argon pressures. It is observed that the intensity of C III transition is almost insignificant after 1 Torr of argon pressure. This shows that presence of background gas affects higher species most. We observed a significant enhancement of the intensity of C III transition $3d\ ^1D - 4f\ ^1F^0$ at 216.3 nm in the presence of argon gas. Figure 25 shows the intensity variation of C III transition at 216.3 nm with distance from the target at various argon pressures. It is observed that the intensity of line attains a maximum value at a pressure of about 1 Torr at 4 mm from the target surface and then decreases with further increase in pressure upto 100 Torr. The decrease of intensity at high pressure is due to very high cooling rate. We observed more line enhancement for this transition in the presence of argon than in the presence of helium gas.

The significant enhancement of emission lines in the presence of background gas indicates an important role of interaction processes between the ambient gas and the plasma. The interactions which can result in populating the upper state could be collisional excitation, charge-transfer and the recombination process. To explain our observation, we discuss each one of the three possibilities. The collisional excitation from the ground state requires very large excitation energy to populate the upper states. Hence the possibility of collisional excitation process playing the main role in enhancing the observed line emission is very less. Charge transfer between the plasma ions and the atoms of the background gas can also populate the excited
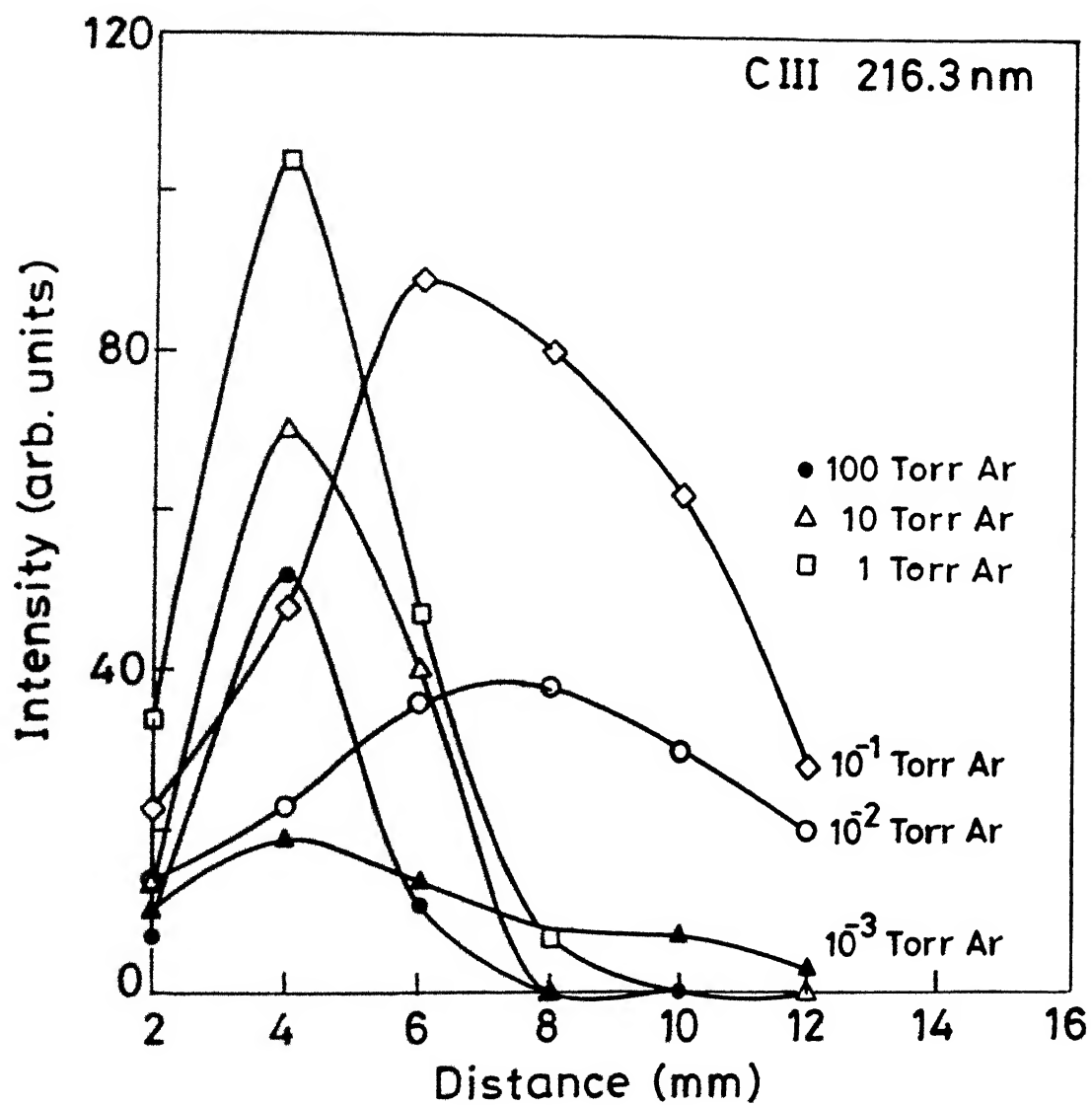
Fig. 25 Intensity variation of C III transition $3d$ ^1D – $4f$ $^1F^0$ at 216.3 nm with distance from the target at various argon pressures.

states. The cross-section calculated for the interaction of ambient gas and plasma ions from Eq. (12) is of the order of $\sigma \approx 10^{-18}$ cm^2. For the expansion velocity of the plasma front of the order of 10^7 cm/s, calculations of the charge transfer cross-section and rate show that this process can not be a dominant process. Moreover, the small difference in the charge state of the plasma ions and the gas atoms reduces the probability of charge transfer. It is found that three body recombination process is much more likely to occur in the presence of background gas. The density of carbon plasma decreases on expansion but still a significant rate of the three body recombination (Eq. 8) can exist at distances of few mm due to simultaneous reduction in temperature of the adiabatically expanding carbon plasma. The rate of the three body recombination, however, decreases at much larger distances where the recombination heating[126] becomes important resulting in a slow decrease of temperature during expansion and leading to freezing of the ionization.[85,86] The background gas essentially provides a heat sink so that the recombination process can continue for a longer period. Theoretical estimates[127] suggest that a background gas at a pressure of 0.1-10 Torr can significantly increase the cooling rate of electrons in the plasma region at 1-10 mm away from the target. Excitation of the background gas results in reducing the electron energy thereby increasing collisional cooling. Hence from Eq. (45) the role of the background gas lies in increasing the cooling rate of the plasma in the expansion region. Enhanced cooling of the expanding plasma increases the three body recombination rate, resulting in populating the excited neutral and ionic carbon species in the presence of background gases. Hence the three body recombination process is mainly responsible for the observed enhancement of the emission lines.

Double peak structure

The spatial and temporal characteristics of various ionic states at various pressures of air, helium and argon gases were studied using 1.06 μm laser irradiation. An interesting feature observed is the appearance of a hump in the temporal profile for the transition 3d ^{2}D - 4f ^{2}F^0 of C II at 426.7 nm at distances far away from the target surface (z greater than 8 mm) at pressure equal to or better than 10^{-3} Torr in the chamber. A single peak is observed for distance less than 8 mm. On increasing pressure in the chamber the hump takes a very distinct shape and the profile appears as a double peak structure at 0.1 Torr. Further increase in background gas pressure decreases the onset distance for the double peak structure. Figure 26 shows the effect of air pressure on the shape of the temporal profiles at 0.1 and 1 Torr. The second peak appears at a distance of 8 mm and 5 mm, respectively from the target at 0.1 and 1 Torr air pressure. Similar effect is observed when helium and argon gas are used as background gas. At low pressure i.e. 10^{-3} Torr of helium gas, a single peak is observed upto about 2 cm away and parallel to the target surface. For pressures 0.01, 0.1 and 1 Torr, the peak remained upto 1.8, 1.2 and 0.9 cm, respectively, from the target surface. Beyond these distances a hump like structure which eventually changes to a distinct double peak structure was observed. The onset distance for the second peak decreased with increase in pressure upto 1 Torr. The onset distance for the second peak decreased in the presence of argon gas, being less than that observed in helium background. However, the second peak disappears on further increase in the pressure beyond 1 Torr. Figures 27(a) and 27(b) show the shape of temporal profiles at 0.1 Torr pressure of helium and argon gas, respectively at various distances. The variation of delay in the peak intensities for the first and
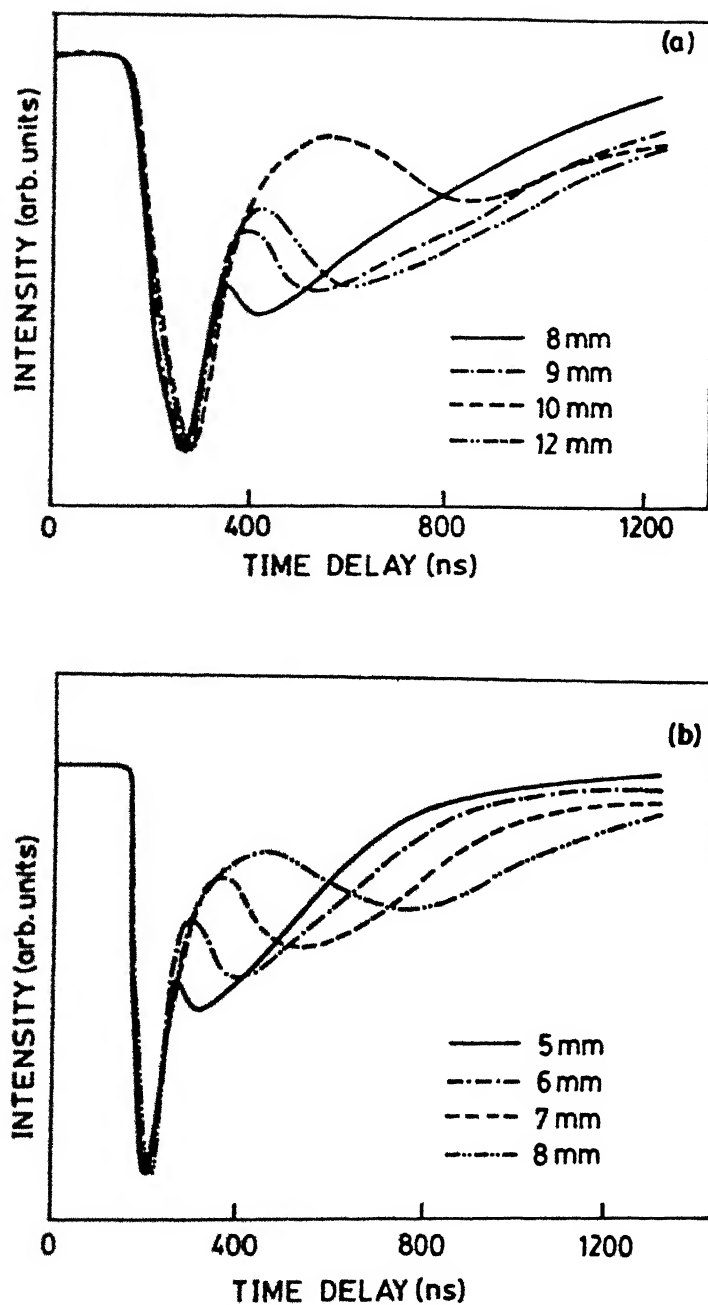
Fig. 26   Influence of the background gas (air) pressure on the shape
of the temporal profiles of C II transition 3d ^{2}D - 4f ^{2}F^0
at 426.7 nm at pressures (a) 0.1 and (b) 1 Torr and at
different distances from the target surface.
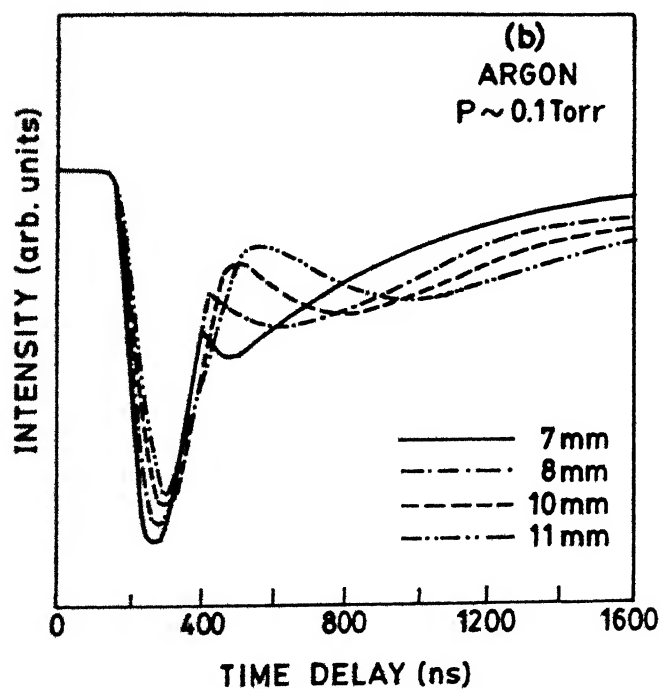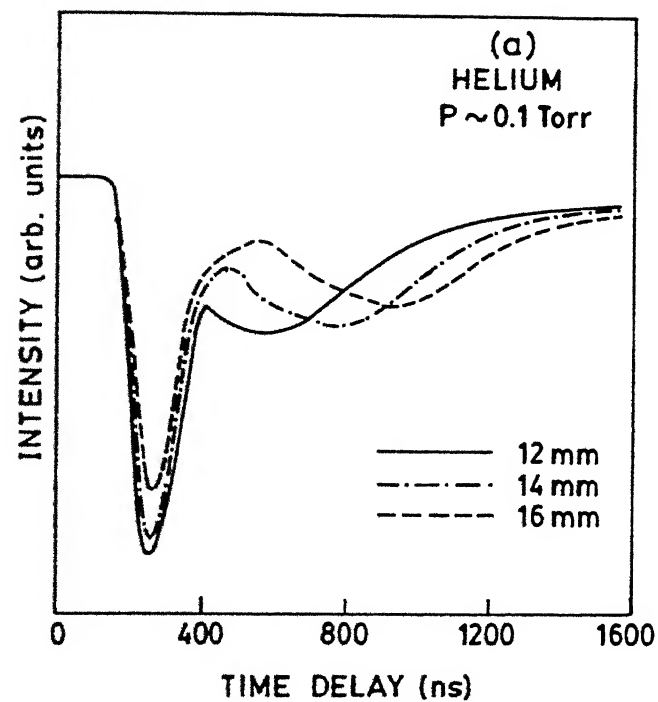
Fig. 27   Shape of the temporal profiles of C II transition
3d ^{2}D – 4f ^{2}F^0 at 426.7 nm at 0.1 Torr of (a) helium and
(b) argon at different distances.

second peak at different distances from the target for various pressures of air, helium and argon gases is plotted in Figs. 28(a), (b) and (c), respectively. The slope of the curves shows that second peak is decelerated fast whereas the first peak accelerated slowly with the increase in gas pressure.

In general, the existence of the above structure could originate from processes like (a) electron-ion recombination interactions within the plasma, (b) collisional interactions between the expanding ions and ambient gas molecules, (c) blast/shock wave interactions and (d) stratification of the plasma due to instabilities occurring at the interface between laser plasma and the ambient gas.[79] Calculations of rate coefficients show that radiative and three body recombination are not dominant phenomena. Moreover, these processes cannot explain a sudden rise of second peak in the temporal profiles at a particular distance. We have not observed the increase in the intensity of the emission line at distances where second peak appears in the temporal profiles, hence the phenomenon cannot be explained on the basis of recombination interactions. Interaction like resonance charge transfer is a velocity dependent one.[28] In our experiment, we find that the faster components have velocities an order of magnitude less than that reported by Dixon et al which makes the resonance charge transfer process a less probable one in our case. Dixon et al[28] have shown that the charge transfer is dominant for the transitions originating from n = 4 levels whereas we found that the double peak structure is pronounced for C II transition originating from n = 4 excited state at 426.7 nm, but the effect is not observed for the transitions at 407.4 nm and 588.9 nm which also originate from n = 4 levels. We also observed the double peak structure for lines originating at n = 2 and 3 levels
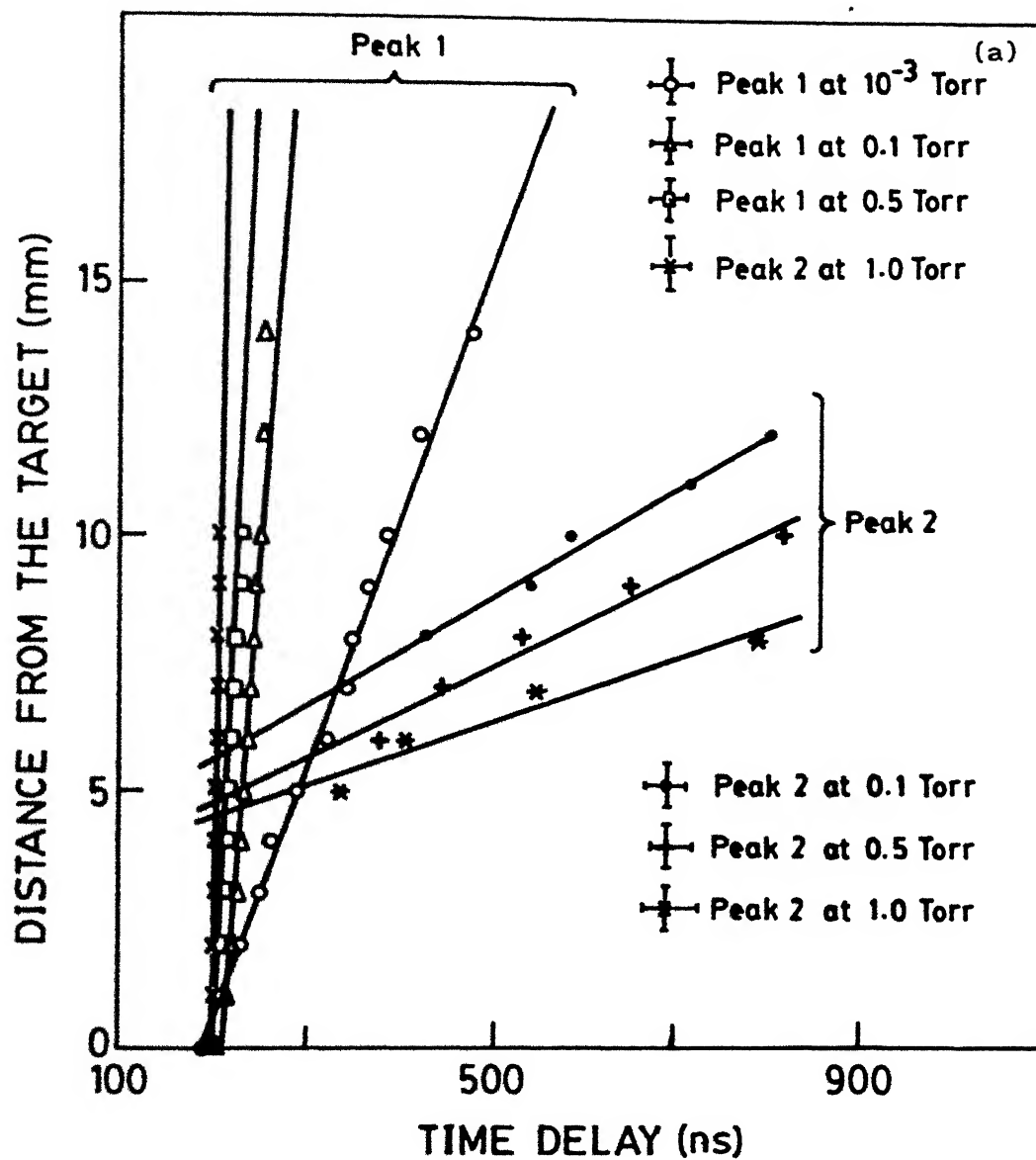
Fig. 28 Variation of time delay in the peak intensities for the first and second peak of C II transition 3d ^{2}D - 4f ^{2}F^0 at 426.7 nm at different distances for various pressures of (a) air.
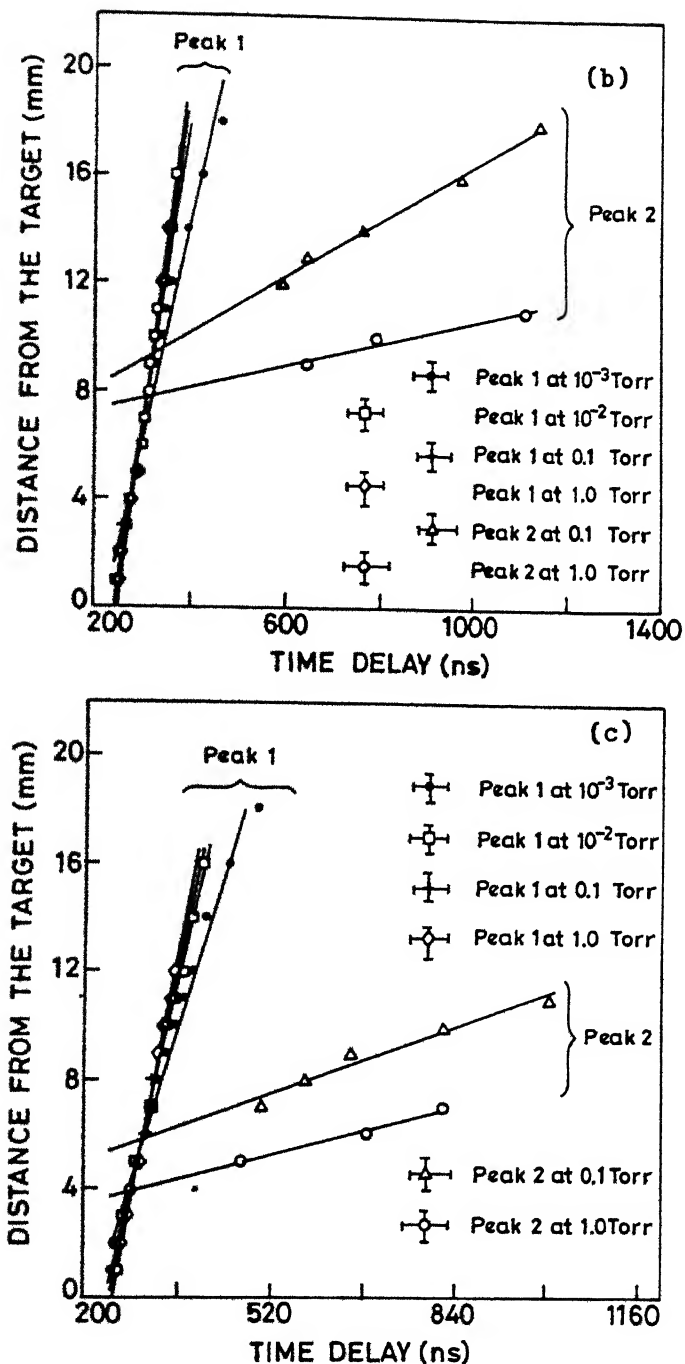
Fig. 28   Variation of time delay in the peak intensities for the first and second peak of C II transition 3d ^2D - 4f $^2F^0$ at 426.7 nm at different distances for various pressures of (b) helium and (c) argon.

respectively at 251.2 nm and 283.7 nm. Thus the phenomenon of double peak structure can not be explained on the basis of electron ion recombination and charge transfer processes. Collisionless interactions are neglected as they are mainly important only at smaller distances. Blast/shock wave interactions occurring in the presence of background gas may play an important role in double peak behaviour. In the presence of ambient gas at high pressure plasma expands supersonically forming a shock wave. As the shock expands, more and more background gas is swept away by the shock wave and hence the expansion velocity decreases with the increasing distance z from the target surface. The motion of the blast wave front is governed by the Eq. (13). In our studies, it is found that C II fast and slow ion trajectories do not fit well with the simple blast wave model given by Eq. (13). We get nearly $z \propto t$ and $z \propto (t)^{0.6}$ dependence for helium and argon at 0.1 and 1 Torr pressure for fast and slow ions, respectively. Thus the phenomenon of the double peak structure cannot be explained on the basis of blast wave interaction.

The shape of the expanding plasma was also observed visually to look for any changes in the pattern of expanding plume. At low pressure ($<10^{-3}$ Torr), the expanding plume is smooth. As the pressure increases the plasma front breaks up and forms a separate luminous region which eventually becomes bracket shaped, a shape similar to an irregular sickle. Visual observations at background gas pressure of 0.1 Torr can well be compared with Anan'in et al[42] where they explained the onset of micro-instability using high speed photography at 0.26 Torr of air pressure as evidenced by the asymmetric luminous region having the structure similar to a bracket in the expanding plasma (Figs. 2 and 3 of Ref 42). Accordingly, the increase in growth of instability was evidenced by the increase in intensity and dimensions of

bracket shape structure. In our case, the increase in the number of peaks at the plasma front with pressure signifies the increase in growth of turbulence. At pressures less than 10^{-3} Torr, plasma is fairly homogeneous in its structure. The inhomogeneities of the laser power density in the laser focussed spot[128,129] can give rise to fast and slow ion components near the target surface. We do not observe the separation of the two components close to the target surface. We observe that at low pressures $< 10^{-3}$ Torr, density of plasma ions decreases largely due to expansion and fast recombination processes resulting in mutual penetration of the plasma and the gas. During interpenetration, transfer of kinetic energy from the laser plasma to the background gas takes place and energy and momentum exchange occur. When pressure is increased to 10^{-2} Torr, the interaction region shifts towards the target due to increased density of ambient gas. At Pressure $\sim 10^{-1}$ Torr, mutual penetration of the laser plasma ions and the ambient gas decreases and interaction region becomes narrower, thus forming an interface. It is expected that near the interface the instabilities like Rayleigh-Taylor sets in the plasma. Furthermore, density fluctuations in the interface region leads to deceleration of laser plasma front. Due to interface formation and density fluctuations, stratification effect in the plasma increases where fast component penetrates the ambient gas and the slow one decelerates due to appearance of instability and consequently gives rise to a distinct double peak structure in temporal profiles. The growth of the Rayleigh-Taylor Instability and the density of ambient gas at which this instability dominates are given by Eqs. (34) and (37), respectively. Using our experimental parameters[79] viz R, the distance from the target surface where distinct double peak structure appears $\simeq$ 0.8 cm for air, 0.7 cm for argon, and

1.2 cm for helium and M $\propto$ 10^{-6} g gives ρ_2 $\simeq$ 1.3 x 10^{-7} g/cm^3, 1.9 x 10^{-7} g/cm^3 and 3.9 x 10^{-7} g/cm^3 corresponding to the gaseous pressure of 0.16 Torr, 0.09 Torr and 0.18 Torr close to our experimental value of 0.1 Torr. The onset distance decreases with the increase in mass of the ambient gas, a fact observed experimentally also. Using the estimated density of the laser plasma ions we find that at lower pressures $\rho_1 > \rho_2$ in the interaction region whereas at higher pressures $\rho_2 \geq \rho_1$ and acceleration is negative. Also it follows from Eq. (34) that $n^2 > 0$ at lower pressures whereas $n^2 < 0$, in agreement with the condition for the growth of the instability at 0.1 Torr.

We did not observe second peak for C III and C IV species. However, for C I transition $2p^2$ ^1S – $3s^1$ p^0 at 247.9 nm we observed fast and slow component of the neutral species at low pressure also, but no change in the structure was observed with increase in the pressure upto 1 Torr, moreover, the onset distance of the second peak did not change with pressure. Figure 29 shows variation of delay in the peak intensities for second peak of C I transition at different distances from the target for various helium pressures. This observation is similar to the double peak structure reported by Dixon et al[129] in helium atmosphere (1-10 Torr) and could be explained from the blast wave model.

In conclusion, we estimated temperature, density and expansion velocity of the laser ablated carbon plasma at moderate irradiance as a function of distance from the target. Variation of electron temperature with laser intensity shows $I^{0.4}$ dependence for all species. Electron density was calculated from stark broadened profile in vacuum and in the presence of ambient gases. It is found that expansion velocity of the plasma front increases with the increase in ionic charge, however, decreases with the
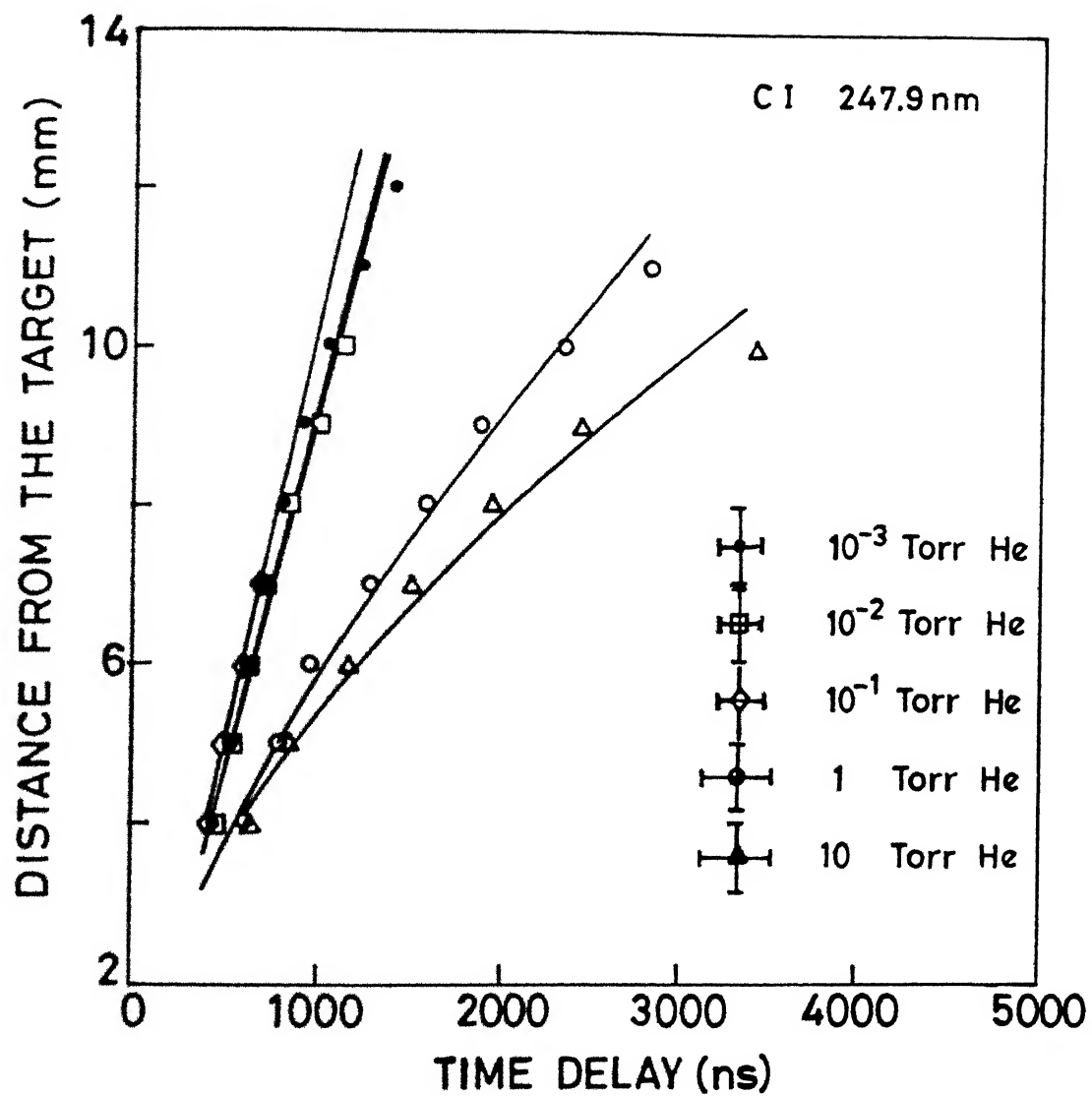
Fig. 29 Time Delay for the appearance of the second peak of C I transition $2p^2\ {}^1S - 3s^1\ P^0$ at 247.9 nm with distance from the target at various pressures.

increase in the atomic mass of the ambient gas. The role of various interaction processes in enhancing the line emission in the presence of helium and argon is presented. From double peak structure in temporal profiles of the C II transition 3d ^{2}D - 4f ^{2}F^0 at 426.7 nm, an investigation of the transition from mutual penetration to interface formation between carbon ions and background gas is reported. At the interface region due to density fluctuations, Rayleigh-Taylor instability (RTI) occurs in the decelerating laser plasma front which leads to stratification of the plasma. Pressure at which RTI occurs at the interface is estimated theoretically which compares well with our experimental observation. It is found that distance of occurrence of instability decreases with the increase in atomic mass of the gases.

LASER ABLATED CARBON PLASMA AT LOW INTENSITIES

INTRODUCTION

At moderate laser intensities ($\sim 10^9$-10^{12} W/cm^2) atomic/ionic species from C V to C I which recombine through atomic to molecular carbon species are observed. However, at low laser intensities ($\sim 10^8$-10^9 W/cm^2) molecular C_2 emission was found to dominate in laser ablated plasma. At moderate irradiance emission spectrum comprises of discrete lines of different ionic species of carbon as shown in Fig. 13. It is seen that decreasing the laser intensity to 10^8 W/cm^2, discrete emission lines disappear whereas C_2 bands appear in the emission spectrum. Hence, depending on the intensity of incident laser radiation it is possible to get high ionic states or molecular states of carbon. Recently, the laser ablated plasmas at low irradiance have found applications in the production of cluster source,[131] preparation of high T_c superconducting thin films,[132] deposition of metals, carbon clusters[74,133,134] and for unhydrogenated diamond like carbon (DLC) films.[135] It is found that high quality diamond like films are obtained at low laser power densities of $\sim 10^8$ W/cm^2 where molecular C_2 emission is most dominant.[12,50,57] The structural properties of the films prepared by pulsed laser deposition depend on simultaneous control of laser and processing parameters, thus for optimization of the film a better understanding of the dependence of film formation on the laser and plasma parameters is essential. It has been found that energetic ionized and excited particles in the plasma plume influence the growth of high quality thin films. Therefore, it is necessary to estimate energy or temperature of the species which dominate in a deposited film. Many researchers have tried to estimate the temperature of the

energetic species at low laser irradiance.[12,50,57] It has been observed that the characteristics of C_2 emission essentially define the quality of deposition of thin films on substrates.[50] The C_2 emission is also important in astrophysics and flame spectroscopy.[42,136] Optical emission studies of C_2 Swan bands using KrF-excimer laser in an ambient gas mixture of Ar and H_2 while depositing thin films have been reported by Chen et al.[50] Swan bands of C_2 have also been reported from laser vaporization of graphite in a pulsed helium flow.[131] Recent results show that the efficient material removal and congruent evaporation of multi-component targets at shorter wavelengths (UV) yield superior films, therefore generally excimer lasers at 193, 248, 308 nm and Nd:YAG laser at 0.532 μm and 0.355 μm are used for deposition of good quality films.[137] Optical emission studies of the plasma plume can yield important information on the pulsed laser deposition process and lead to better understanding of the laser ablated plasma with and without inert gas. In general, properties of carbon films prepared by pulsed laser ablation range from soft and graphitic to hard and diamond-like, depending on the energetic particles present in the plasma plume and on the deposition parameters, such as laser power density, laser wavelength, background conditions, substrate temperature.

In the present chapter,[46,93,94] a systematic investigation of optical emission studies of the molecular carbon C_2 produced by irradiating graphite target with Nd:YAG laser and its harmonics at different laser energies and helium gas pressures is reported. The temporally and spatially resolved studies of emitted particles of laser ablated carbon at low irradiance are performed. The present study is aimed at understanding the role of ambient gas and for correlating the deposited film properties with plasma

plume parameters. These studies are helpful to optimize parameters for diamond like carbon film deposition, to correlate carbon clusters with the plasma dynamics and to investigate the spectroscopy of small carbon clusters.

EXPERIMENTAL SET UP

The experimental set up and data acquisition arrangement used for recording plasma emission was similar to the one described in Chapter II. The laser radiation up to 1 J in 8 ns at its fundamental at 10 pps was focussed onto a rotating graphite target enclosed in a vacuum chamber using a 65 cm focal length lens. The vacuum chamber was evacuated to a pressure of $\leq$ 10^{-3} Torr and then filled in with helium gas at desired pressures.

RESULTS AND DISCUSSION

At higher laser irradiance 900 mJ of laser energy the plasma emission was dominated by atomic/ionic species from C V to C I which recombine through atomic carbon to molecular carbon far away from the target surface.[79] Figure 30 shows an emission spectrum of carbon plasma at 10^{-1} Torr of helium gas pressure at 600 mJ laser energy and 3 mm away from the target surface in the wavelength range 500-600 nm. It is evident that the ionic, atomic and molecular transitions are observed. However, at low irradiance viz. 60 mJ of laser energy molecular C_2 emission was found to dominate. Figure 31 shows the emission spectrum at 1 Torr of helium gas pressure at 60 mJ of laser energy. The spectrum is dominated by C_2 emission in the $\Delta v = -2, -1, 0, +1, +2$ sequences of the Swan ($d^3\Pi_g - a^3\Pi_u$) bands and the $\Delta v = 0$ and +1 sequences of the Deslandres - d'Azambuja ($C^1\Pi_g - A^1\Pi_g$) bands.[131] We have not observed C_3 emission i.e. cometary bands[138] at 405 nm with and without helium gas in our
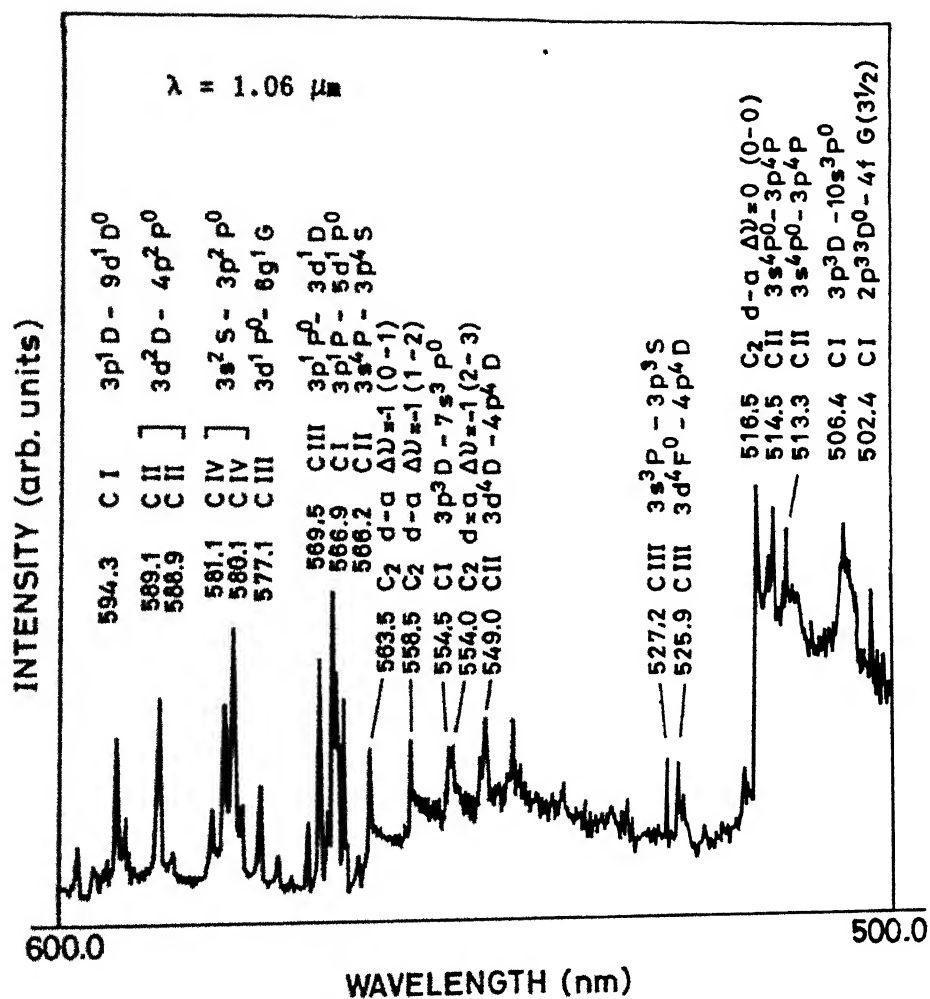
Fig. 30 Emission spectrum of carbon plasma at 10^{-1} Torr of helium gas pressure at 600 mJ of laser energy at 3 mm away from the target surface in the spectrum range 500-600 nm.
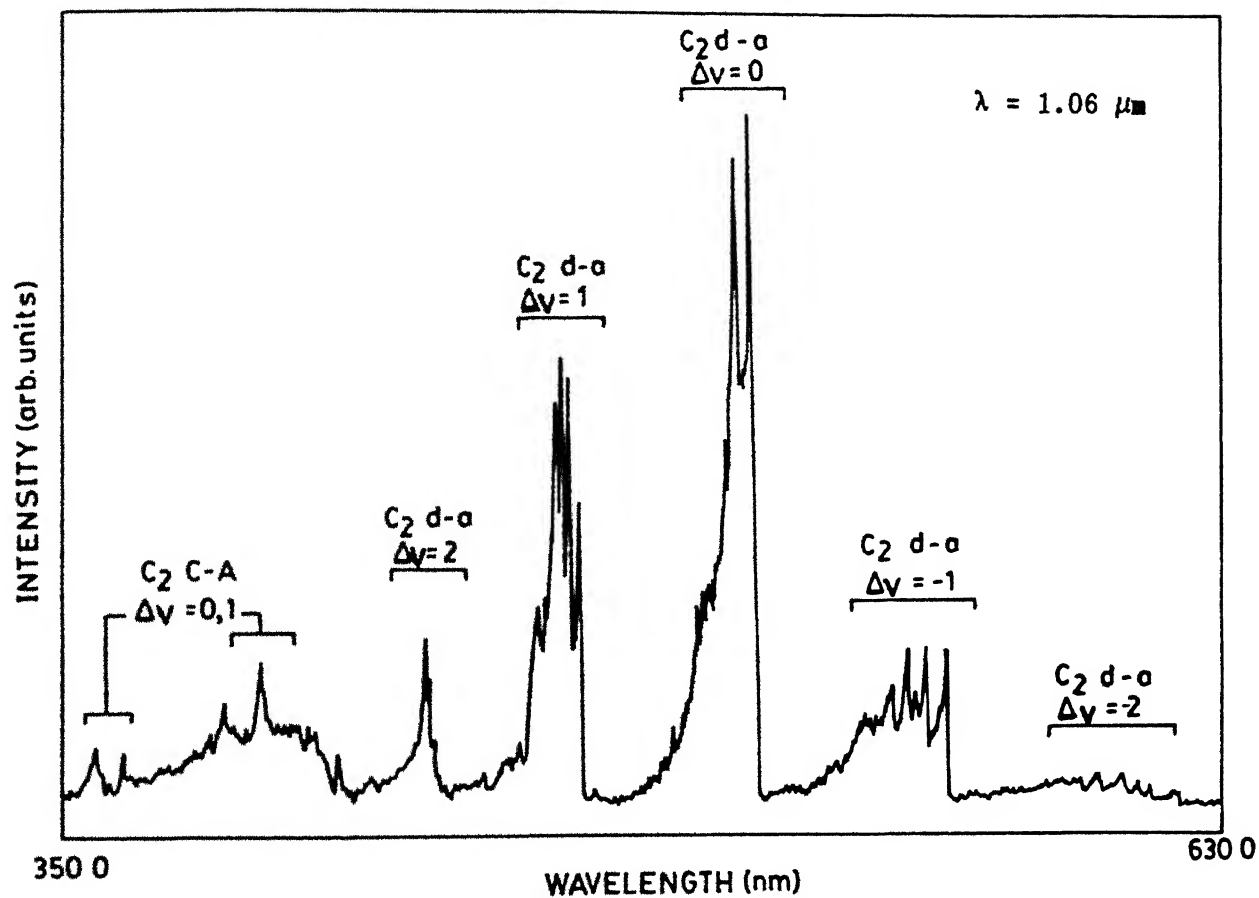
Fig. 31   Emission spectrum of carbon at 1 Torr of helium gas pressure at 60 mJ of laser energy.

experiment. However, in addition to C_2 lines, some C I and C II lines were also present. The presence of helium gas increased the intensity of emitted spectrum and all band heads. Figure 32 shows emission spectrum of the C_2, d -a $\Delta v = 0$ Swan band sequence in the wavelength range 500-520 nm at 10^{-1} Torr of helium gas pressure. At 10^{-3} Torr pressure, only Swan band heads (0-0) at 516.5 nm, (1-1) at 512.9 nm, (2-2) at 509.7 nm were seen. Further increase in the pressure of helium gas to 10^{-2} Torr showed slight increase in the intensity of band heads. At 10^{-1} Torr not only the intensity of band heads increased but two band heads (3-3) at 507.0 nm and (4-4) at 505.6 nm also appeared. Increase in the pressure from 10^{-1}-100 Torr, showed slight increase in the intensity but no more bands. Figure 33 shows the $\Delta v = -1$, Swan band sequence at 10^{-2}, 1 and 100 Torr of helium gas pressures. Swan bands of $(v'-v'')$ i.e. (0-1) at 563.5 nm, (1-2) at 554.0 nm, (3-4) at 550.1 nm and (4-5) at 547.0 nm were observed at all the above mentioned helium gas pressures. Similar to $\Delta v = 0$ band sequence we observed that intensity of C_2 band heads for $\Delta v = -1$ band sequence suddenly increases at 10^{-1} Torr and does not change significantly for pressures upto 100 Torr. Figure 34 shows the spectra of the C_2 d-a, $\Delta v = -1$ Swan band sequence at 10^{-1} Torr of helium gas at 30, 60 and 90 mJ of laser energy. It was found that intensity of C_2 band heads increased at lower laser energies but after 60 mJ of laser energy intensity of C_2 band heads became almost constant. Figure 35 shows the $\Delta v = 1$, C_2 Swan band sequence at pressure of 10^{-1} Torr of helium gas. The bands (1-0) at 473.7 nm, (2-1) at 471.5 nm, (3-2) at 469.7 nm, (4-3) at 468.4 nm and (5-4) at 467.8 nm are prominent. This sequence also behaved similar to $\Delta v = 0$, -1 sequence at 10^{-1} Torr and higher pressure of helium gas. Figure 36 shows the $\Delta v = -2$ Swan band sequences at 10^{-2} Torr of helium gas pressure at 80 mJ
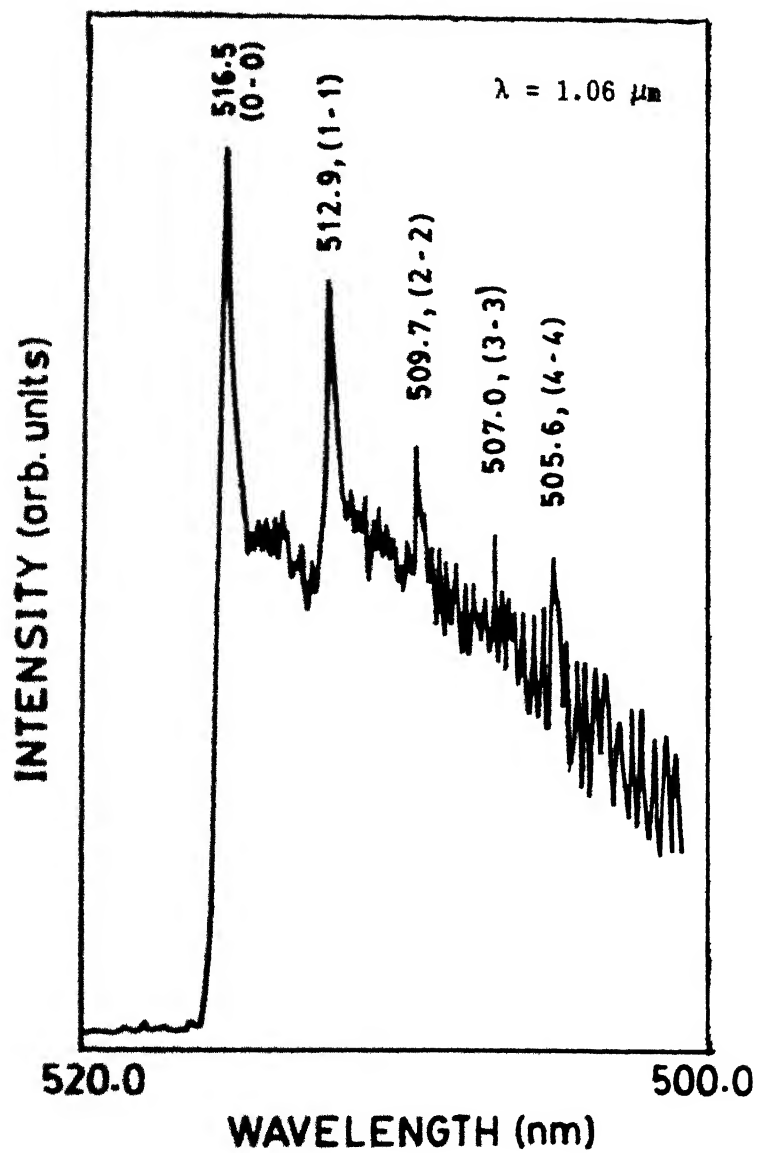
Fig. 32 C_2 d-a, $\Delta v=0$, Swan band sequence at 10^{-1} Torr of helium   gas
pressure at 60 mJ of laser energy.
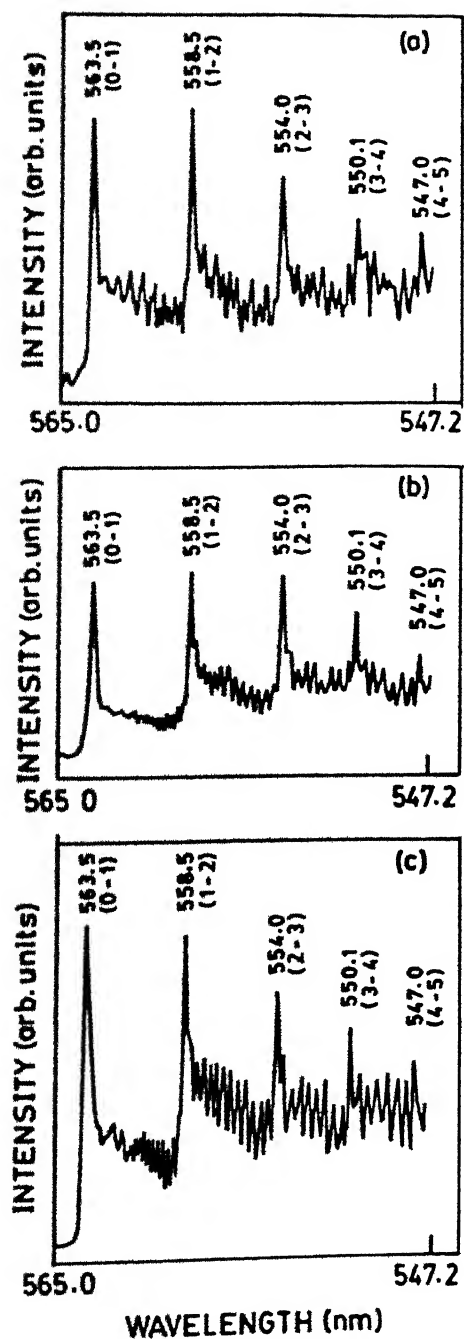
Fig. 33 C_2 d-a, Δv=-1, Swan band sequence at (a) 10^{-2}, (b) 1 and (c) 100 Torr of helium gas pressures at 60 mJ of laser energy using 1.06 μm laser irradiation. The intensity in (b) and (c) is five times that of (a).
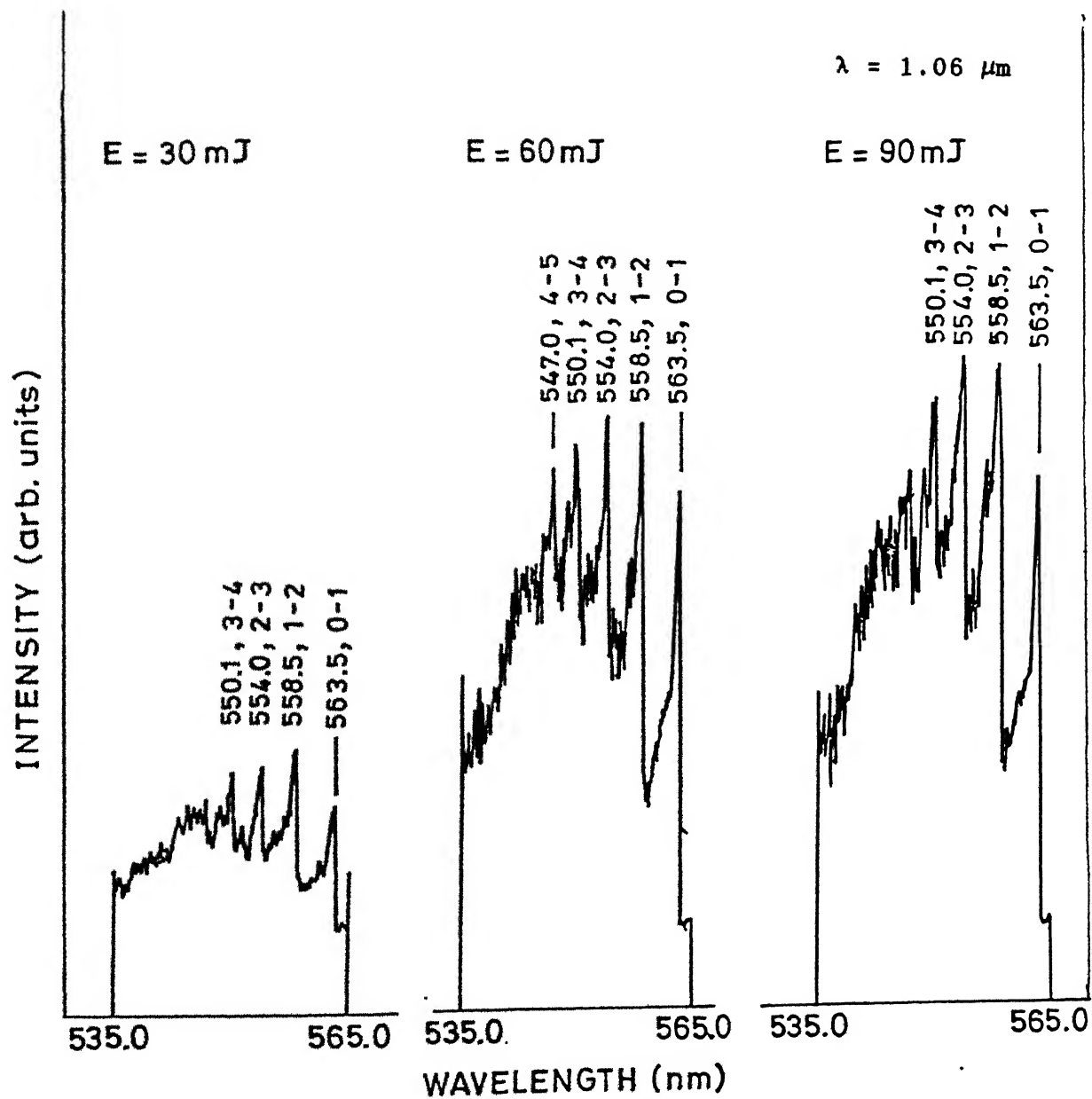
Fig. 34 C_2 d-a Swan band sequence $\Delta v = -1$ at 10^{-1} Torr of helium gas pressure at 30, 60 and 90 mJ of laser energy.
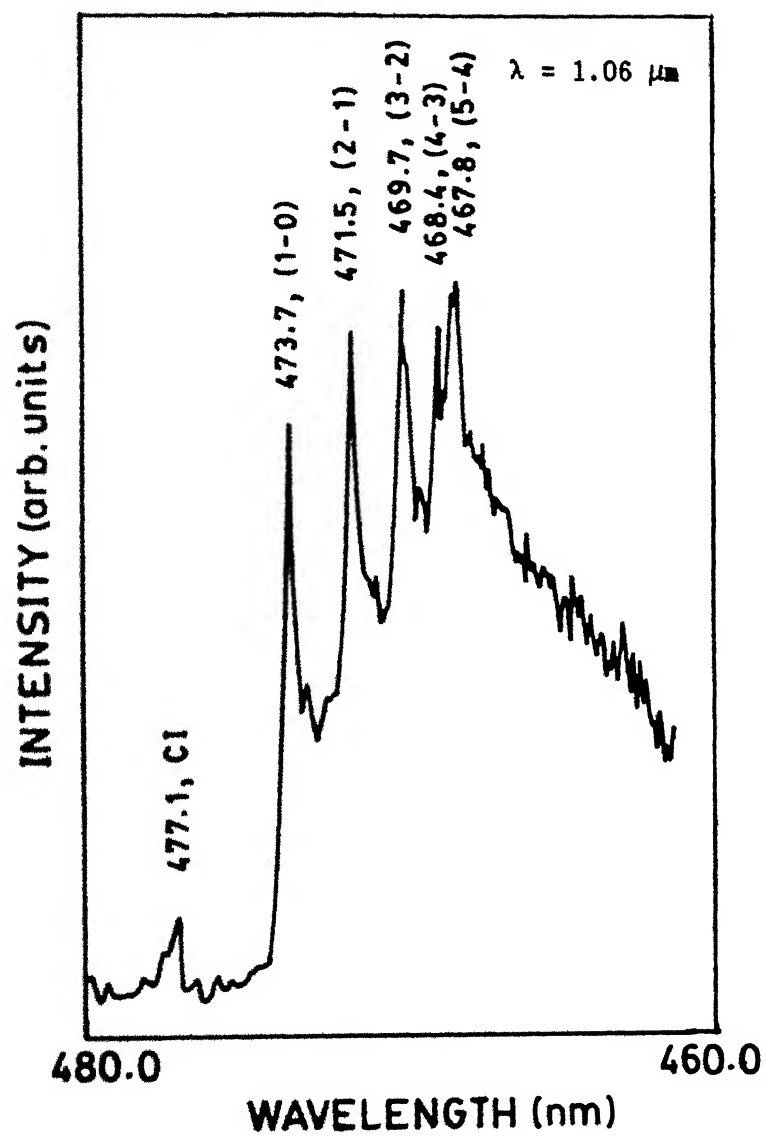
Fig. 35 C_2 *d-a*, $\Delta v=1$, Swan band sequence at 10^{-1} Torr of helium gas pressure at 60 mJ of laser energy.
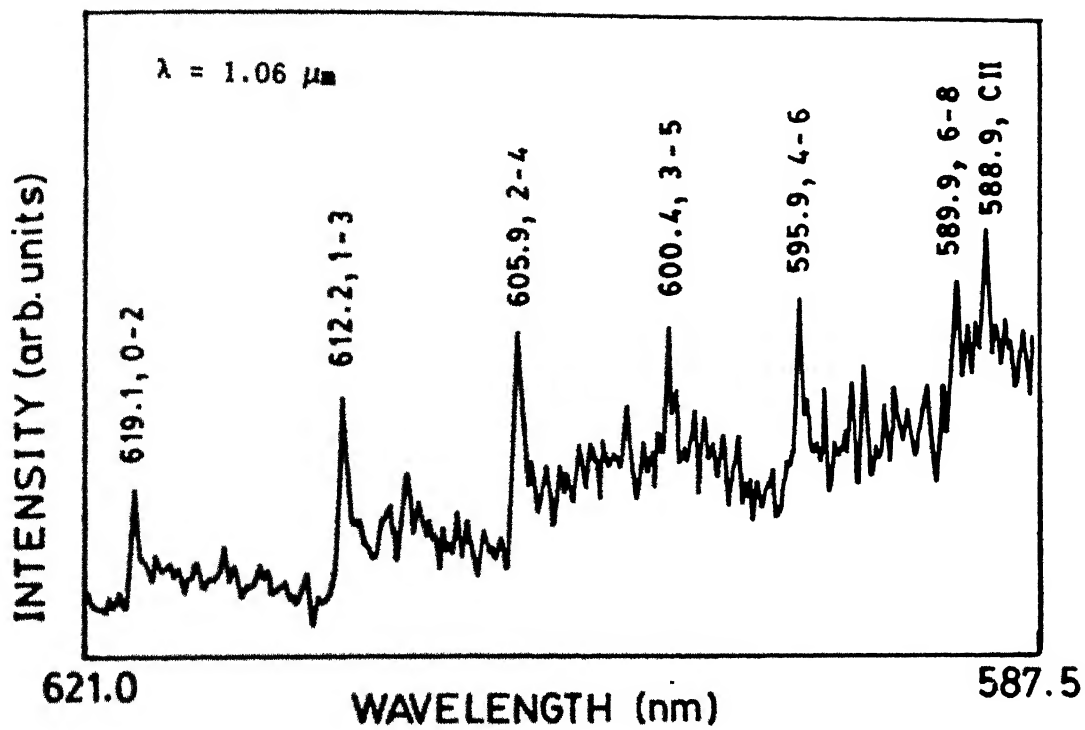
Fig. 36 C_2 d-a, $\Delta v=-2$, Swan band sequence including (6-8) high
pressure band and C II ionic line at helium gas pressure of
10^{-2} Torr at 80 mJ of laser energy.

of laser energy. Swan band heads of (0-2) at 619.1 nm, (1-3) at 612.2 nm, (2-4) at 605.9 nm, (3-5) at 600.4 nm and (4-6) at 595.9 nm were observed. In addition to these, we also observed the so called "high pressure" band of the Swan system at 589.9 nm which originates from v'= 6 level and C II atomic line at 588.9 nm. The high pressure (HP) bands were first observed by Fowler[139] from an electrical discharge through CO at relatively high pressure. In our experiment this band sequence was only evident at 10^{-2} Torr and 10^{-1} Torr of helium gas pressure and completely diminished on further increasing the helium gas pressure, in agreement with earlier reports.[131,140] HP bands were also reported[50] at high pressure of 100 Torr of argon gas but were not observed at high pressures of helium gas.[131] In our experiment, since the high pressure bands were observed only at 80 mJ of laser energy and in the presence of helium gas at 10^{-2} and 10^{-1} Torr where atomic carbon lines were also observed suggests that the origin of these bands is in fast recombining phase of plasma. The intensity of laser for observing these bands being not very large implies that C_2 bands are formed from atomic carbon recombination. Our conclusion is similar to Little et al[80] where they showed that appearance of these bands is critically dependent on the laser intensity and proposed that the upper level of these bands is populated via a potential-curve crossing by the metastable (Fig. 2) state which is populated preferentially during the formation of C_2 from free carbon atoms. The proposed mechanism for production of the upper level of the HP and Swan bands which is consistent with experimental and theoretical evidence is according to the following sequence of reactions[80] :

$$C + C + M \longrightarrow C_2(^5\Pi_g, v) + M$$

$$C_2(^5\Pi_g, v) + M \longrightarrow C_2(^5\Pi_g, v=o) + M$$

$$C_2(^5\Pi_g, v=o) + M \longrightarrow C_2(d^3\Pi_g, v=o-6) + M \qquad (34)$$
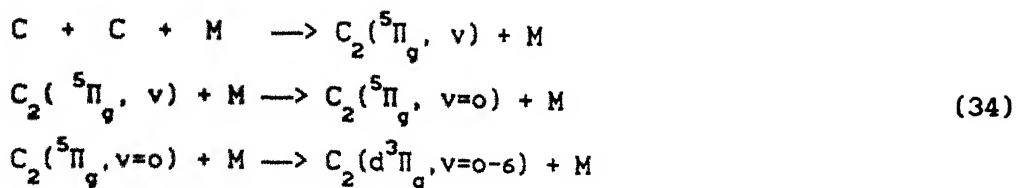
where M is the collision partner. Figure 37 shows the variation of the intensity of C_2 Swan band sequence (2-0) at 436.4 nm, (3-1) at 437.1 nm and (4-2) at 438.2 nm with helium pressures. The intensity of bands increased as the pressure of helium gas increased from 10^{-3} to 100 Torr.

Vibrational Temperature

Laser ablated plasma at low irradiance is mostly used for thin film deposition. It is found that properties of the laser ablated particles in the ablation plume greatly affects the quality of deposited films but the details of the particles behaviour are not fully understood. Quality of the film is severely effected by the energy of the particle being deposited and hence by the temperature. Therefore, it is necessary to estimate the temperature of the species which dominate in a deposited film. Various techniques have been utilized to estimate the temperature during dynamic changes in both temperature and electron density in a laser produced plasma at low irradiance.[12,50,57] We used C_2 Swan band head intensities to estimate temperature of the laser ablated plasma at low irradiance. Figure 38 shows the relative population of the upper vibrational level as derived from the measured intensities (Eqs. (43) and (44)) against vibrational quantum number for helium gas pressure of 1 Torr for 1.06 μm laser radiation at 60 mJ laser energy, the slope of the curve gives vibrational temperature 9168 K. Figure 39 shows the variation of vibrational temperature calculated from C_2 Swan bands $\Delta v = -1$ with helium gas pressure. Vibrational temperature decreases with
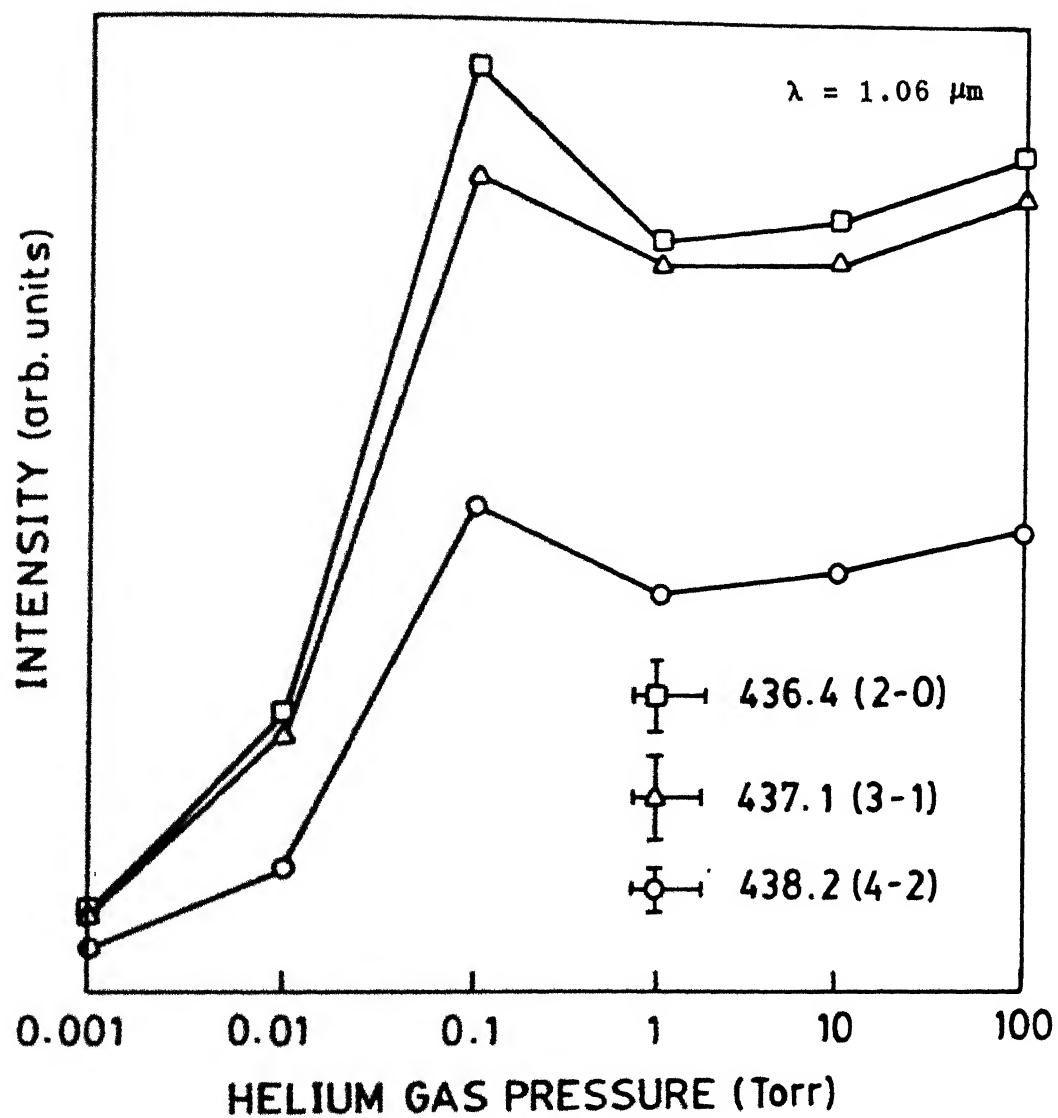
Fig. 37   Variation of intensity of C_2 d - a, Δv = 2, Swan   band
sequence with helium pressure at 60 mJ of laser energy.
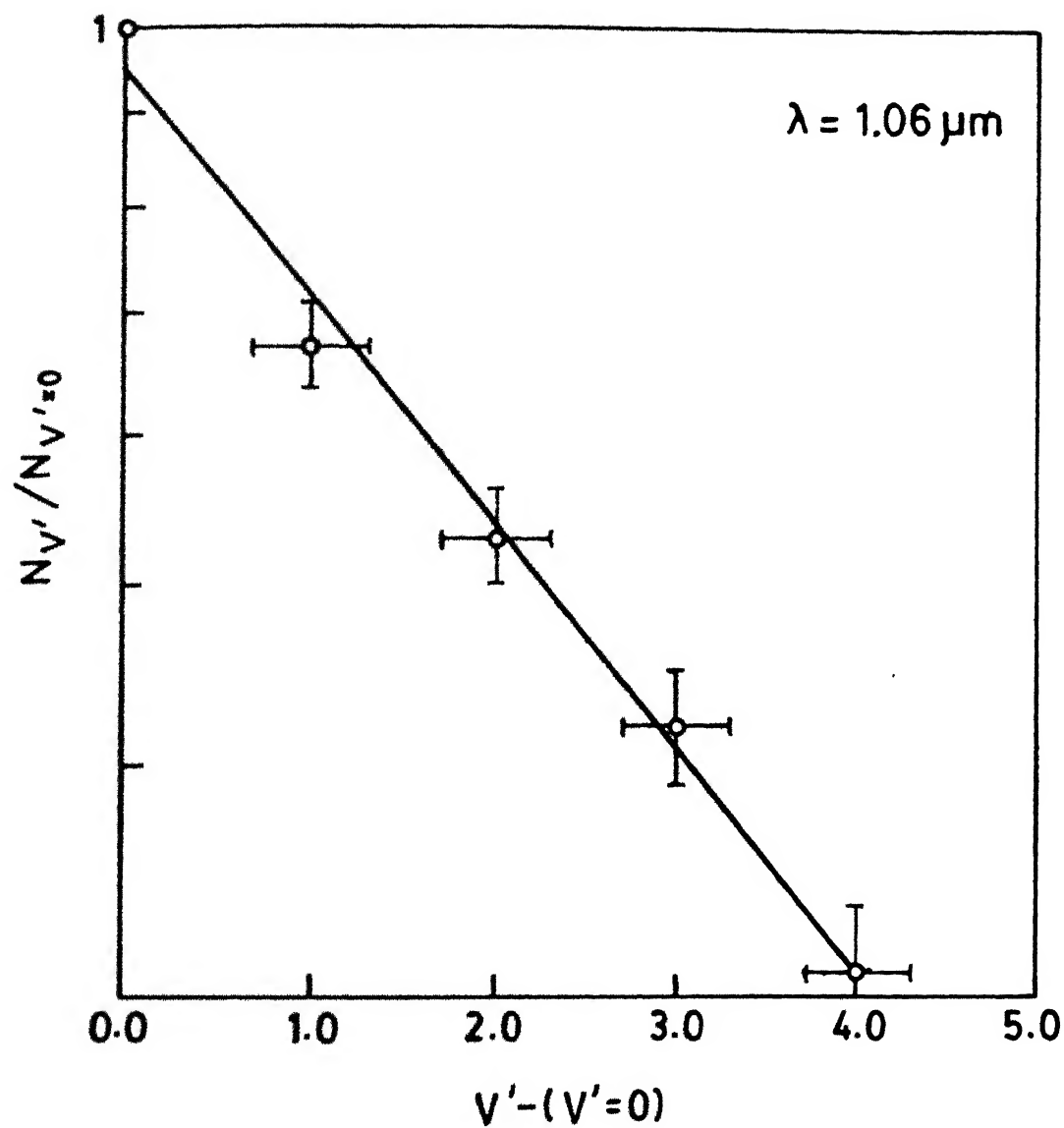
Fig. 38   Relative population of the upper vibrational level of the C_2
Swan band sequence $\Delta v = -1$ versus vibrational quantum number
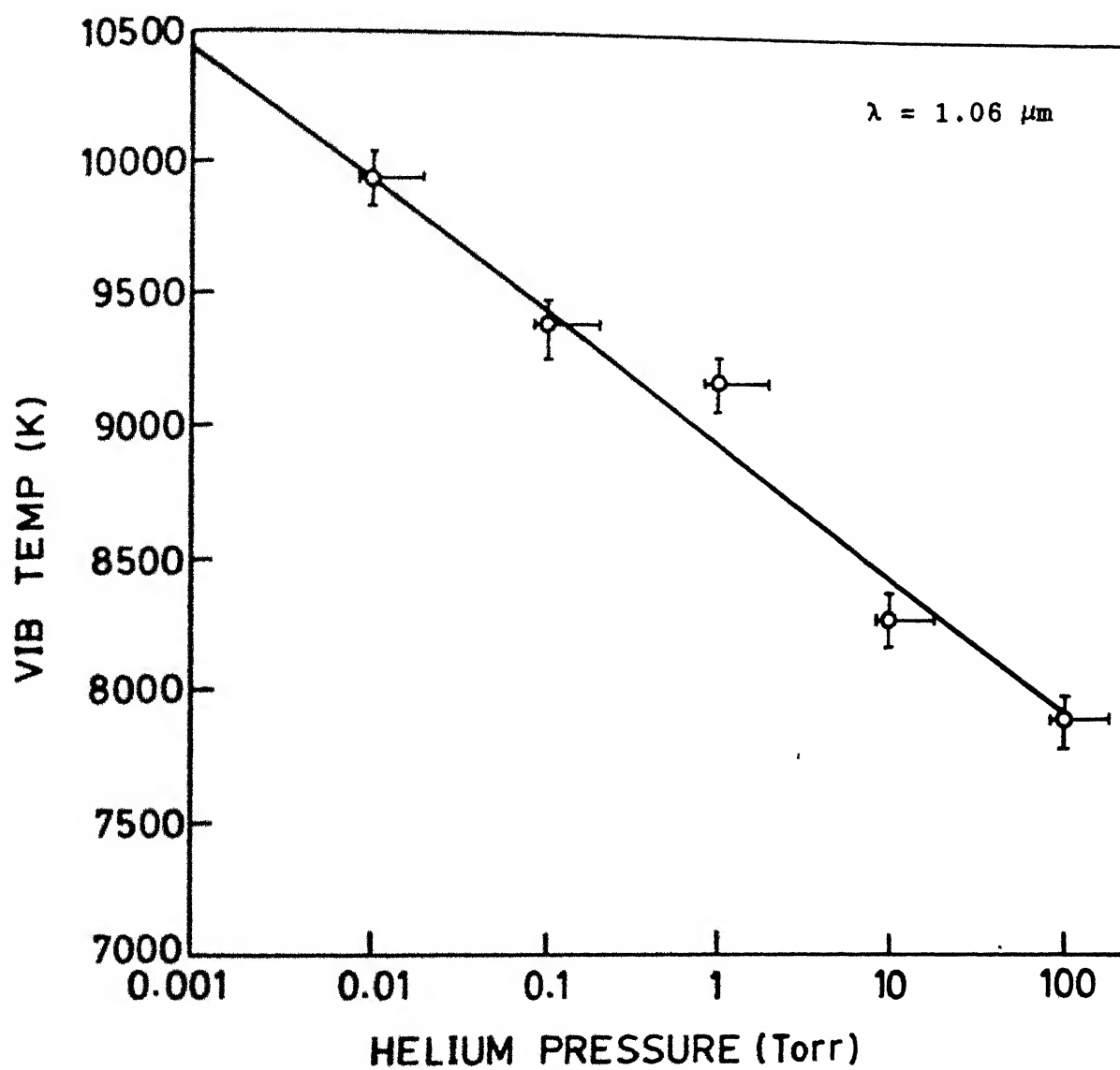
Fig. 39 Vibrational temperature calculated from C_2 Swan bands as a function of helium gas pressure.

increase in helium gas pressure. Hence the presence of helium gas helps in cooling of the molecular species and increases the recombination rate.

Wavelength Dependence

Relative abundance of clusters in the deposited film depends on parameters like laser wavelength, laser intensity and background gas etc.. Laser wavelength used for ablation plays an important role in defining the quality and sensitivity of the deposited film. It has been shown in pulsed laser deposition of high-T_c superconducting and of diamond like carbon films that short wavelengths (UV) and short pulse widths yield superior quality films.[137] To see the wavelength effect on C_2 species which dominate in diamond like carbon deposited films, emission spectra of C_2, d-a, $\Delta v = -1$ Swan band sequence[141] were taken in vacuum and in helium gas pressures[142] at various incident laser energies and wavelengths.[94] Figure 40 shows the intensity of C_2 Swan band heads of (v'-v'') i.e. (0-1) at 563.5 nm and (1-2) at 558.5 nm for 1.06 μm, 0.532 μm and 0.355 μm laser irradiation at 10^{-3} Torr pressure of helium gas. It is found that for all laser wavelengths there is an optimum energy after which intensity of the C_2 bands decreases. The intensity of C_2 bands peaks at 60 mJ, 40mJ and 30 mJ for 1.06 μm, 0.532 μm and 0.355 μm laser irradiation, respectively. Figure 41 shows the emission spectra of C_2 $\Delta v = -1$ Swan band sequence for 1.06 μm, 0.532 μm, 0.355 μm and 0.266 μm at the optimum energy at 10^{-3} Torr helium pressure. The intensity of the band heads slightly increases with the decrease in laser wavelength. This may be due to photofragmentation of higher clusters formed in laser produced plasma. Emission spectra of C_2 bands were recorded at the optimum laser energy for all laser wavelengths and for various helium gas pressures. Figure 42 shows the intensity of C_2 Swan band head of (v'-v'') i.e. (0-1) at 563.5 nm at various
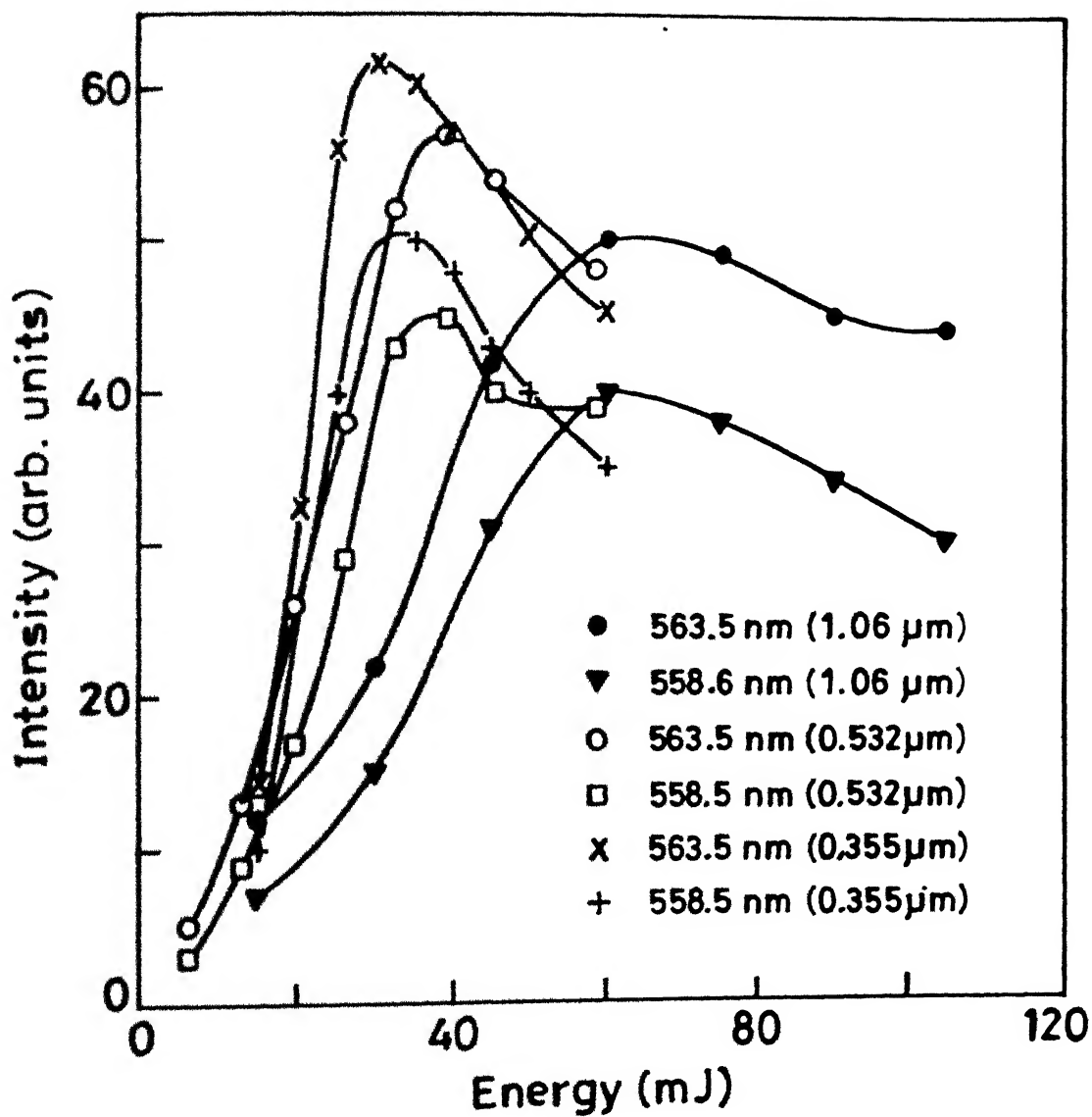
Fig. 40. Intensity of C_2 Swan band heads, (0-1) at 563.5 nm and (1-2) at 558.5 nm for 1.06 μm, 0.532 μm and 0.355 μm laser irradiation at 10^{-3} Torr helium pressure.
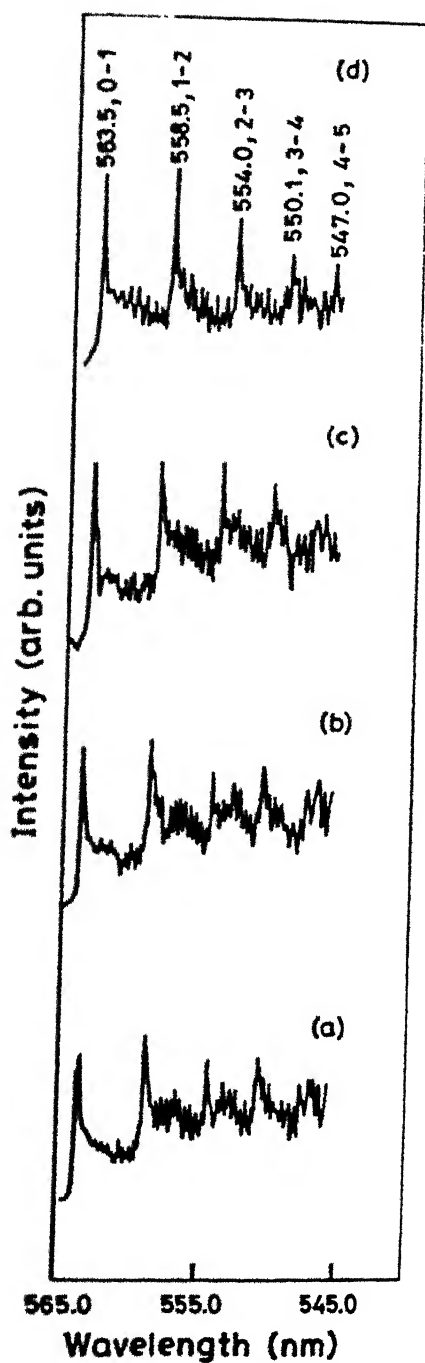
Fig. 41. C_2 $\Delta v = -1$ Swan band sequence at (a) 60 mJ for 1.06 μm, (b) 40 mJ for 0.532 μm, (c) 30 mJ for 0.355 μm and (d) 30 mJ for 0.266 μm laser irradiation at 10^{-3} Torr helium pressure.
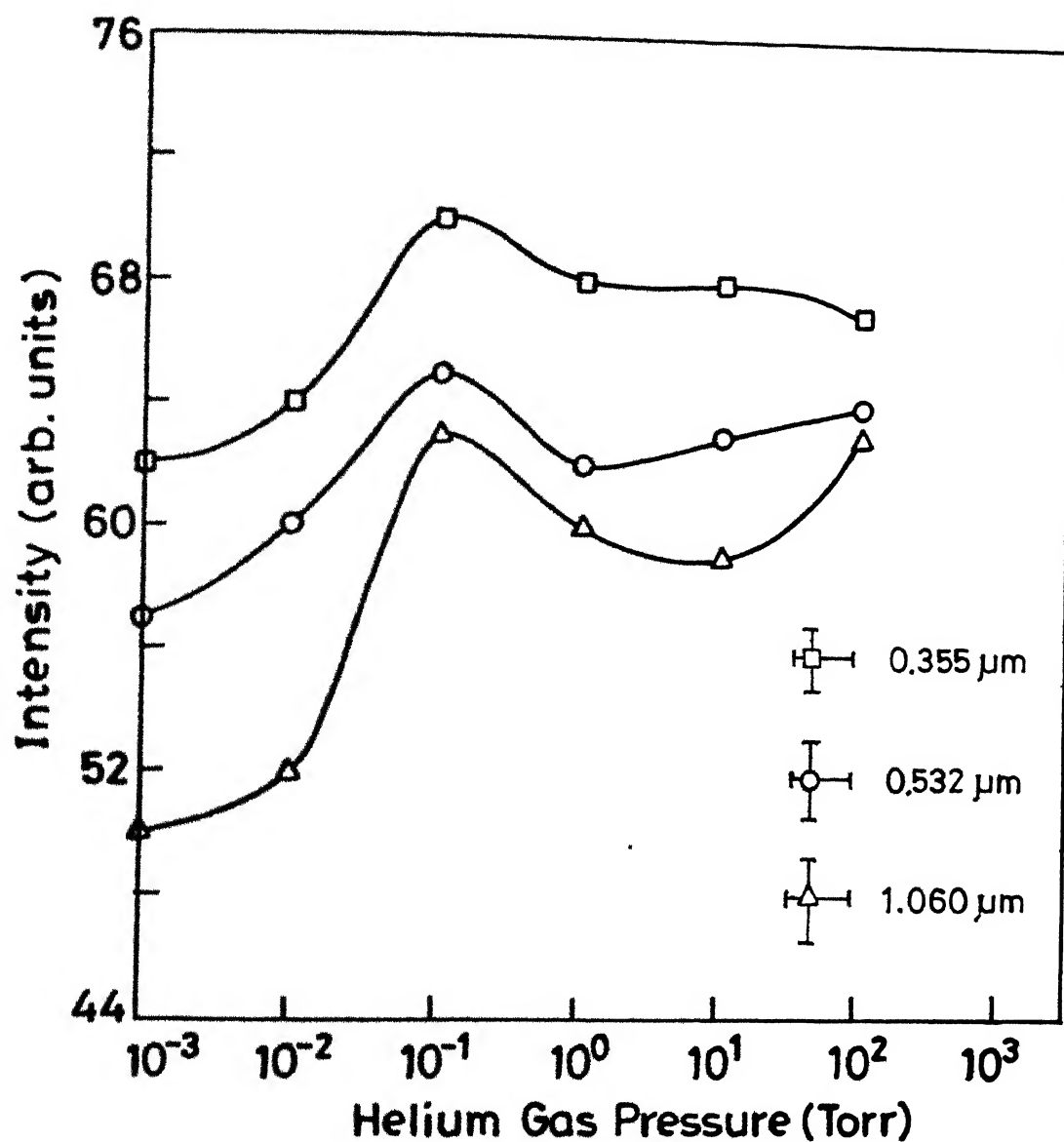
Fig. 42. Intensity of C_2 Swan band head (0-1) at 563.5 nm at various helium pressures for 1.06 μm, 0.532 μm and 0.355 μm laser irradiation.

gas pressures for 1.06 μm, 0.532 μm and 0.355 μm laser irradiation. With the increase in helium pressure, the intensity of C_2 band heads increases upto 10^{-1} Torr and does not change significantly upto 100 Torr. The vibrational temperature of C_2 bands was calculated for various laser wavelengths at various helium pressures. Figures 43(a) and (b) show the relative population of the upper vibrational level as derived from the measured intensities against vibrational quantum number for helium gas pressures from 10^{-3} Torr to 100 Torr for 0.532 μm laser radiation at 40 mJ laser energy and 0.355 μm laser radiation at 30 mJ laser energy, respectively. The slope of the curve gives vibrational temperature. Vibrational temperature was also calculated for 1.06 μm and 0.266 μm laser radiation. Figure 44 shows the variation of vibrational temperature at various pressures of helium gas for 1.06 μm at 60 mJ, 0.532 μm at 40 mJ, 0.355 μm at 30 mJ and 0.266 μm laser radiation at 30 mJ laser energy. The increase of helium pressure decreased the vibrational temperature for a particular laser wavelength. Thus addition of helium helps in cooling and clustering the molecular species. It follows from Fig. 44 that shorter laser wavelength irradiation produces higher vibrational temperature consistent with $T \approx (I\lambda^2)^{4/9}$.[1] Here I is the laser intensity and λ is laser wavelength. It has been found that using shorter wavelength laser irradiation high quality thin films can be deposited due to larger mass ablation rate $\dot{m}$ and surface absorption rate K.[143] $\dot{m}$ and K are defined as

$$\dot{m} \propto I^{5/9} \lambda^{-4/9} \tag{35}$$

$$K = \frac{4\pi\mu}{\lambda} \tag{36}$$

Here μ is the surface absorption index.[66,144] Experimental results[145,146] have
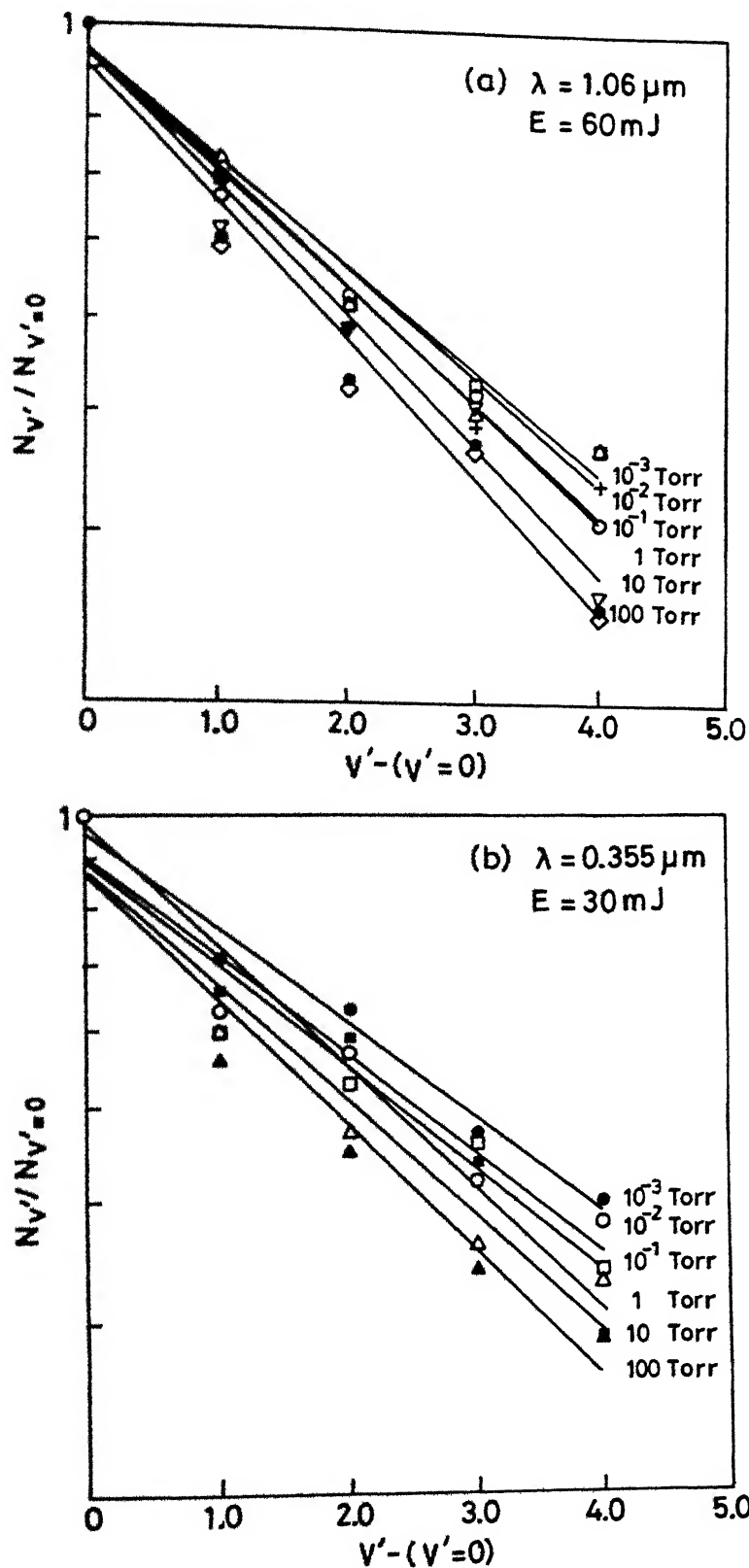
**Fig. 43. Relative** population of the upper vibrational level of the C_2 Swan band sequence $\Delta v = -1$ versus vibrational quantum number for helium gas pressures from 10^{-3} to 100 Torr for (a) 1.06 μm laser irradiation at 60 mJ laser energy and (b) 0.355 μm laser irradiation at 30 mJ laser energy.
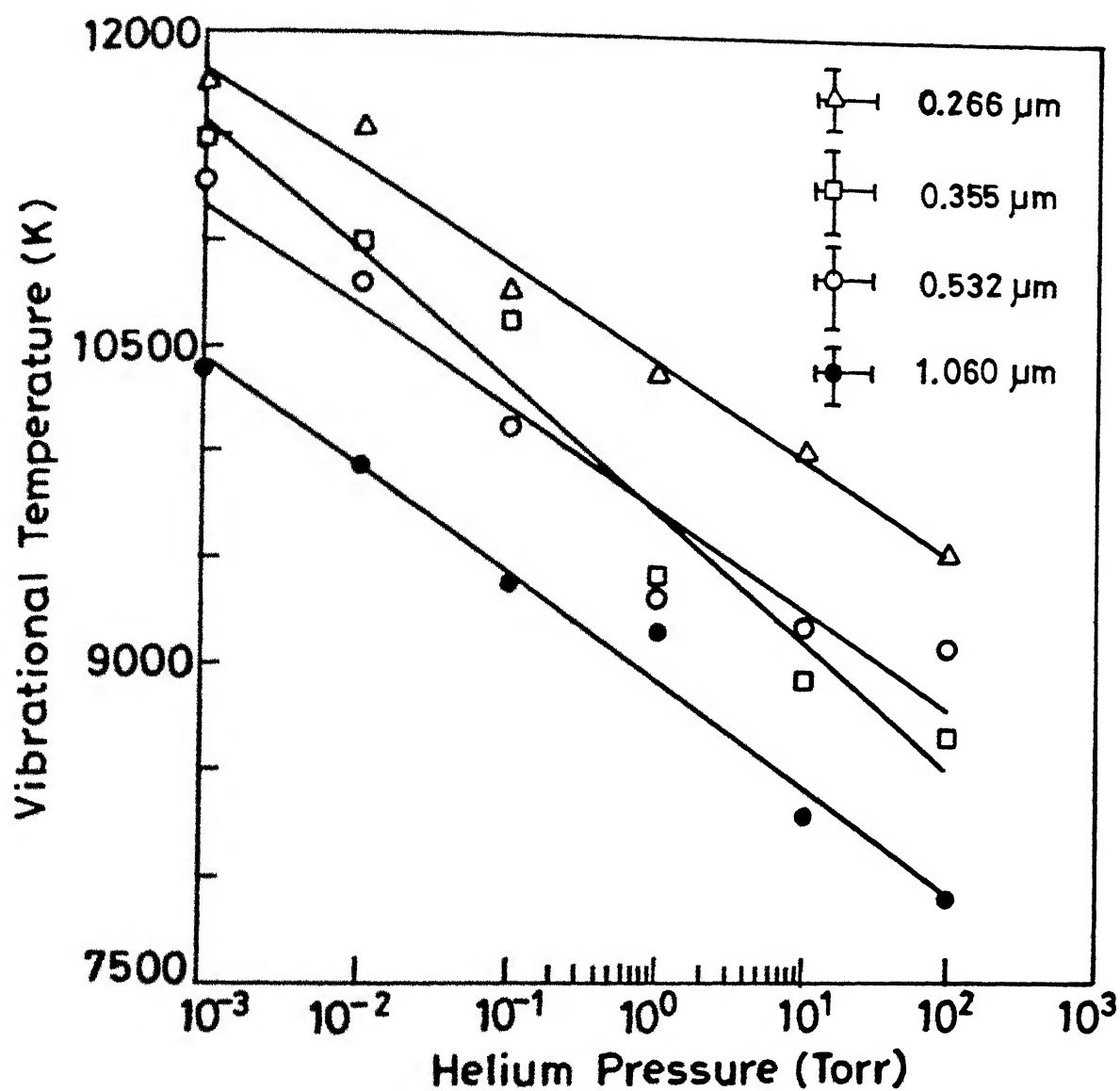
Fig. 44. Variation of vibrational temperature with helium pressures
for 1.06 μm at 60 mJ, 0.532 μm at 40 mJ, 0.355 μm at 30 mJ
and 0.266 μm laser irradiation at 30 mJ laser energy.

also shown that higher sensitivity of the deposited film is obtained using UV laser irradiation. Presumably, higher vibrational temperature for shorter wavelength may be due to a change in the optical penetration depth which decreases with wavelength. The decreased volume of material with which the laser can interact results in a more efficient coupling to the target. Hence shorter wavelength is to be preferred for thin film deposition. Koren et al[137] have shown that UV lasers deposited superconducting thin film result in lower resistivity. Figure 45 shows the vibrational temperature calculated at various laser energies for 0.355 μm at 10^{-1} Torr helium pressure. It follows that there exists an optimum laser energy at which vibrational temperature is maximum. The optimum films of diamond like carbon are obtained due to the condensation of energetic C_2 particles[17,57] only above a critical power densities of ~ 10^8 W/cm^2 and upto the densities where C_2 remains dominant fragment in the laser ablated carbon plasma. We observed the C_2 emission at power density slightly greater than the critical power density. It is also found that the degree of the diamond like character varies due to different temperature in the laser plasma,[12,50,57] hence deposition at the optimum energy where temperature obtained is maximum can play an important role for a thin film. The reported vibrational temperature of C_2 species for four order of magnitude of helium gas pressure may be helpful in understanding the phenomenon of deposition of diamond like carbon films.

To see the influence of background gas on temporal profiles of molecular carbon species, temporal profiles of C_2 d-a, 0-0 Swan band head at 516.5 nm being most prominent were recorded at various helium gas pressures at 2 mm from the target. Figure 46 shows the temporal profiles of C_2 band head at 516.5 nm at different helium gas pressures using 1.06 μm laser irradiation. It
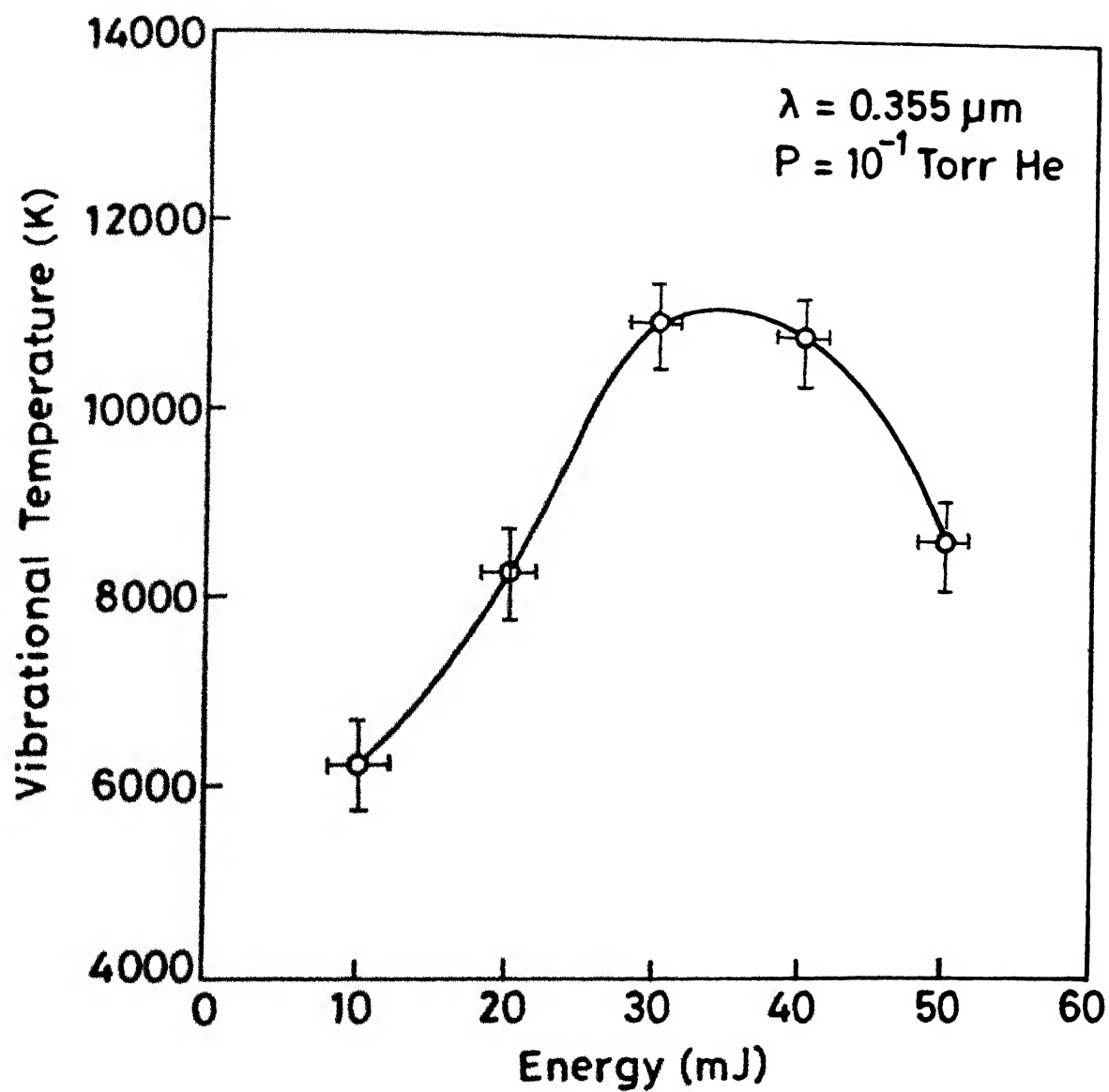
Fig. 45. Vibrational temperature as a function of laser energy for 0.355 μm at 10^{-1} Torr helium pressure.
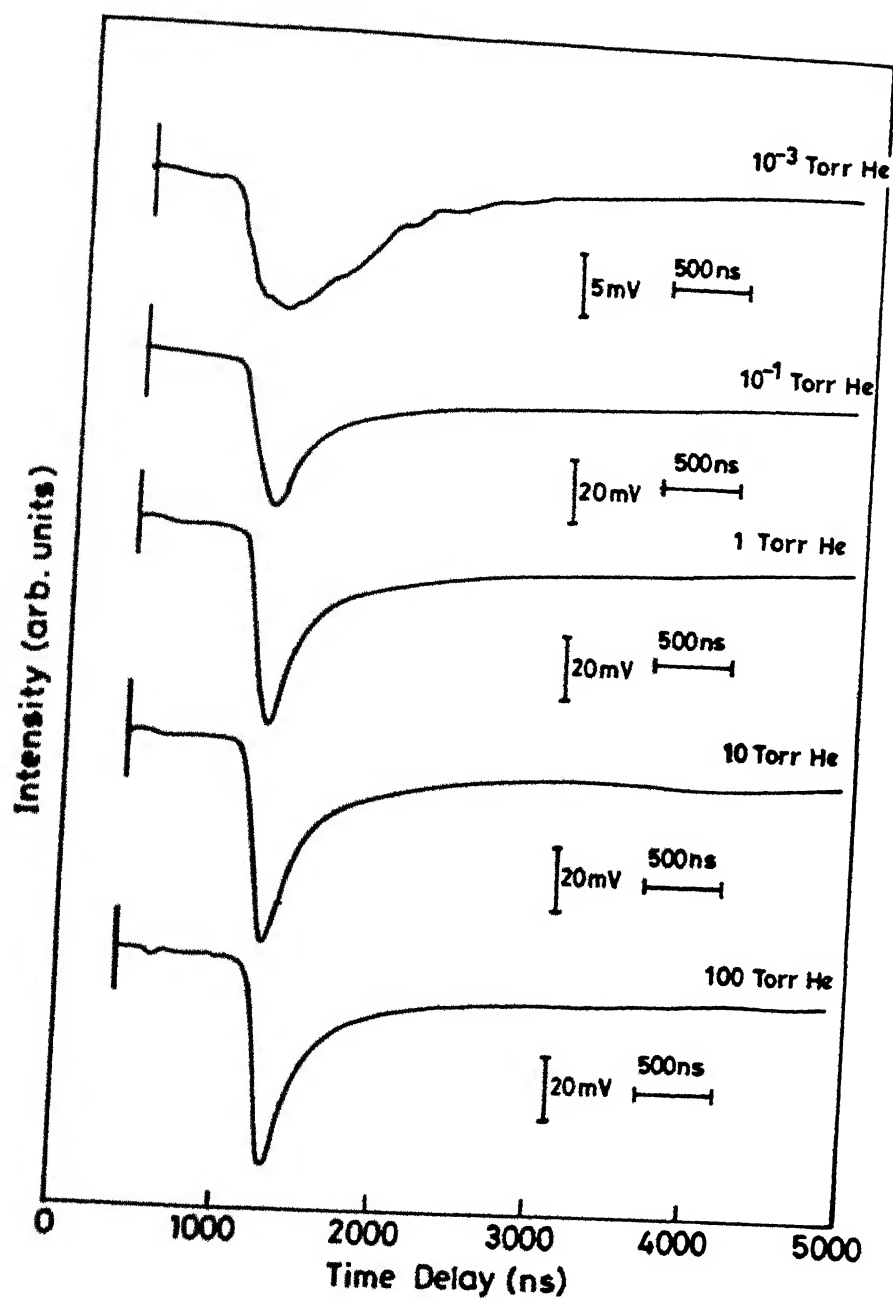
Fig. 46. Temporal profiles of C_2 band head at 516.5 nm at different helium pressures for 1.06 μm laser irradiation.

Is observed that increasing the helium gas pressure increased the delay time in the peak intensities of the temporal profiles. Thus velocity of the C_2 species decreased with the increase in pressure. The temporal profiles also showed the increase in intensity of band head with the increase in helium pressure.

In conclusion, C_2 emission spectra were recorded at various helium gas pressures at various incident laser energies and wavelengths. It is found that there is an optimum energy at which intensity of C_2 band heads is maximum. The presence of helium enhances the intensity of emitted C_2 spectrum. Vibrational temperature was calculated at various energies, wavelengths and helium pressures using Swan band head intensity. Temperature and velocity of the C_2 species decrease with the increase in helium pressure. Vibrational temperature increases with the decrease in laser wavelength and there is an optimum energy at which temperature is maximum.

CHAPTER V

FULLERENES FROM LASER ABLATED CARBON PLASMA

INTRODUCTION

Since the first report on the existence of stable carbon clusters of 60 atoms from a laser ablated graphite target,[69] there has been a tremendous growth in research activity aimed at understanding the formation and properties of clusters.[74,147] Clusters are of technological importance in diverse areas such as catalysis and combustion.[55] Experimental techniques have been developed to generate clusters of virtually any element from ablation of solid targets of the element in the gaseous atmosphere.[13-16] The early work involving carbon vaporized from graphite[148] has recently been supplemented by pulsed laser evaporation[149] and the formation of carbon clusters have been extensively studied.[150] Particularly, because of anticipated astrophysical significance, the carbon clusters are being generated and studied in the laboratory.[151] The carbon clusters which form closed structures known as fullerenes are of current interest because of their immediate applications in superconductivity and non-linear optics.[152,153] Two widely used methods for the preparation of such clusters are resistive heating and laser evaporation. In both these methods, C_{60} clusters are observed to be dominant when formed in the atmosphere of helium gas. However, the actual mechanism involved in the formation of fullerenes and the role of the background gas (like helium) which enhances the formation of carbon clusters, C_{60} etc., are not very clear.[147-153] In an attempt to generate these molecules in the laboratory, Kroto and coworkers[69,154] conducted a series of experiments in which they identified various even-numbered carbon species-fullerenes[13] in the products of laser vaporized graphite. It is found that two groups of

carbon clusters, i.e. C_n (n = 1 to 30) and C_{2n} (n = 20 to 90), are formed from laser evaporated carbon targets, the most stable being 60 carbon atom cluster and also a 70 carbon atom cluster to some extent.[13] The recent report on the production of macroscopic quantities of C_{60} (and also C_{70}) by Kratschmer et al[73] from laser evaporation has generated immense interest in carbon clusters. Study of C_{60} and C_{70} has received further impetus because of the discovery of conductivity[155] in alkali metal doped C_{60} and C_{70} and superconductivity[156] in C_{60} doped with K (T_c = 18 K), R_b (T_c = 28 K), and their alloys.[157] Wagal et al[158] have reported optical quality carbon film deposition by accelerating the ions produced in the laser produced plasma plume. Recently a systematic study of the structure of carbon fullerenes ranging from C_{72} to C_{102} has been carried out.[159] The relative abundance of these clusters critically depends on the experimental parameters like laser intensity, background gas, etc.. Mainly, C_{60} and C_{70} clusters dominate in the fullerene family when formed from low intensity plasma and/or at helium/argon pressure.[147] However, the correlation of carbon clusters[95,131] with the plasma dynamics is rare, particularly the dynamics of cluster formation is still not well understood.

Laser ablated carbon plasma in the presence of argon gas has been used for deposition of C_{60} on various substrates using pulsed laser deposition (PLD) technique.[74] PLD is emerging as the leading technique to deposit in situ high quality thin films because of its ability of giving high deposition rates, depositing materials with high melting temperatures, simplicity of implementation and operation, easy control of film microstructure and of maintaining stoichiometry of multicomponent system.[8-10] In the PLD process a mixture of plasma and hot vapours of the target material is produced and the properties of laser ablated plasma controls the growth, structure and

properties of produced thin films. High density gas flowing over the target serves as a buffer gas in which clusters of the target material are formed. Ambient gas effectively enhances the possibility for clustering and growth reactions.[147] Thus pulsed laser ablation consists of consecutive processes of energy coupling to the target material and deposition on substrate via the gas phase condensation. The presence of atomically and electronically excited (as well as ionized) species and fast quenching of the laser ablated plasma lead to the formation of films in metastable states with unique physical and mechanical properties.[160] The laser ablation and deposition technique has been used to produce a variety of films: high quality, high transition temperature superconducting oxide films;[161,162] hard, hydrogen-free diamond-like carbon films;[163] amorphous Si films;[164] and epitaxial TiN films from TiN targets,[165] and other films of Ge, SiO_2, GeO_2, Au, Cu, etc.. Recently extremely smooth high-quality C_{60} thin films were fabricated by irradiation of a pulsed KrF excimer laser beam on to a C_{60} powder target.[166] Creasy et al[167] have observed fullerene ions from laser ablation of diamond-like carbon films demonstrating that C_{60} ions can be formed in a variety of systems. Formation mechanism of the C_{60} films was found to be consistent with gas phase condensation of small species in the laser ablation plasma on to the substrate. The usual methods to characterize carbon soot and films are mass spectrometry, X-ray diffraction, UV-visible, IR and Raman spectra, scanning and tunneling electron microscopy, HPLC etc.. Yoshimoto et al[166] characterized the C_{60} films using Raman and UV-visible spectra and HPLC analysis. Takahashi et al[168] have used scanning electron microscopy and other techniques for characterization of plasma polymerized C_{60} / C_{70} mixture films. Many researchers have used field ion-scanning tunneling microscopy to study the monolayer and multilayer

adsorption behaviours of the C_{60} fullerene on Si (111)[169] and (100)[170] and Cu (111)[171] surfaces. Characterization of deposited films along with spectroscopic studies of the plasma plume can yield important information on the PLD process and also lead to a better understanding of the laser ablated plasma.

In this chapter presence of fullerenes[95] in laser ablated carbon soot and carbon films obtained from vaporization of graphite in a helium atmosphere and its correlation with the molecular carbon are discussed. X-ray, UV-visible absorption, infrared spectroscopy and scanning electron microscopy were used to characterize clusters.

EXPERIMENTAL SET UP

The carbon clusters were generated by ablation of graphite using a Q-switched Nd:YAG laser in a helium atmosphere. Experimental set up used in the present study is similar to the one described in Chapter II. Laser beam was focussed onto the rotating graphite target enclosed in a vacuum chamber. The experiment was carried out for different pressures in the range 10^{-2}-100 Torr of helium gas. Figure 12 shows the experimental set up used for the deposition of the carbon films. Q-switched Nd:YAG laser delivering upto 500 mJ of energy in 6 ns (FWHM) at its 2nd harmonic i.e. 0.532 μm with a repetition rate of 10 pps was line focussed using a cylindrical lens of focal length 30 cm to a spot of 0.048 cm^2 onto the rotating graphite rod. The ablated carbon was deposited on silicon and glass substrates at 1 cm away and parallel to the target surface at low laser irradiance. To observe the carbon clusters, 'soot', the ablated carbon powder was collected from the chamber at different helium pressures. Soot was dissolved in benzene / n-hexane solution and the

solution was heated tô 60°C for about 48 hours with constant stirring. The solution was filtered and the solvent evaporated in a flask till a thick solution (of about 2-3 ml) at the bottom was formed. This solution was decanted into a smaller sample tube and allowed to evaporate in ambient conditions. Micro crystals formed were dried and mixed with KBr to prepare pellets to record IR spectra. The n-hexane / benzene soluble material was characterized by UV-visible spectroscopy. Under the similar conditions of deposition of the carbon films, the plasma radiation was imaged on the monochromator and was detected with a photomultiplier tube and recorded on a strip chart recorder or displayed on the oscilloscope to study C_2 emission.[46,93,94]

RESULTS AND DISCUSSION

The experimental techniques used to characterize and study the carbon clusters mainly fullerenes are given in Table 2. Characterization of the carbon films[95] was done by X-ray diffraction and scanning electron microscopy. UV-visible and IR spectroscopy were used to characterize[73,108] fullerenes from laser ablated carbon soot.

Characterization of Pulsed Laser Deposited Carbon Films

X-Ray Diffraction and Scanning Electron Microscopy

The structural properties of the deposited carbon films were investigated by X-ray diffractometer (Rich & Seifert, JSO-debyeflex 2002) in order to determine crystalline orientation. Figure 47 shows a typical X-ray diffraction pattern of the carbon film deposited on silicon substrate at 100 Torr helium pressure. Peaks at 10.3°, 11°, 17.9° and 21° show the presence of
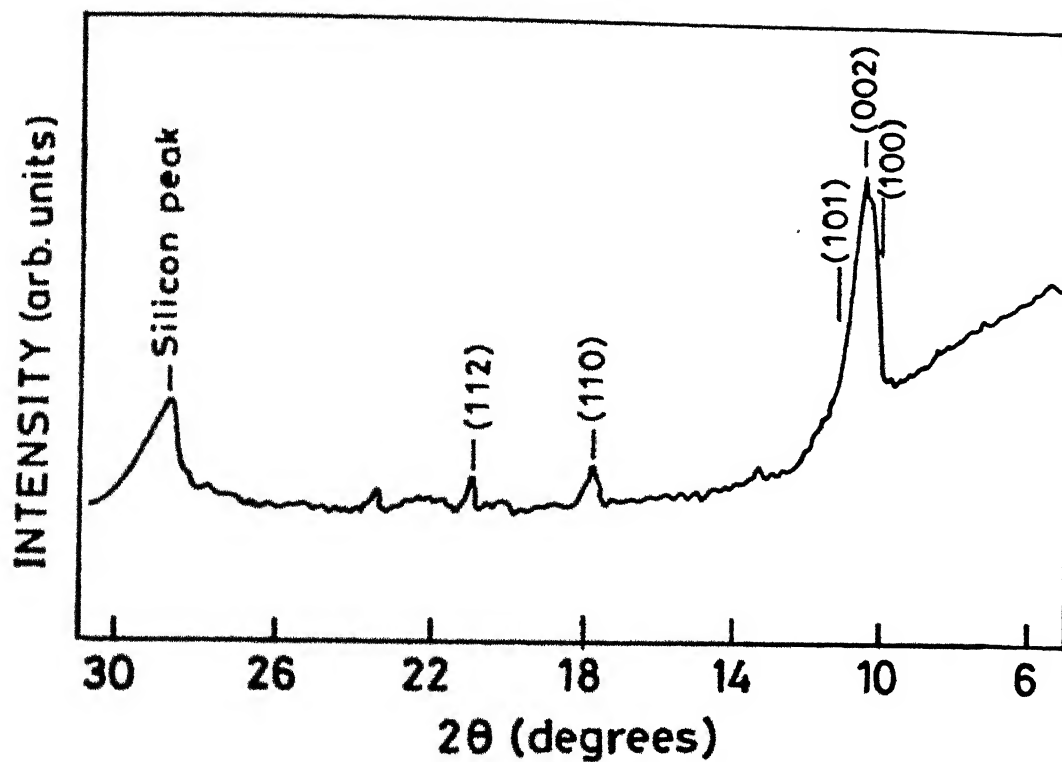
Fig. 47 X-ray diffraction pattern of the carbon film deposited at 100 Torr helium gas pressure. Peaks at $10.3°$, $11°$, $17.9°$ and $21°$ show the presence of (100), (002), (110) and (112) crystalline planes of C_{60}, respectively.

(100), (002), (110) and (112) crystalline planes of C_{60}, respectively. X-ray diffraction was also done for the carbon films deposited at various helium pressures from 10^{-2}-100 Torr and it was found that the observed peaks were prominent only at 100 Torr. This implies that the crystallinity changes with the helium gas pressures. At lower helium pressures (< 100 Torr) the films were amorphous. Increase in helium pressure upto 100 Torr improves the quality of the film crystallization and phase orientation.

Scanning electron microscopy was used to study the variation in the surface structure of the deposited carbon films with helium gas pressures. Films grown at various helium pressures exhibited marked differences in the composition and morphology of the films. Figure 48 shows the scanning electron micrographs (SEM) of the films deposited at 10^{-2}, 1, 10 and 100 Torr of helium gas pressure. It is found that the density of the microcrystalline clusters increases with the increase in helium pressure, this complements the observed X-ray peaks. Films deposited at lower helium pressures indicate low film density and poor connection between the clusters. Clusters become larger and more closely packed with the increase in helium pressure. At 100 Torr helium pressure, the nucleation density of carbon clusters in terms of surface area is about 80-90% of the total substrate surface. Beyond 100 Torr, carbon film starts peeling off and show cauliflower morphology with no systematic pattern. This variation in the morphology of the films is principally due to the temperature variations in the laser ablated carbon plasma at various helium pressures. Fig 49(a) and (b) show the individual microcrystals obtained at 100 Torr helium pressure and in vacuum, respectively. It is found that in vacuum the assemblage of hexagonal crystals is dominated whereas in the presence of helium gas particularly at 100 Torr spherical aggregates of carbon are
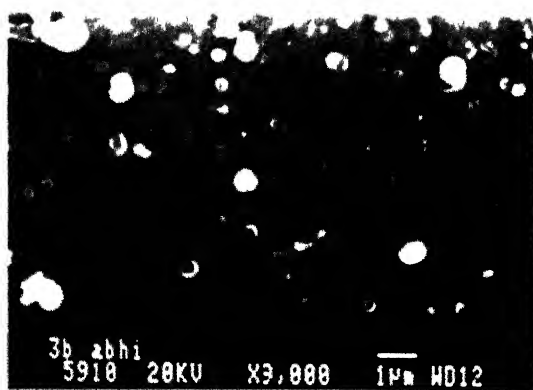
(a)
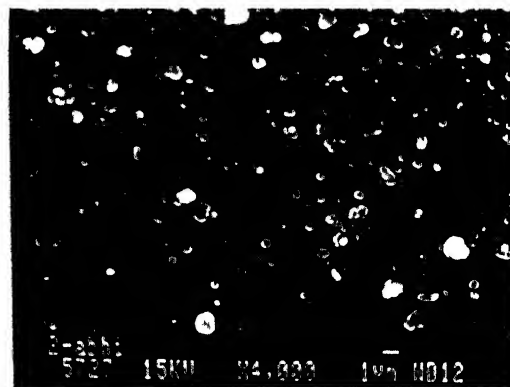
(b)
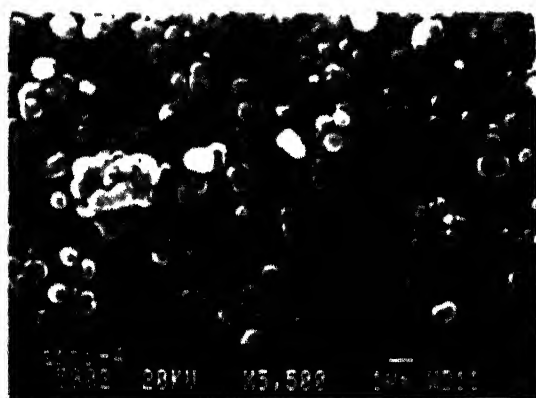
(c)
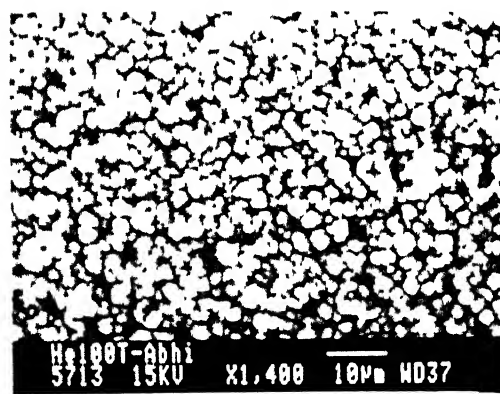
(d)

Fig. 48   Scanning electron micrographs of the carbon films deposited
at (a) 10^{-2}, (b) 1, (c) 10 and (d) 100 Torr of helium gas
pressure.

(a)
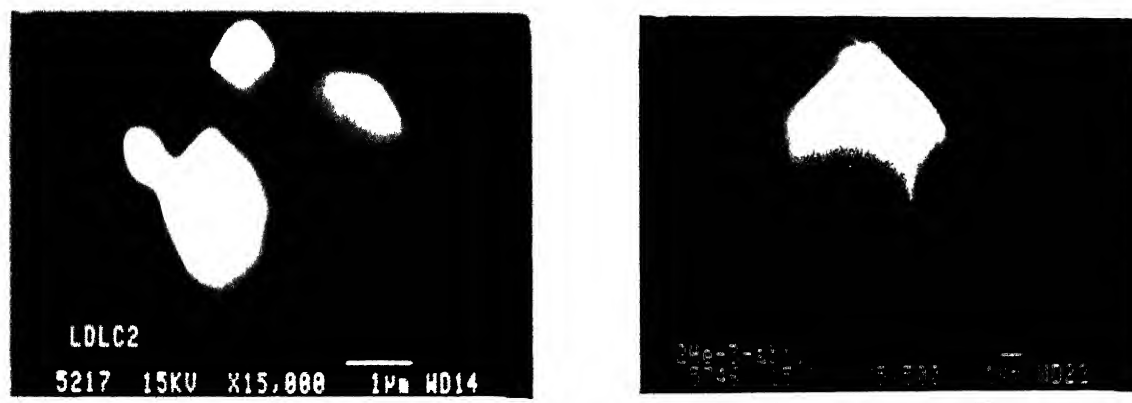
(b)

Fig. 49   Scanning   electron   micrographs   of   the   individual
microcrystals obtained at (a) 100 Torr helium pressure and
(b) in vacuum.

dominant. This structure at 100 Torr agrees well with the reported structure of C_{60}.[109]

Laser Ablated Carbon 'Soot' Characterization

UV-Visible Absorption and Infrared Spectroscopy

Figure 50 shows an optical absorption spectrum recorded at room temperature in the range 200-450 nm of the carbon soot (collected at 100 Torr helium pressure) dissolved in n-hexane. The absorption spectra show peaks around 211, 231, 273, 299, and a broad band at 325 nm. These peaks are characteristic of C_{60} and C_{70} clusters.[172] The fact that these peaks exist indicate the presence of fullerenes in our soot. The peak at 231 nm appears as a shoulder to 211 nm. However, in pure C_{60} these two peaks are well separated.[73]

The benzene dissolvable fullerenes were further characterized by using vibrational spectroscopy. Raman spectral studies on deposited films showed peaks at 1362, 1587 cm^{-1}. The relative intensity of these peaks increase at some spots in the films, indicating the existence of crystalline domains. Since these domains were very few and tiny, we resorted to the method of extracting fullerenes by dissolving the 'soot' in benzene and depositing the aliquots of the benzene extract onto KBr pellets for IR spectroscopy. No attempt was made to separate the clusters as the yield of the benzene soluble clusters was very low, thus the overlapping of many bands in the IR spectra is expected. Figure 51 shows IR spectra recorded at 10^{-2}, 1, and 100 Torr helium gas pressures. The modes at 1720, 1600, 1580, 1455, 1383, 1269, 1126, 1068, 1039, 739, 701, 670, 651, 575 and 525 cm^{-1} were observed. It is evident from the IR spectra, Fig. 51, that the modes become prominent as the helium gas
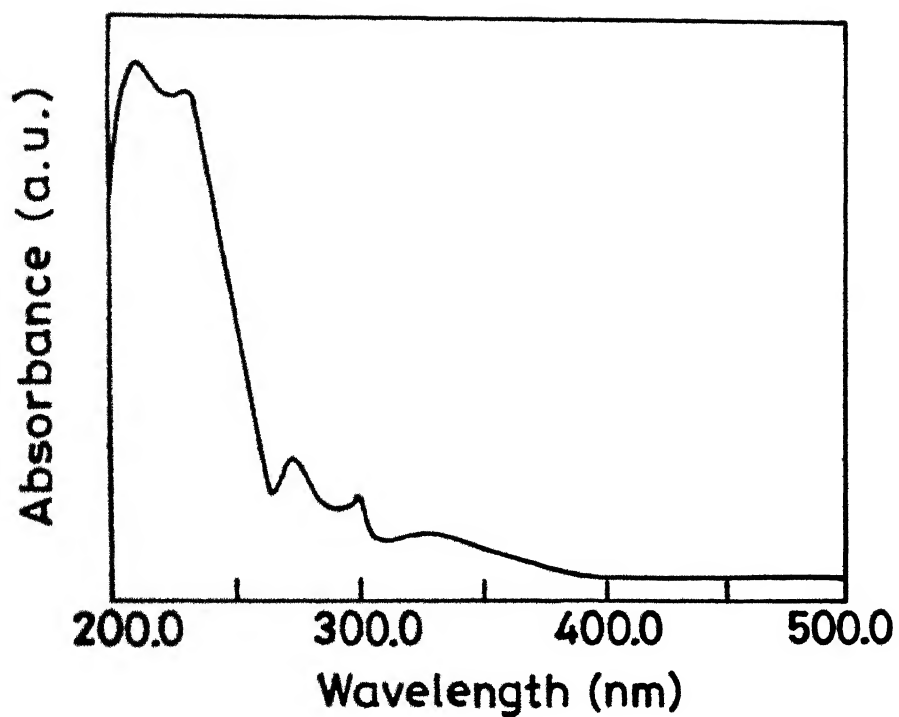
Fig. 50 Optical absorption spectrum from the n-hexane solvable soot
collected at 100 Torr helium pressure in the range 200-450 nm.
Peaks around 211, 231, 273, 299 and a broad band at 325 nm
are characteristic of C_{60} and C_{70} clusters.
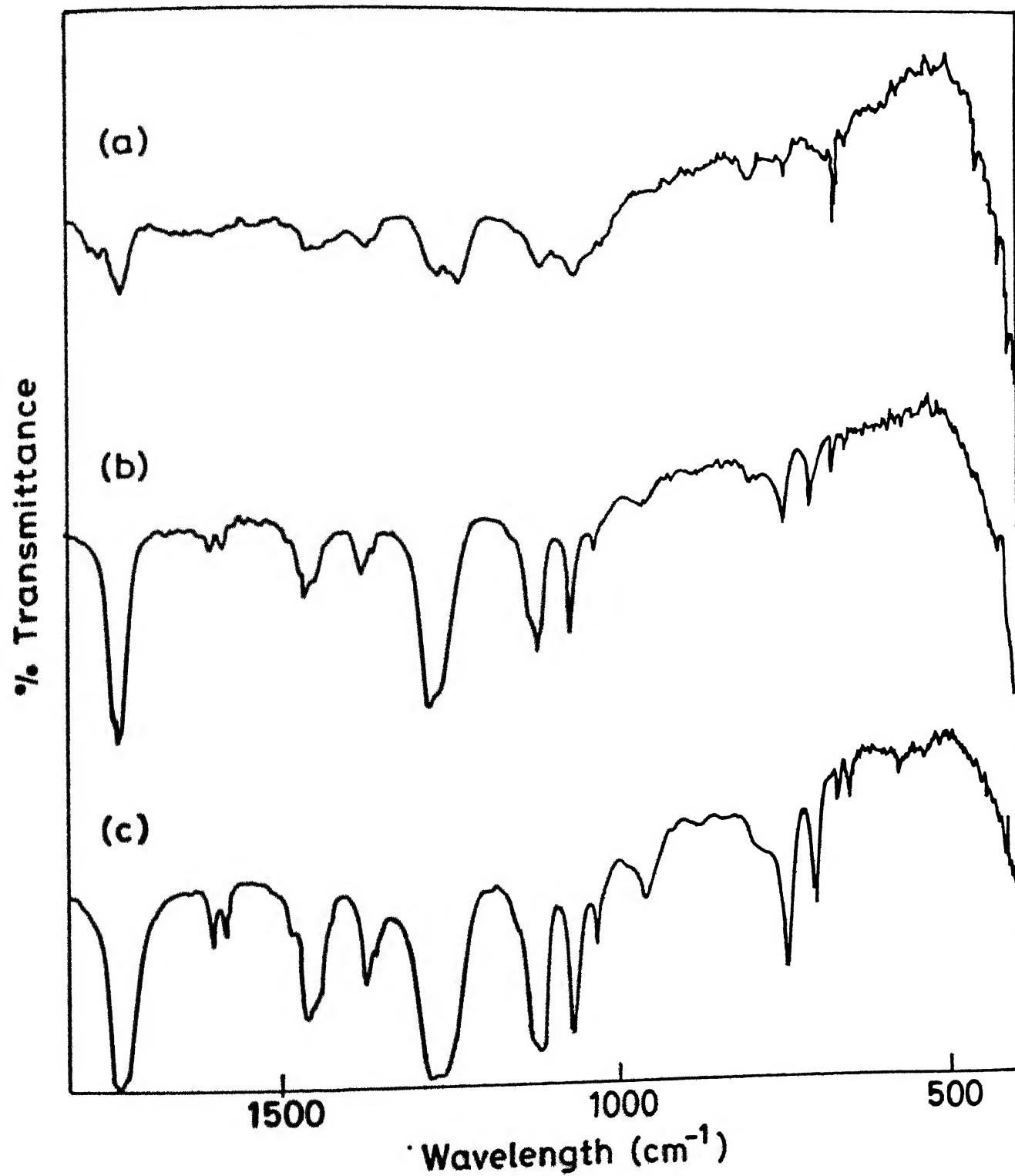
Fig. 51 Infrared spectra of carbon clusters extracted from benzene solvable soot collected at (a) 10^{-2}, (b) 1 and (c) 100 Torr helium pressure. The modes corresponding to 1455, 1126, 739, 701, 670, 651, 575 and 525 cm^{-1} show the presence of C_{60} and C_{70}.

pressure is increased from 10^{-2} to 100 Torr. The observed bands were identified by comparison with known modes.[73] Generally C_{60} in the solid phase shows four characteristic IR active modes at 527, 577, 1183 and 1429 cm^{-1}, though the agreement between experimental observation and theoretical calculation is very poor.[173,174] IR spectra of C_{70} comprises of modes at 458, 536, 570, 650, 674, 700, 730, 830, 1180 and 1430 cm^{-1}. On comparing the observed modes with the modes of C_{60} and C_{70}, it is found that the modes corresponding to 1455, 1126, 739, 701, 670, 651, 575 and 525 cm^{-1} could be due to C_{60} and C_{70}. The highest frequency IR mode for C_{60} and C_{70} is around 1430 cm^{-1}. The peak at 1455 cm^{-1}, in our case, could be due to C_{60} and C_{70}. Again there is a strong overlap for 1180 cm^{-1} (next highest) for C_{60} and C_{70} which we observe at 1269 cm^{-1}. Usually it is difficult to compare the low frequency spectra as the overlap of all fullerenes is stronger, and results in a broad structure. However, clear modes at 651, 670, 701 and 739 cm^{-1} are observed indicating the presence of C_{70} clusters. The two lower frequency modes of C_{60} are not very much evident at lower helium pressures in the spectra, but appear at 100 Torr helium pressure. The mode at 1039 cm^{-1} could well be compared with the recent calculations which predict additional modes at 159 and 1066 cm^{-1}.[175] The observations indicate the presence of C_{60} and C_{70} microcrystalline domains in our soot. It is interesting to note the existence of a strong mode at 1720 cm^{-1} in the IR spectra. This mode indicates the presence of higher fullerenes. A primary evidence of these came from the absorption spectra of the soot collected in vacuum (Fig. 52). The absorption spectra show peaks around 277, 298, 323 and a broad band at 367 nm. These absorption peaks and strong mode at 1720 cm^{-1} in the IR spectrum show the presence of carbon clusters C_{78}, C_{80}, C_{82} and C_{84}. But the clusters of C_{78},
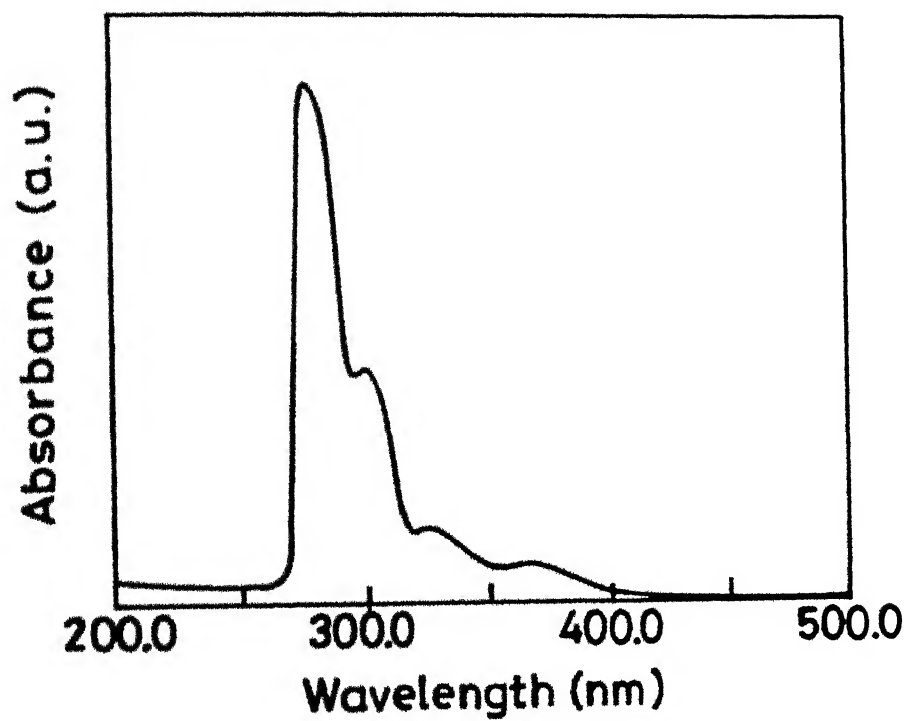
Fig. 52 Optical absorption spectrum from the benzene solvable soot collected in vacuum in the range 200-450 nm.

C_{80} and C_{82} are known to show a weak double peak structure in 700-800 nm range, which red shifts and weakens on increasing the size.[176,177] Whereas no such peak is known for C_{84} in this range. We have not observed any peak in 700-800 nm range in the absorption spectrum implying the absence or negligible presence of C_{78}, C_{80} and C_{82} clusters. Thus the mode at 1720 cm^{-1} in the IR spectra indicates the presence of higher cluster C_{84}. It is worthwhile to compare our results with recent calculations of vibrational frequencies of C_{84} molecule.[178] The calculations show two higher frequency modes at 1703 and 1683 cm^{-1} for C_{84} under D_2 symmetry. The strong mode at 1720 cm^{-1} could well be compared with 1703 cm^{-1}. The mode at 1683 cm^{-1} appears as a broad peak at 1625 cm^{-1}. These observations indicate the presence of C_{84} in our case.

Several reports explain the growth mechanism of fullerenes.[179] Kroto[76] and Smalley[180] proposed that the nucleus of the growing particles in an incomplete spherical shell accumulates primarily graphitic carbon on its reactive edges. A fullerene is formed in the rare event that a shell closes, thereby becoming inert with respect to further growth. Wakabayashi et al[77] proposed ring-stacking model following Kroto et al and showed that C_2 is the dominant fragment for the formation of the stable fullerenes as shown in Fig. 1 for the I_h symmetry and D_{5h} symmetry of C_{60} and C_{70} molecule, respectively and for perfect closing of fullerenes. An extensive spectroscopic study of ionic[79] and molecular species[46,94] was performed from laser ablated carbon plasma. It is found that at higher laser irradiance such as 900 mJ of laser energy the plasma emission is dominated by atomic/ionic species from C V to C I and at low irradiance molecular C_2 emission was prominent. Moreover, in the presence of ambient gas significant enhancement for ionic, atomic and molecular species of carbon with the increase in gas pressure was observed.

Characterization of pulsed laser deposited carbon films and laser ablated carbon soot showed that the yeild of fullerenes was found to be maximum at higher helium pressures. We found that emission spectrum recorded under the conditions of deposited films consisted of C_2 Swan bands. Band head intensities of C_2 Swan bands at various pressures showed similar trend as was observed for fullerenes. It is known that characteristics of the film are effected by the energy of the particles being deposited and hence on the temperature of the dominant species. Therefore, in order to optimize the fullerene film characteristics we estimated the temperature of the C_2 species which dominate in laser ablated plume. The vibrational temperature calculations[94] for C_2 species at various helium pressures showed decrease in temperature with the increase in helium pressure. This indicates that the presence of helium gas helps in cooling and clustering of the species. Particularly at 100 Torr helium pressure, vibrational temperature was found to be lowest, indicating that clustering is maximum at 100 Torr pressure and hence explains the observance of fullerenes, in agreement with our SEM pictures at various pressures as shown in Fig. 48. X-ray spectra recorded for deposited films at various helium pressures showed that amorphous character was prominent at lower helium pressures but nearly at 100 Torr helium pressure crystalline peaks of C_{60} were observed. Similar to the increase in C_2 band heads increase in IR spectrum modes was observed with the increase in helium pressure showing that C_2 is the dominant species for the formation of fullerenes. Photodissociation experiments[181] have also shown that larger (n $\ge$ 32) even numbered cluster ions decay dominantly by the loss of a neutral C_2 fragment indicating the importance of C_2 in fullerenes.

To conclude, the carbon clusters C_{60}, C_{70} and C_{84} produced by laser

vaporization of a graphite in the presence of helium gas were characterized using X-ray diffraction, scanning electron microscopy, UV-visible absorption and infrared spectroscopy. Importance of molecular carbon C_2 in the formation of fullerenes is also discussed.

CONCLUSIONS

We studied the pulsed laser ablated carbon plasma in vacuum and in the presence of air, helium and argon gases at low and moderate laser irradiance. A Q-switched Nd:YAG laser and its harmonics were used to produce carbon plasma. Plasma emission was recorded at various distances from the target surface ($z = 0$-20 mm) for different laser energies (30 mJ to 1 J) and wavelengths (1.06, 0.532, 0.355 and 0.266 μm). Thin films of carbon were deposited on glass and silicon substrates.

At moderate laser intensities $\sim 10^9$-10^{12} W/cm^2, we found that atomic/ionic species (C I to C V) dominate the plasma emission. Electron temperature of the carbon plasma estimated from the relative intensities of spectral lines assuming the plasma to be in local thermodynamic equilibrium lies between 2-10 eV. The variation of electron temperature with intensity of laser radiation gives $I^{0.4}$ dependence. The electron density estimated by measuring the stark width of C II transition $3p\ ^2P^0 - 4s\ ^2S$ at 392.0 nm at various distances away from the target was found to be in the range 10^{16}-10^{17} cm^{-3}. The variation of stark broadened profile in the presence of helium and argon gases was also carried out. The temporal profiles of C II (426.7 nm), C III (465.0 nm) and C IV (580.1 nm) were used to estimate the velocity of the plasma front. The expansion velocities of C II, C III and C IV species were found to be about 4×10^6, 7×10^6 and 10×10^6 cm/s, respectively. Thus it decreases with decrease in ionic charge. Expansion velocity of the plasma front decreased with the increase in atomic mass and pressure of the ambient gas. Laser ablated carbon studies in the presence of helium and argon indicated the line emission enhancement of the ionic species. It was found

that the background gas essentially provides a heat sink and the three body recombination rate increased resulting in populating the excited neutral and ionic carbon species. A detailed investigation of the temporal profiles at various pressures of air, helium and argon gas and at different distances revealed a peculiar double peak structure in the temporal profile of the C II transition 3d ^{2}D - 4f ^{2}F^0 at 426.7 nm at various gas pressures. Various interaction processes such as electron-ion recombination, collisional interactions, blast/shock wave, micro-instabilities occurring due to interaction of laser plasma and the ambient gas etc. were investigated as a possible cause of the double peak structure. It is proposed that the second peak in temporal profiles originates mainly due to stratification of the plasma into fast and slow ion components at the interface region due to density fluctuations where the occurrence of the Rayleigh-Taylor instability caused deceleration of the laser plasma front. The instability occurred at 0.1 Torr of background gas.

At low laser irradiance the plasma emission was dominated by C_2 emission in the Δv = -2, -1, 0, +1, +2 sequences of the Swan (d$^3\Pi_g$ - a$^3\Pi_u$) bands and the Δv = 0 and +1 sequences of the Deslandres - d'Azambuja (C$^1\Pi_g$ - A$^1\Pi_g$) bands. C_2 being an essential ingredient for generation of stable C_{60} and C_{70} clusters and for deposition of diamond like carbon films, an extensive investigation of optical emission spectra of C_2 were carried out. The studies were performed at various laser irradiances, wavelengths and at various pressures (10^{-3} to 100 Torr) of the ambient gas. We found that at an optimum energy the intensity of C_2 band heads is maximum. The presence of helium gas enhanced the intensity of Swan band heads. Vibrational temperatures estimated from the measured emission intensities of the Swan band heads at

various laser energies and wavelengths and under various helium pressures lie in the range of 6000-12000 K. Temperature and velocity of the C_2 species decrease with the increase in helium pressure. Thus addition of helium helped in cooling and clustering of the molecular species. Vibrational temperature increases with the decrease in laser wavelength and there is an optimum energy at which temperature is maximum. The shorter laser wavelength irradiation produced higher vibrational temperature consistent with $T \approx (I\lambda)^{4/9}$.

Pulsed laser deposition was attempted for depositing carbon films on silicon substrates at 1 cm away and parallel to the target surface at low laser irradiance and at different helium pressures. X-ray diffraction pattern of the carbon films deposited at 100 Torr helium pressure showed peaks at $10.3°$, $11°$, $17.9°$ and $20°$ confirming the presence of (100), (002), (110) and (112) crystalline planes of C_{60}. Scanning electron micrographs of the film deposited under various helium pressures showed that the density of the microcrystalline clusters increases with the increase in helium pressure. Beyond 100 Torr, carbon film showed 'cauliflower' morphology with no systematic pattern. The ablated carbon powder 'soot' collected from the chamber at different helium pressures was analyzed for the presence of C_{60}. The optical absorption spectra show peaks around 211, 231, 273, 299 and a broad band at 325 nm which are characteristic of C_{60} and C_{70} clusters. Prominent IR modes at 1720, 1455, 1126, 739, 701, 670, 651, 575 and 525 cm^{-1} in the infrared spectrum showed the presence of C_{60}, C_{70} and C_{84} in the benzene/n-hexane solvable carbon soot.

Future scope of work

No attempt was made to understand the plasma expansion in the

presence of magnetic field However, in order to gain more understanding of the instabilities occurring in the laser ablated carbon plasma, a systematic study undertaken in the presence of magnetic field in an ambient gas atmosphere will enhance the growth of Rayleigh-Taylor instability near the magnetic confinement radius where the excluded field energy equals the original plasma energy. Development of the instability can be studied using high speed streak photography. These studies will help in simulating the space and astrophysical-like plasmas at moderate irradiances in laboratory. Astrophysical-like plasmas have usually been achieved at very high irradiances. Studies of various other phenomena like large larmour radius instability, jet effect, conditions of strongly coupled plasma at moderate laser intensity will help in understanding the plasmas in laboratory.

We measured the electron density using stark broadened profile of the C II species. Other methods like resonance absorption and laser-induced fluorescence can be utilized using tunable dye laser as a probe beam to compare the density.

We used pulsed laser deposition technique for depositing carbon films. However, to increase the yield and to improve the homogeneity and uniformity of the deposited film, the pulsed laser deposition along with capacitively coupled plasma technique can be tried. This technique involves coupling of laser energy to the laser ablated spot. It extends the laser ablated plume to a large area, large volume and deposits energetic species giving uniform film.

Due to presence of delocalised π-electrons, the fullerenes, C_{60}, C_{70} etc. have been predicted to exhibit nonlinear optical behaviour. Studies of nonlinear optical properties like optical limiting, phase conjugation of the C_{60} / C_{70} toluene solution, can be carried out.

REFERENCES

1. T.P. Hughes, *Plasmas and Laser Light* (Wiley, New York, (1975).

2. R.K. Singh and J. Narayan, Phys. Rev. B 41, 8843 (1990).

3. H. Puell, Z. Naturforsch 25a, 1807 (1970).

4. J.C. Miller and R.F. Haglund, Jr., *Laser Ablation*, (Springer, Berlin 1991).

5. J.F. Ready, *Effect of High Power Laser Radiation*, (Academic Press, New York, 1971).

6. K. Laqua, *Analytical Laser Spectroscopy*, N. Omenetto Ed., (Wiley, Interscience, New York, 1979).

7. K. Dittrich and R. Wennrich, Prog. Analyt. Atom. Spect. 7, 139 (1984).

8. C. Champeaux, P. Marchet, J. Aubreton, J.P. Mercurio and A. Catherinot, Appl. Surf. Sci. 69, 335 (1993).

9. J. Seth, R. Padiyath, D.H. Rasmussen and S.V. Babu, Appl. Phys. Lett. 63, 473 (1993).

10. E. Dyer and R.J. Farley, J. Appl. Phys. 74, 1442 (1993).

11. L.J. Radziemski and D.A. Cremers, Ed. *Laser Induced Plasmas and Applications*, (Marcel Dekker, Inc., New York, 1989).

12. D.L. Pappas, K.L. Saenger, J. Bruley, W. Krakow, J.J. Cuomo, T. Gu and R.W. Collions, J. Appl. Phys. 71, 5675 (1992).

13. E.A. Rohlfing, D.M. Cox, and A. Kaldor, J. Chem. Phys. 81, 3322 (1984).

14. U. Naher, H. Gohlich, T. Lange and T.P. Martin, Phys. Rev. Lett. 68, 3416 (1992).

15. R.E. Leuchtner, A.C. Harms and A.W. Castleman, Jr., J. Chem. Phys. 94, 1093 (1991).

16. D.E. Powers, S.G. Hansen, M.E. Geusic, D.L. Michalopopulos and R.E. Smalley, J. Chem. Phys. 78, 2866 (1983).

17. R.W. Dreyfus, R. Kelly, R.E. Walkup and R. Srinivasan, SPIE 710, 46 (1986).

18. B. Soom, H. Chen, Y. Fischer and D.D. Meyerhofer, J. Appl. Phys. 74, 5372 (1993).

19. G. Mehlman, D.B. Chrisey, P.G. Burkhalter, J.S. Horwitz and D.A. Newmann, J. Appl. Phys. 74, 53 (1993).

20. N.G. Utterback, S.P. Tang and J.F. Friichtenicht, Phys. Fluids 19, 900 (1976).

21. B.C. Boland, F.E. Irons and R.W.P. McWhirter, J. Phys. B 1, 1180 (1968).

22. F.E. Irons, R.W.P. McWhirter and N.J. Peacock, J. Phys. B 5, 1975 (1972).

23. J.F. Seely and W.B. McKnight, J. Appl. Phys. 48, 3691 (1977).

24. C. Steden and H.J. Kunze, Phys. Lett. A 151, 534 (1990).

25. F.E. Irons and N.J. Peacock, J. Phys. B. 7, 2084 (1974).

26. L.Z. Barabash, Yu.A. Bykovskii, A.A. Golubev, D.G. Kosyrev, K.I. Krechet, Yu.I. Lapitskii, S.V. Latyshev, R.T. Haydarov, B.U. Sharkov and A.V. Shumshirov, Laser and Part. Beams 2, 49 (1984).

27. J.S. Bakos, G. Burger, P.N. Ignacz, J. Szigeti, G. Petravich, S. Zoletnik and D. Hildebrandt, J. Nucl. Mater. 162, 381 (1989).

28. R.H. Dixon and R.C. Elton, Phys. Rev. Lett. 38, 1072 (1977).

29. T.N. Lee, W.A. Molander and R.C. Elton, Phys. Rev. A 33, 1202 (1986).

30. P.A. Naik, P.D. Gupta and S.P. Khumbare, Phys. Rev. A 43, 4540 (1991).

31. A.T. Prengel, J. Dehaven, E.J. Johnson and P. Davidovits, J. Appl. Phys. 48, 3551 (1977).

32. J.N. Broughton and R. Fedosejevs, J. Appl. Phys. 74, 3712 (1993).

33. I. Olivares and H.J. Kunze, Phys. Rev. E 47, 2006 (1993).

34. K. Matsuo, K. Tanaka, K. Muraoka and M. Akazaki, Jap. J. Appl. Phys. 30, 1102 (1991).

35. T.P. Duffey, T.G. McNeela, J. Mazumder and A.L. Schawlow, Appl. Phys. Lett. 63, 2339 (1993).

36. K. Mann and K. Rohr, Laser and Part. Beams 10, 435 (1992).

37. J.C.S. Kools and J. Dieleman, J. Appl. Phys. 74, 4163 (1993).

38. C. Timmer, S.K. Srivastava, T.E. Hall and A.F. Fucaloro, J. Appl. Phys. 70, 1888 (1991).

39. H.P. Gu, Q.H. Lou, N.H. Cheung, S.C. Chen, Z.Y. Wang and P.K. Lin, Appl. Phys. B 58, 143 (1994).

40. B.H. Ripin, C.K. Manka, T.A. Payser, E.A. McLean, J.A. Stamper, A.N. Mostovych, J. Grun, K. Keavney, J.Y. Crawford and J.D. Huba, Laser and Part. Beams 8, 183 (1990).

41. V.V. Bychkov, S.M. Golberg and M.A. Liberman, Sov. Phys. JETP 73, 642 (1991).

42. O.B. Anan'in, Yu.A. Bykovskii, Yu.V. Eremin, E.L. Stupitskii, I.K. Novikov, and S.P. Frolov, Sov. J. Quantum Elect. 21, 787 (1991).

43. J. Grun, J. Stamper, C. Manka, J. Resnick, R. Burris, J. Crawford and B.

H. Ripin, Phys. Rev. Lett 66, 2738 (1991).

44. J.J. MacFarlane, G.A. Moses and R.R. Peterson, Phys. Fluids B 1, 635 (1989).

45. S. Suckewer, C.H. Skinner, H. Milchberg, C. Keane and D. Voorhees, Phys. Rev. Lett. 55, 1753 (1985).

46. Abhilasha and R.K. Thareja, Phys. Lett. A 184, 99 (1993).

47. R.J. Spindler, J. Quant. Spectrosc. Radiat. Transfer 5, 165 (1965).

48. G. Herzberg, A. Lagerquist and C. Malberg, Can. J. Phy. 47, 2734 (1969).

49. M.I. Savadatti and K.S. Kini, Ind. J. Pure Appl. Phys. 10, 890 (1972).

50. X. Chen, J. Mazumder and A. Purohit, Appl. Phys. A 52, 328 (1991).

51. R.W. Dreyfus, R. Kelly and R.E. Walkup, Nucl. Inst. Meth. B 23, 557 (1987).

52. J.R. Sobehart, J. Appl. Phys. 74, 2830 (1993).

53. G. Koren and J.T.C. Yeh, J. Appl. Phys. 56, 2120 (1984).

54. J. Seth, R. Padiyath and S.V. Babu, Appl. Phys. Lett. 63, 126 (1993).

55. A.G. Gaydon, *The Spectroscopy of Flames 2nd Edition* (London, Chapman and Hall, 1957).

    J.E. Goldsmith and D.T.B. Kearsley, Appl. Phys. B 50, 371 (1990).

56. N.B. Richter, *The Nature of Comets* (London, Methuen, 1965).

57. D.L. Pappas, K.L. Saenger, J.J. Cuomo and R.W. Dreyfus, J. Appl. Phys. 72, 3966 (1992).

58. M. Ebben, G. Meijer and J.J. TerMeulen, Appl. Phys. B 50, 35 (1990).

59. W.A. deHeer, Rev. of Mod. Phys. 65, 611 (1993).

60. A. McKellar, Astron. J. 65, 350 (1960).

61. W. Weltner Jr. and R.J. Van Zee, J. Chem. Rev. 89, 1713 (1989).

62. J. Baker, S.K. Bramble and P.A. Hamilton, Chem. Phys. Lett. 213, 297 (1993).

63. P. Jena, B.K. Rao and S.N. Khanna, Eds., *Physics and Chemistry of Small Clusters* (Plenum Press, New York, 1987).

64. Q.M. Zhang, Jae-Yel Yi and J. Bernholc, Phys. Rev. Lett. 66, 2633 (1991).

65. H. Palmer and M. Shelef, *Chemistry and Physics of Carbon*, Ed. J.R. Walker, Jr.(Marcel Dekker, New York, 1961).

66. P.P. Radi, T.L. Bunn, P.R. Kemper, M.E. Molchan and M.T. Bowers, J. Chem. Phys. 88, 2809 (1988).

67. E.A. Rohlfing, J. Chem. Phys. 93, 7851 (1990).

68. J.M.L. Martin, J.P. Francois and R. Gijbels, J. Chem. Phys. 93, 8850 (1990).

69. H.W. Kroto, J.R. Heath, S.C. O'Brien, R.F. Curl and R.E. Smalley, Nature 318, 162 (1985).

70. E. Culotta and D.E. Koshland Jr., Science 254, 1706 (1993).

71. H.W. Kroto, A.W. Allaf and S.P. Balm, Chem. Rev. 91, 1213 (1991).

72. F. Diederich and R.L. Whetten, Acc. Chem. Res. 25, 119 (1992).

73. W. Kratschmer, L.D. Lamb, K. Fostiropoulos and D.R. Huffman, Nature 347, 354 (1990).

74. G. Meijer and D.S. Bethune, J. Chem. Phys. 93, 7800 (1990).

75. K.C. Rustagi, Ind. J. Phys. A 67, 493 (1993).

76. H.W. Kroto and K. McKay, Nature 331, 328 (1988).

77. T. Wakabayashi and Y. Achiba, Chem. Phys. Lett., 190, 465 (1992).

78. R. Kelly and J. E. Rothenberg, Nucl. Inst. Meth. B 7/8, 755 (1985).

79. Abhilasha, P.S.R. Prasad and R.K. Thareja, Phys. Rev. E 48, 2929 (1993).

80. C.E. Little and P.G. Browne, Chem. Phys. Lett. 134, 560 (1987).

81. P.K. Carroll and E.T. Kennedy, Contemp. Phys. 22, 61 (1981).

82. C. Fauquignon and F. Floux, Phys. Fluids 13, 386 (1970)

83. D.C. Emmony and J. Irving, Brit. J. Appl. Phys. 2, 1186 (1969).

84. J.B. Hasted, Physics of Atomic Collisions, (Butterworths, Washington, 1964).

85. P.T. Rumsby and J.W.M. Paul, Plasma Phys. 16, 247 (1974).

86. M. Mattioli, Plasma Phys. 13, 19 (1971).

87. L. Sedov, Similarity and Dimensional Methods in Mechanics (Academic, New York, 1959).

88. Ya. B. Zel'dovich and Yu. P. Raizer, Physics of Shock waves and High Temperature Hydrodyanamic Phenomenon (Academic, New York, 1966).

89. S. Chandrasekhar, Hydrodyanamic and Hydromagnetic Stability (Oxford University Press, London, 1981).

90. G. Taylor, Proc. R. Soc. London Ser. A 201, 192 (1950).

91. H.J. Kull, Phys. Fluids B 1, 170 (1989).

92. R.R. Whitlock, M.H. Emery, J.A. Stamper, E.A. McLean, S.P. Obenschain and M.C. Peckerar, Phys. Rev. Lett. 52, 819 (1984).

93. R.K. Thareja and Abhilasha, J. Chem. Phys. 100, 4019 (1994).

94. Abhilasha, R.K. Dwivedi and R.K. Thareja, J. Appl. Phys. 75, XXXX (1994).

95. P.S.R. Prasad, Abhilasha and R.K. Thareja, Phys. Stat. Sol.(a) 139, K1 (1993).

96. R K. Thareja, Abhilasha and Sampriti, Appl. Phys. Lett., submitted.

97. V. Kumar and R.K. Thareja, Phys. Edu. 9, 271 (1992).

98. J.T. Knudtson, W.B. Green and D.G. Sutton, J. Appl. Phys. 61, 4771 (1987).

99. R. Tambay, R. Singh and R.K. Thareja, J. Appl. Phys. 72, 1197 (1992).

100. H.R. Griem, Plasma Spectroscopy (McGraw-Hill, New York, 1964).

101. G. Bekefi, Priciples of Laser Plasmas (Wiley, New York, 1976).

102. R.M. Gilgenbach and P.L.G. Ventzek, Appl. Phys. Lett. 58, 1597 (1991).

103. D.W. Koopman, Phys. Fluids 14, 1707 (1971).

104. R.W. Dreyfus, R. Kelly and R.E. Walkup, Appl. Phys. Lett. 49, 1478 (1986).

105. R. Tambay, Ph.D. Thesis, I.I.T. Kanpur (1991).

106. L.L. Danylewych and R.W. Nicholls, Proc. R. Soc. A 339, 197 (1974).

107. A.R. Striganov and N.S. Sventitskii, in Tables of Spectral Lines of Neutral and Ionized Atoms (Plenum, New York, 1968).
W.L. Wiese, M.W. Smith and B.M. Glennon, Atomic Transition Probabilities Vol I (National Standard Reference Data System - NBS 4, US Government Printing Office, 1966).

108. P.R. Chalker, Diamond and Diamond-Like Films and Coatings, R.E. Clausing Ed. (Plenum Press, New York, 1991).

109. D.M. Cox, S. Behal, M. Disko, S.M. Gorun, M. Greaney,, C.S. Hsu, E.B. Kollin, J. Millar, J. Robbins, W. Robbins, R.D. Sherwood and P. Tindall, J. Am. Chem. Soc. 113, 2940 (1991).

110. C.N.R. Rao, T. Pradeep, R. Seshadri, R. Nagarajan, V.N. Murthy, G.N. Subbanna, F. D'Souza, V. Krishnan, G.A. Nagannagowada, N.R. Suryaprakash, C.L. Khetrapal and S.V. Bhat, Ind. J. Chem. 31, F5 (1992).

111. J.M. Dawson, Phys. Fluids 7, 981 (1964).

112. P. Mulser, R. Sigel and S. Witkowski, Phys. Reports 6, 187 (1973).

113. S.O. Dean, E.A. Mclean, J.A. Stamper and H.R. Griem, Phys. Rev. Lett. 27, 487 (1971).

114. O.B. Anan'in, Yu.A. Bykovskii, E.L. Stupitskit and A.M. Khudaverdyan,

Sov. J. Quant. Elect. 17, 1474 (1987).

115. T.P. Wright, Phys. Rev. Lett. 28, 268 (1972).

116. W.T. Silfvast, L.H. Szeto and O.R. Wood II, Opt. Lett. 4, 271 (1979).

117. R.H. Dixon, J.F. Seely and R.C. Elton, Phys. Rev. Lett. 40, 122 (1978).

118. J.M. Bridges, C.L. Cromer and T.J. McIlrath, Appl. Opt. 25, 2208 (1986).

119. V.I. Bayanov, V.A. Serebryakov, I.Yu. Skobelev, N.A. Soloev, A.Ya. Faenov and S.Ya. Khakhalin, Sov. J. Quant. Elect. 18, 1150 (1988).

120. T.N. Lee, Phys. Rev. A 27, 2082 (1983).

121. O.B. Anan'in, Yu.A. Bykovskii, B.V. Zamyshlyaev, A.G. Guz, E.L. Stupitski and A.M. Khudaverdyan, Sov J. Plasma Phys. 9, 186 (1983).

122. N. Qi, H. Kilic and M. Krishnan, Appl. Phys. Lett. 46, 471 (1985).

123. V. Kumar and R.K. Thareja, J. Appl. Phys. 67, 3260 (1990).

124. E.T. Kennedy, Contemp. Phys. 25, 31 (1984).

125. A. Khare and R.K. Thareja, IEEE J. Quant. Elect. 24, 2525 (1988).

126. A.W. Ali and W.W. Jones, Phys. Lett. A 55, 462 (1976).

127. W. Furukane, K. Sato and T. Oda, J. Phys. D 22, 390 (1989).

128. P. Mulser, Plasma Phys. 13, 1007 (1971).

129. R.R. Goforth and P. Hammerling, J. Appl. Phys. 47, 3918 (1976).

130. R.H. Dixon, R.C. Elton and J.F. Seely, Opt. Comm. 45, 397 (1983).

131. E.A. Rohlfing, J. Chem. Phys. 89, 6103 (1988).

132. D.P. Norton, D.H. Lowndes, J.D. Budai, D.K. Christen, E.C. Jones, J.W. McCamy, T.D. Ketcham, D.St. Julien, K.W. Lay, and J.E. Tkacyzk, J. Appl. Phys. 68, 223 (1990).

133. S. Deshmukh, E.W. Rothe and G.P. Reck, J. Appl. Phys. 66, 1370 (1989).

134. B. Brosda, R. Castell-Munoz and H.J. Kunze, J. Phys. D 23, 735 (1990).

135. F. Davanloo, E.M. Juengerman, D.R. Jander, T.J. Lee and C.B. Collins, J. Appl. Phys. 67, 2081 (1990).

136. G. Herzberg, *Molecular Spectra and Molecular Structure I. Spectra of Diatomic Molecules, 2nd Edition* (Van Nostrand Reinhold, New York, 1950).

137. G. Koren, A. Gupta, R.J. Baseman, M.I. Lutwyche and R.B. Laibowitz, Appl. Phys. Lett. 55, 2450 (1987).

138. L. Gausset, G. Herzberg, A. Lagerqvist and B. Rosen, Astrophys. J. 142, 45 (1965).

139. A. Fowler, Monthly Notices Roy. Astron. Soc. 70, 484 (1910).

140. M. Jeunehomme and R.P. Schwenker, J. Chem. Phys. 42, 2406 (1965)

141. K. P. Huber and G.Herzberg, *Molecular Spectra and Molecular structure*, IV, Constant of Diatomic molecules (Van Nostrand Reinhold, New York, 1979).

142. M. Anselment, R.S. Smith, E. Daykin and L.F. Dimauro, Chem. Phys. Lett. **134**, 444 (1987).

143. A. Bingham and P.L. Saiter, Anal. Chem. 48, 1735 (1976).

144. F. Dahmani and T. Kerdja, Laser and Part. Beams 9, 769 (1991).

145. G. Koren, Appl. Phys. Lett. 50, 1030 (1987).

146. F. Xiong and R.P.H. Chang, Mat. Res. Soc. Symp. Proc. 270, 451 (1992).

147. R.E. Smalley, in *Atomic and Molecular clusters*, E.R.Bernstein, Ed. (Elsevier, New York, 1990).

148. K.R. Thompson, R.L. DeKock, and W. Weltner, Jr., J. Am. Chem. Soc. **93**, 4688 (1971).

149. M. Vala, T.M. Chandrasekhar, J. Szczepanski, R.J. Van Zee, and W. Weltner, Jr., J. Chem. Phys. 90, 595 (1989).

150. J. Szczepanski, R. Pellow and M. Vala, Z. Naturforsch. 47a, 595 (1992).

151. P. Swings, *Molecular Spectra in Cosmic Sources in Astrophysics: A Symposium*, J.A. Hynek, Ed. (New York, McGraw Hill, 1951) 145.

152. K. Tanigaki, T.W. Ebbesen, S. Saito, J. Mizuki, J.S. Tsai, Y. Kubo and S.Kuroshima, Nature 352, 222 (1991).

153. Q. Gong, Y. Sun, Z. Xia, Y.H. Zou, Z. Gu, X. Zhou and D. Qiang, J. Appl. Phys. 71, 3025 (1992).

154. J.R. Heath, S.C. O'Brien, Q. Zhang, Y. Liu, R.F. Curl, H.W. Kroto, F.K. Tittel and R.E Smalley, J. Am. Chem. Soc. 107, 7779 (1985).

155. R.C. Haddon, A.F. Hebard, M.J. Rosseinsky, D.W. Murphy, S.J. Duclos, K.B. Lyons, B. Miller, J.M. Rosamilia, R.M. Fleming, A.R. Kortan, S.H. Glarum, A.V. Makhija, A.J. Muller, R.H. Eick, S.M. Zahurak, R. Ycko, G. Dabbagh and F.A. Thiel, Nature 350, 320 (1991).

156. A.F. Hebard, M.J. Rosseinsky, R.C. Haddon, D.W. Murphy, S.H. Glarum, T.T.M. Palstra, A.P. Ramirez and A.R. Kortan, Nature 350, 600 (1991).

157. K. Tanigaki, T.W. Ebbesen, S. Saito, J. Mizuki, J.S. Tsai, Y. Kuko and S. Kuroshima, Nature 352, 222 (1991)

158. S.S. Wagal, E.M. Juengeman and C.B. Collins, Appl. Phys. Lett. 53, 187 (1988).

159. B.L. Zhang, C.Z. Wang, K.M. Ho, C.H. Xu and C.T. Chan, J. Chem. Phys. 98, 3095 (1993).

160. J. Narayan, N. Biunno, R. Singh, O. Holland and O. Auciello, Appl. Phys. Lett. 51, 1845 (1987).

161. L. Lynds, B.R. Weinberger, G.G. Peterson, and H.A. Krasinski, Appl. Phys. Lett. 52, 320 (1988).

162. T. Sato, S. Furuno, S. Iguchi, and M. Hanabusa, Jpn. J. Appl. Phys. 26, 1487 (1987).

163. M. Hanabusa, M. Suzuki, and S. Nishigaki, Appl. Phys. Lett. 38, 385 (1981).

164. N. Biunno, J. Narayan, S.K. Hofmeister, A.R. Srivatsa and R.K. Singh, Appl. Phys. Lett. 54, 1519 (1989).

165. I.N. Mihailescu, N. Chitica, L.C. Nistor, M. Popescu, V.S. Teodorescu, I. Ursu, A. Andrei, A. Barborica, A. Luches, M.L. deGiorgi, A. Perrone, B. Dubreuil and J. Hermann, J. Appl. Phys. 74, 5781 (1993).

167. W.R. Creasy and J.T. Brenna, J. Chem. Phys. 92, 2269 (1990).

166. M. Yoshimoto, T. Arakane, T. Asakawa, K. Horiguchi, K. Hirai and H. Koinuma, Jpn. J. Appl. Phys. 32, L1081 (1993).

168. N. Takahashi, H. Dock, N. Matsuzawa and M. Ata, J. Appl. Phys. 74, 5790 (1993).

169. Y.Z. Li, M. Chander, J.C. Patrin, J.H. Weaver, L.P.F. Chibante and R.E. Smalley, Phys. Rev. B 45, 13837 (1992).

170. T. Hashizume, X. Wang, Y. Nishina, H. Shinohare, Y. Saito, Y. Kuk and T. Sakuvai, Jpn. J. Appl. Phys. 31, L880 (1992).

171. K. Motai, T. Hashizume, H. Shinohara, Y. Saito, H.W. Pickering, Y. Nishina and T. Sakurai, Jpn. J. Appl. Phys. 32, L450 (1993).

172. H. Ajie, M.M. Alvarez, S.J. Anz, S.D. Beck, F. Diederich, K. Fostiropoulos, D.R. Huffman, W. Kratschmer, Y. Rubin, K. Schriver, D. Sensharma and R.L. Whetten, J. Phys. Chem. 94, 8630 (1990).

173. D.S. Bethune, G. Meijer, W.C. Tang, H.J. Rosen, W.G. Golden, H. Selei, C.A. Brown and M.S. Devries, Chem. Phy. Lett. 179, 181 (1991).

174. G. Onida and G. Benedek, Europhys. Lett. 18, 403 (1992).

175. Q. Jiang , H. Xia, Z. Zhang and D. Tian, Chem. Phys. Lett. 192, 93 (1992).

176. F. Diederich, R. Ettl, Y. Rubin, R.L. Whetten, R. Beck, M. Alvarez, S. Anz, D. Sensharma, F. Wudl, K.C. Khemani and A. Kock, Science **253**, 548 (1991).

177. K. Kibuchi, N. Nakahara, T. Wakabayashi, M. Honda, H. Matsumiya, T. Moriwaki, S. Suzuki, H. Shiromaru, K. Saito, K. Yamauchi, I. Ikemoto and Y. Achiba, Chem. Phy. Lett. **188**, 177 (1992).

178. F. Negri, G. Orlandi and F. Zerbetto, Chem. Phy. Lett. **189**, 495 (1992).

179. Q.L. Zhang, S.C. O'Brien, J.R. Heath, Y. Liu, R.F. Curl, H.W. Kroto and R.E. Smalley, J. Phys. Chem **90**, 525 (1986).

180. R.F. Curl and R.E. Smalley, Science **242**, 1017 (1988).

181. P.P. Radi, M.T. Hsu, M.E. Rincon, P.R. Kemper and M.T. Bowers, Chem. Phys. Lett. **174**, 223 (1990).

PHY- 1994 - D - TRI - PUL